TECHNISCHE
UNIVERSITÄT
WIEN
Vienna University of Technology

Diploma Thesis

NUMERICAL ANALYSIS OF FLOW STRUCTURE AND HEAT TRANSFER IN BUBBLING FLUIDIZED BEDS

carried out for the purpose of obtaining the degree of

Master of Science (MSc or Dipl.-Ing.)

under the supervision of

Univ.Prof. Dipl.-Ing. Dr.techn. Markus Haider
(E302 - Institute for Energy Systems and Thermodynamics)
and
Univ.Ass. Dipl.-Ing. Stefan Thanheiser
(E302 - Institute for Energy Systems and Thermodynamics)
and
Projektass. Dipl.-Ing. Florian Heindl
(E302 - Institute for Energy Systems and Thermodynamics)

submitted at TU Wien

Faculty of Mechanical and Industrial Engineering

by

Noah Ladner
Matr.Nr. 11779613

Vienna, 17th June 2022 ....
(Noah Ladner)

Affidavit

I declare in lieu of oath, that I wrote this thesis and performed the associated research myself, using only literature cited in this volume.

Vienna, 17th June 2022 ....

(Noah Ladner)

Acknowledgement

At this point I would like to thank all those who have directly and indirectly contributed to the establishment of this diploma thesis.
I would especially like to thank Prof. Markus Haider, who made this work possible and supported me without tiring. He inspired me with his enthusiasm and excitement on the subject of fluidized bed heat exchangers.
I would also like to thank Florian Heindl, who has always shared his knowledge with me and thus supported me immensely. I would like to thank Prof. Heimo Walter for his commitment in terms of software and IT. Thanks also to Stefan Thanheiser, whose critical thinking made this diploma thesis what it has become.
Last but not least, I would like to thank my family, friends and people close to me, especially Magdalena, who made the ups and downs of studying WIMB tolerable and my parents for their unconditional support. Without them, none of this would have been possible.

Abstract

Using renewable energy sources to mitigate the effects of climate change requires innovative energy storage systems. One promising option for storing solar thermal energy is the use of low-cost and environmentally friendly particle based systems. The central element of this technology is a heat exchanger, which transfers the heat between the storage medium, such as quartz sand, and the working medium flowing through tube bundles. This counter current heat exchanger is based on an active fluidized bed technology, whereby the storage medium is fluidized by additional gas and a horizontal particle flow is imposed on the system.

For the sizing and optimal use of this technology, a comprehensive understanding of flow conditions and heat transfer behaviour is essential. Therefore, three main geometries, each with different tube types and arrangements, were investigated. The CPFD-Software Barracuda® was used to simulate the different constellations under the assumption of suitable initial and boundary conditions.

For the sake of comparability, ambiguities regarding minimum fluidization and fluidization degree were first eliminated. Initially, qualitative agreements with heat transfer coefficients already determined experimentally were detected. However, considerable quantitative deviations were determined. After a new parameterisation of the heat transfer model in Barracuda®, also a quantitative agreement was achieved. A MATLAB code was created to determine the bubble frequency at the different tube types. Since bubble frequency and particle convection are linked, conclusions could be drawn about the heat transfer behaviour. Finally, the relevance of baffles and the applied air-cushion technology in relation to bypass flows in fluidized bed heat exchangers and the associated energy efficiency was outlined.

Kurzfassung

Die Nutzung erneuerbarer Energiequellen zur Milderung der Auswirkungen des Klimawandels erfordert innovative Energiespeichersysteme. Eine vielversprechende Möglichkeit zur Speicherung solarthermischer Energie ist die Verwendung von kostengünstigen und umweltfreundlichen auf Partikel basierenden Systemen. Das zentrale Element dieser Technologie ist ein Wärmetauscher, der die Wärme zwischen dem Speichermedium, wie z. B. Quarzsand und dem durch Rohrbündel fließenden Arbeitsmedium überträgt. Dieser Gegenstromwärmetauscher basiert auf einer aktiven Wirbelschichttechnologie, bei der das Speichermedium durch ein Gas fluidisiert und dem System eine horizontale Partikelströmung aufgezwungen wird.

Für die Dimensionierung und den optimalen Einsatz dieser Technologie ist eine umfassende Kenntnis des Strömungs- und des Wärmeübergangsverhaltens unerlässlich. Daher wurden drei Hauptgeometrien mit jeweils unterschiedlichen Rohrtypen und -anordnungen untersucht. Die CPFD-Software Barracuda® wurde verwendet, um die verschiedenen Konstellationen unter der Annahme geeigneter Anfangs- und Randbedingungen zu simulieren.

Um eine Vergleichbarkeit zu ermöglichen, wurden zunächst Unklarheiten bezüglich der Minimalfluidisierung und des Fluidisierungsgrades geklärt. Zunächst wurden qualitative Übereinstimmungen mit den bereits experimentell ermittelten Wärmeübergangskoeffizienten bestätigt. Jedoch wurden erhebliche quantitative Abweichungen festgestellt. Nach einer Reparametrierung des Wärmeübergangsmodells in Barracuda® konnte eine quantitative Übereinstimmung erreicht werden. Außerdem wurde ein MATLAB-Code erstellt, um die Blasenfrequenz an den verschiedenen Rohrtypen zu bestimmen. Da Blasenfrequenz und Partikelkonvektion miteinander verbunden sind, konnten Rückschlüsse auf das Wärmeübertragungsverhalten gezogen werden. Schließlich wurde die Relevanz von Leitblechen und der Luftkissentechnologie in Bezug auf Bypass-Strömungen in Wirbelschichtwärmetauschern und die damit verbundene Energieeffizienz verdeutlicht.

Table of Contents

Nomenclature

List of Abbreviations

Abbreviation	Description
CFD	Computational Fluid Dynamics
CFL	Courant-Friedrichs-Lewy
CPFD	Computational Particle Fluid Dynamics
CSP	Concentrated Solar Power
DEM	Discrete element modelling
GPU	Graphics Processing Unit
HT	Heat Transfer
HTC	Heat Transfer Coefficient
IPCC	Intergovernmental Panel on Climate Change
MP-PIC	Multiphase particle-in-cell
TES	Thermal Energy Storage
TFM	Two-fluid model
CS	Cross section

List of Symbols

Symbol	Unit	Description
A_{pr}	m^2	Particle projection area
A_p	m^2	Particle surface
A_S	m^2	Immersed surface

Symbol	Unit	Description
Ar	-	Archimedes number
$c_{p,f}$	$\frac{J}{kgK}$	Fluid heat capacity
C_d	-	Drag Coefficient
C_S	-	Smagorinsky coefficient
c_v	$\frac{J}{kgK}$	Specific heat capacity of the particles
d_{sv}	m	Sauter-diameter
D_p	$\frac{1}{s}$	Drag function
d_p	m	Sieve diameter
d_s	m	Surface diamater
d_v	m	Volume diameter
Δp	Pa	Pressure drop
Δt	s	Time step
Δx_{cell}	m	Cell dimension
Δ	m	Computational grid size
δ_{ij}	-	Kronecker delta
ε	-	Porosity
ε_L	-	Porosity at the loosening point
$\vec{F}$	$\frac{N}{m^2}$	Momentum exchange rate per volume
f_d	-	Weight function
$\vec{F_p}$	N	Force exerted by the fluid on a particle
g	$\frac{m}{s^2}$	Gravity
h	$\frac{W}{m^2K}$	Heat transfer coefficient
H	m	Bulk height
h_d	$\frac{W}{m^2K}$	Dense particle phases heat transfer coefficient
h_{fw}	$\frac{W}{m^2K}$	Heat transfer coefficient between fluid and wall
h_{gc}	$\frac{W}{m^2K}$	Gas convective heat transfer coefficient
h_l	$\frac{W}{m^2K}$	Lean gas phase heat transfer coefficient
h_{max}	$\frac{W}{m^2K}$	Maximum heat transfer coefficient
h_p	$\frac{W}{m^2K}$	Heat transfer coefficient between fluid and particles
h_{pc}	$\frac{W}{m^2K}$	Particulate convective heat transfer coefficient
h_{rad}	$\frac{W}{m^2K}$	Radiative heat transfer coefficient
h_f	$\frac{J}{kg}$	Fluid enthalpy

Symbol	**Unit**	**Description**
h_p	$\frac{W}{m^2K}$	Heat transfer coefficient between particle and fluid
θ_{cp}	-	Close Pack Volume Fraction
θ_f	-	Fluid volume fraction
θ_p	-	Particle volume fraction
k_f	$\frac{W}{mK}$	Fluid thermal conductivity
L	m	Characteristic length
λ	$\frac{W}{mK}$	Thermal conductivity
λ_f	$\frac{W}{mK}$	Fluid thermal conductivity
λ_g	$\frac{W}{mK}$	Gas thermal conductivity
m	kg	Total mass
m_p	kg	Particle mass
μ	$Pa \cdot s$	Dynamic viscosity
μ_f	$Pa \cdot s$	Dynamic fluid viscosity
μ_g	$Pa \cdot s$	Dynamic viscosity of the fluid respectively gas
μ_t	$Pa \cdot s$	Turbulent viscosity
Nu	-	Nusselt number
Nu_{gc}	-	Gas convective nusselt number
Nu_p	-	Particle nusselt number
p	Pa	Fluid pressure
Pr	-	Prandtl number
Pr_g	-	Prandtl number of gas
ϕ	$\frac{s}{m^4kgK}$	Particle probability distribution function
Φ	$\frac{W}{m^3}$	Viscous dissipation
Ψ	-	Sphericity
$\dot{Q}$	$\frac{W}{m^3}$	Source of energy per volume
$\dot{Q}_{pg}$	W	Heat flow between particle and fluid
$\dot{Q}_{SB}$	W	Heat flow between between fluidized bed and immersed surface
$\dot{q}_D$	$\frac{W}{m^3}$	Enthalpy diffusion
R_g	$\frac{J}{kgK}$	Ideal gas constant
r_p	m	Volume based particle radius
Re	-	Reynolds number
Re_L	-	Reynolds number of lean phase

Symbol	Unit	Description
Re_p	-	Particle reynolds number
ρ_b	$\frac{kg}{m^3}$	Bulk density
ρ_f	$\frac{kg}{m^3}$	Fluid density
ρ_g	$\frac{kg}{m^3}$	Fluid respectively gas density
ρ_p	$\frac{kg}{m^3}$	Particle density
ρ_s	$\frac{kg}{m^3}$	Solid density
S	-	Interpolation operator
S_h	$\frac{W}{m^3}$	Conservative energy exchange from the particle phase to the fluid phase
t	s	Time
T_B	K	Bed temperature
T_f	K	Fluid temperature
T_g	K	Gas temperature
T_p	K	Particle temperature
T_S	K	Surface temperature
τ_D	s	Damping time
τ_p	$\frac{N}{m^2}$	Particle normal stress
$\vec{\vec{\tau}}_f$	$\frac{N}{m^2}$	Macroscopic fluid stress tensor
$\vec{u}_f$	$\frac{m}{s}$	Fluid velocity
U_g	$\frac{m}{s}$	Relative velocity between particle and fluid
U_f	$\frac{m}{s}$	Fluid velocity
$\vec{u}_p$	$\frac{m}{s}$	Particle velocity
$\overline{\vec{u}_p}$	$\frac{m}{s}$	Mean particle velocity
U_p	$\frac{m}{s}$	Particle velocity
v	$\frac{m}{s}$	Fluid velocity
V	m^3	Total volume
v_{mb}	$\frac{m}{s}$	Minimum bubbling velocity
v_{mf}	$\frac{m}{s}$	Minimum fluidisation velocity
v_t	$\frac{m}{s}$	Terminal velocity
V_p	m^3	Particle volume
V_v	m^3	Void volume
$\dot{V}$	$\frac{m^3}{s}$	Volume flow rate
$\dot{V}_{mf}$	$\frac{m^3}{s}$	Volume flow rate at minimum fluidisation

Symbol	**Unit**	**Description**
$\vec{x}_p$	m	Particle position

1 Introduction

Undeniably, one of the greatest challenges of the 21st century is climate change. Global warming and the associated effects are a highly debated topic for researchers, politicians and public. The effects of climate change will be felt by almost every inhabitant of this globalised world in the form of changes to ecosystems, reduction of biodiversity, health, food security, livelihood, water supply, human security and economic growth. With the current state of knowledge, these impacts become extreme above a temperature threshold of +1.5 °C, starting from preindustrial level. There are two main strategies to soften the impact. The first strategy is called adaptation and involves actions that reduce the negative impacts of climate change. The second and much more important strategy is called mitigation. It addresses the reduction of greenhouse gas sources and increase of greenhouse gas sinks. In concrete terms, the reduction of greenhouse gas emissions can be achieved, for example, through practicing energy efficiency or the use of renewable energies. The IPCC reports that a target of 70-85% of electricity is to be generated from renewable sources by 2050 [30].

But the push for renewable energy sources such as wind, water and solar energy is challenging. In contrast to fossil energy sources, the supply of energy is not constant due to dynamic weather events. This volatile energy supply must be compensated by grid operators in order to ensure security of supply. This required flexibilisation can be achieved through innovative energy storage systems.

1.1 Motivation

When thinking about energy storage, the first thing that comes to mind is probably a battery. Besides this electrochemical storage technology, energy can also be stored in the form of heat. If there is a demand for energy, the stored heat can be used to produce steam and generate electricity via a turbine. This concept is also known under the titles "Carnot-Battery" and "Pumped Thermal Energy Storage", and brings a number of advantages with it.

Thermal energy storage systems can use waste heat from industrial processes as well as the sun as a heat source. The latter can be realised, for example, with a Concentrated Solar Power Plant (CSP), as shown in Figure 1.1. Solar radiation falls on a large number of mirrors, also called heliostat field, which reflects the radiation to a common point. The concentrated solar radiation reaches the receiver, which is installed on a tower and heats a working medium. In the illustrated case, water serves as the working medium, which evaporates in the receiver, is collected in the steam drum and then can be used in the process via a turbine. The condenser closes the cycle. A steam storage system is integrated for cloudy periods. Under full load conditions, part of the generated steam is used to charge the storage system, whose capacity is sufficient for a limited period to feed the turbine in partial load operation [2].

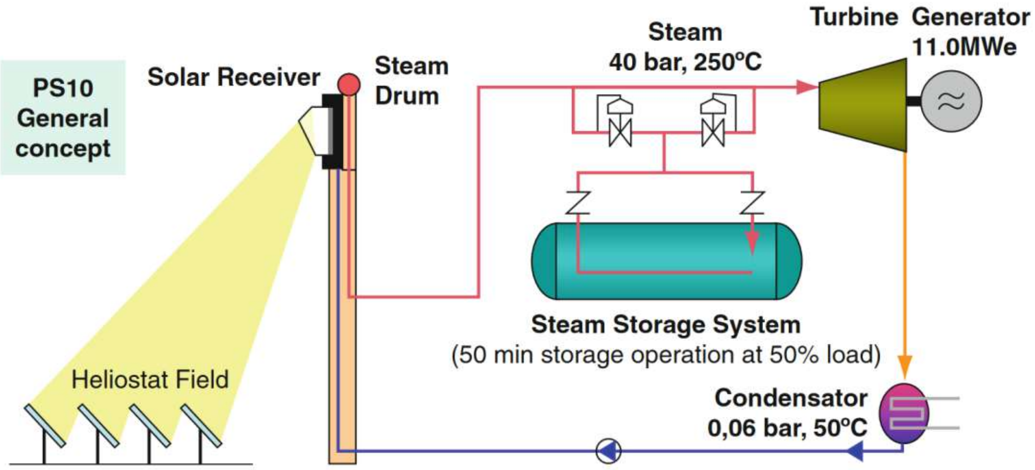

Figure 1.1: Concentrated solar power plant concept, Alexopoulos et al. [2]

Traditionally, a tube receiver is used, which consists of many vertical tubes on which the radiation falls. The working medium is heated by heat conduction through the tube wall. To avoid this diversion, which is associated with losses, a direct absorption receiver can be used as an alternative. In this case, the working medium is replaced by particles that are directly exposed to the radiation in the receiver. This allows significantly higher temperatures to be achieved and increases the efficiency of the system [2].

A heat exchanger is needed to ensure that the energy absorbed by the particles can be used in the turbine for electricity production. This should transfer the sensible heat to a power cycle based on water or supercritical CO_2. Fluidized bed heat exchangers in which the particles are fluidized by additional gas, such as air, are suitable for this task. In this fluidized area there are tubes containing the high-pressure working fluid that is heated.

1.2 Aim of this work

The use of fluidized bed heat exchangers leads to a number of advantages, but is challenging too. A very high heat transfer, temperature unifomity and a maximised overall thermal performance are distinguished as the main advantages of fluidized beds. Although the technology is relatively old, not all effects in fluidized beds have been fully researched. Predominantly, correlations based on experiments are applied, which have a small range of validity. The existing mechanistic models do not allow all effects to be fully explained.

However, for the planning and sizing of fluidized bed heat exchangers, knowledge of flow conditions, heat transfer behaviour and their interrelationships is essential. Therefore, this paper aims to contribute to a better understanding of these phenomena in order to enable a beneficial use of this promising technology.

1.3 Structure of this thesis

As mentioned above, the aim is to gain a deeper understanding and further knowledge of flow conditions, heat transfer behaviour and their interrelationships for fluidized bed technology-based heat exchangers. To achieve this, in the course of this work, a theoretical basis will first be created with the treatment of the fundamentals of fluidized bed technology. This includes the coverage of flow structures and heat transfer phenomena in bubbling fluidized beds. Since all investigations are carried out with the simulation program Barracuda Virtual Reactor®, the underlying equations, methods and models are briefly described to complete the theoretical framework.

Three different geometries, each with different tube types and arrangements are simulated as an approach to study the flow and heat transfer behaviour in fluidized beds. Their modelling in Barracuda®, including the set-up and boundary conditions used, is explained in detail.

The individual simulations and their results are discussed intensively. Based on the obtained findings and relevant literature, the subsequent simulations were adapted.

The thesis concludes with a summary of the tasks carried out and their most important results, as well as limitations of the work and possible future objectives.

2 Theoretical framework

This chapter is intended to provide the basis for all further research and consideration in this thesis. For this purpose, first the basic principles of fluidization engineering are presented, then the flow structure and heat transfer in fluidized beds are discussed in more detail, and finally the fundamentals of the simulation program used in this diploma thesis are explained.

2.1 Fluidization engineering

Generally, in a fluidized bed a bed of solid particles is loosened up and carried by an upward flowing fluid until the entire system exhibits fluid-like behaviour. As can be seen in Figure 2.1, depending on the fluid volume flow or fluid velocity, a distinction can be made between different fluidized bed states. State *a* is achieved when the fluid flows through the cavities at a very low velocity. The solid particles do not move and, as in the resting state, there is a fixed bed porosity. When the flow velocity increases, a state is reached in which all particles are in motion and have no permanent contact with each other. In this state *b*, there is minimum fluidization and the corresponding velocity is called the minimum fluidization velocity. If the fluid flow rate is increased further, in gas-solid bubbling fluidized beds practically solid-free bubbles form, which fuse during the ascent and thus increase in size if they are not splitted by components such as horizontal heat exchanger tubes. (Condition *c*) In the case of slim apparatus, the entire cross-section may be taken up by the gas bubbles. (State *d*) If the terminal velocity of the solid particles is reached by further increasing the fluid velocity, all the particles are discharged. As can be seen in Figure 2.1 *e*, such a fluidized bed state can only be achieved by a permanent recirculation of the particles through a recirculation cyclone [32].

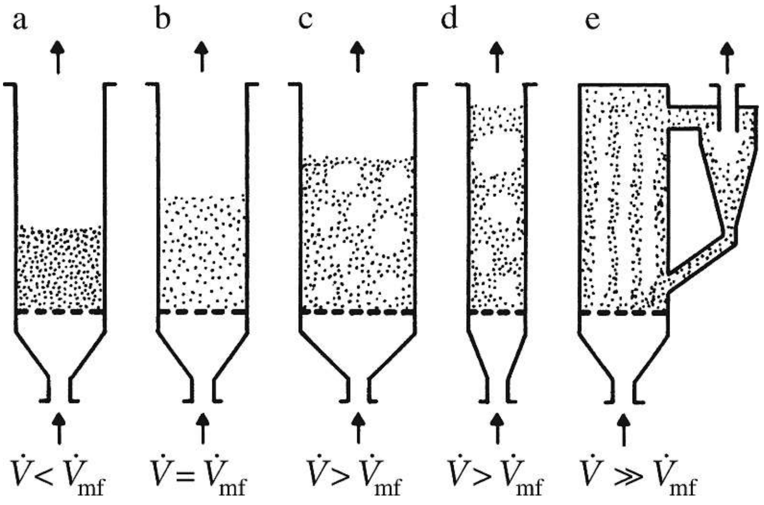

Figure 2.1: Fluidized bed states, Stephan et al. [32]

2.1.1 Characterisation of particles and fluidized beds

In the case of gas-solid fluidized beds, different flow conditions occur, which essentially depend on the gas velocity, the properties of the gas and the the properties of the particles.

The diameter of a perfectly round particle can be used as a descriptive quantity. If the shape deviates from this ideal form, as is the case for particles of industrial interest, reference or equivalent properties must be used for characterisation. Four important equivalent diameters are listed in Table 2.1 [15].

symbol	designation	definition	formula
d_p	Sieve diameter	Side length of the square which the particle passes through	-
d_v	Volume diameter	diameter of a sphere with the same volume as the particle	$d_v = \left(\frac{6V_p}{\pi}\right)^{1/3}$
d_s	Surface diamater	diameter of a sphere with the same surface area as the particle	$d_s = \left(\frac{A_p}{\pi}\right)^{1/2}$
d_{sv}	Sauter-diameter	diameter of a sphere with the same surface area to volume ratio as the particle	$d_{sv} = \frac{6V_p}{A_p} = \frac{d_v^3}{d_s^2}$

Table 2.1: Reference diameters for particle characterisation

By introducing a shape factor, some of these equivalent diameters can be related. A commonly used shape factor is the degree of true sphericity, introduced by Wadell [35]. Accordingly, the sphericity Ψ is defined as the ratio of the surface area of the sphere of equal volume to the surface area of the particle and can be expressed according to Equation 2.1.

$$\Psi = \left(\frac{d_v}{d_s}\right)^2 = \frac{d_{sv}}{d_v} \tag{2.1}$$

The sphericity takes the value 1 for spheres, for all other particle shapes it lies between $0 < \Psi < 1$. Typical values for the sphericity of common materials are listed in Table 2.2.

material	Ψ
crushed coal	0.70 - 0.75
crushed sand	0.70 - 0.85
rounded sand	0.90 - 0.95
limestone	0.65 - 0.75
ordinary salt	0.80 - 0.85
technical glass spheres	0.98 - 1.00

Table 2.2: Sphericity of common materials, Hofbauer [15]

Based on published data of experimental research, Geldart [10] categorised fluid-particle systems into four different groups in terms of their fluidizability. These four groups (A-D) were identified by plotting the difference in density between solid and fluid ($\rho_s - \rho_f$) against the mean particle size d_{sv}. The issue is depicted in Figure 2.2. According to Geldart [10], the major characteristics of the four groups are as follows:

- Group C: difficult to fluidize at all due to cohesive properties; very small, moist or very irregularly shaped particles
- Group A: dense phase expansion after minimum fluidization and before the beginning of bubble formation
- Group B: bubble formation at the minimum fluidization velocity; greatest practical relevance
- Group D: formation of stable spouted beds; large and/or dense particles

Quartz sand with an average grain size of 146 µm is used in context of this work. This corresponds to the working regime in group B, close to group A and results in a low fluidization effort.

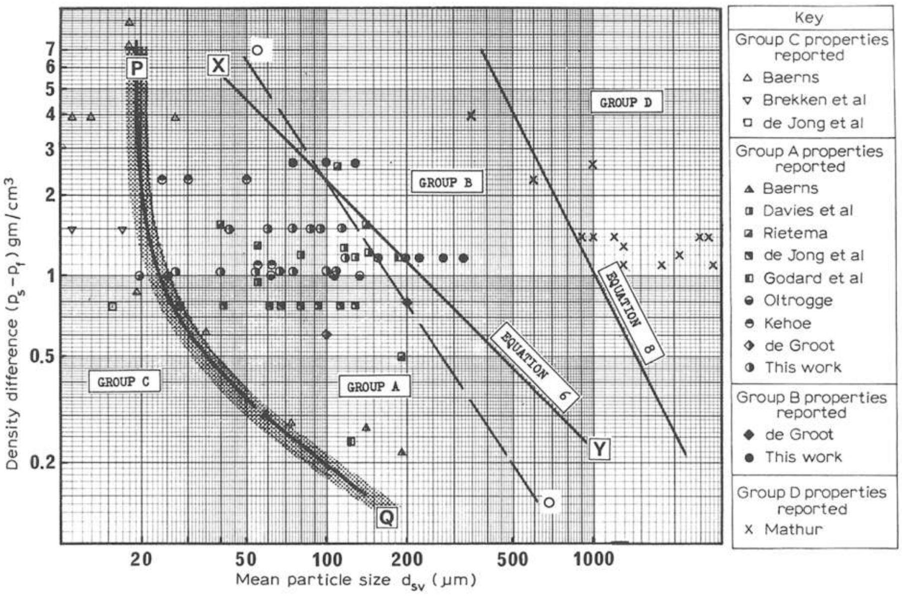

Figure 2.2: Geldart classification of powders, Geldart [10]

2.1.2 Porosity

An important characteristic of powders and bulk solids is the porosity ε, which is the ratio of void volume V_v to the total volume occupied by the particle bulk V. Using the bulk density ρ_b and the particle density ρ_p, the porosity can be calculated by eliminating the total mass m according to Equation 2.2 [25].

$$\varepsilon = \frac{V_v}{V} = \frac{V - V_p}{V} = 1 - \frac{m}{\rho_p V} = 1 - \frac{\rho_b}{\rho_p} \tag{2.2}$$

Thus, for the experimental determination of the fixed-bed porosity, the mass of the particles, the volume occupied by the bulk and the particle density must be known. In general, the different densities are specified in the manufacturer's data sheet.

The fixed-bed porosity should be determined in the state in which it is present in operation, because it depends very much on the packing arrangement, i. e. whether the fixed bed is in loose or vibrated bulk. The porosity in the fixed bed generally increases with sphericity and decreases with particle size and a wide particle size distribution [15].

2.1.3 Minimum fluidization velocity

As already mentioned in section 2.1, the point of minimum fluidization and the corresponding velocity is an essential parameter for the operation of fluidized beds. The determination of this crucial characteristic requires the following basic considerations.

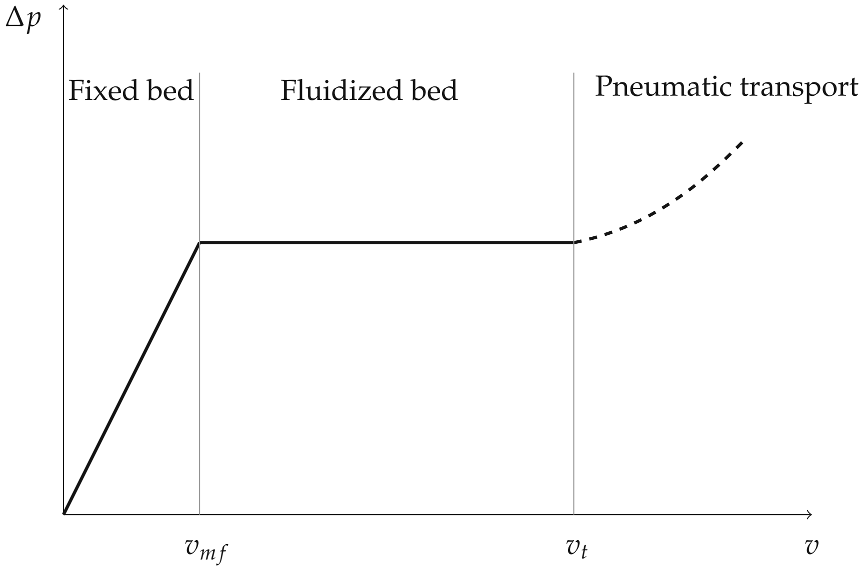

Figure 2.3: Pressure velocity diagram, based on Hofbauer [15]

In Figure 2.3, the pressure drop of the bulk is schematically plotted against the fluidization velocity. Using the curve, three different areas can be distinguished, as already mentioned in section 2.1, namely fixed bed, fluidized bed and pneumatic transport. According to Hofbauer [15], the mathematical specification of the pressure drop Δp in the fixed bed state can be done using the Ergun equation for Reynolds numbers greater than one. In this Equation 2.3, in addition to the bulk height H, the gas properties and the porosity ε, the surface-volume-related diameter d_{sv} also occurs. Especially for small diameters, the equation reflects the approximately linear course in the state of resting bulk very well.

$$\frac{\Delta p}{H} = 150\frac{(1-\varepsilon)^2}{\varepsilon^3}\frac{\mu_g v}{d_{sv}^2} + 1.75\frac{1-\varepsilon}{\varepsilon^3}\frac{\rho_g v^2}{d_{sv}} \tag{2.3}$$

Since the solid particles are kept in suspension in the fluidized bed state, the force acting on the bulk due to the pressure loss is equal to the gravity force of the particles reduced by their buoyancy force. This can be expressed by Equation 2.4. As already could be seen in Figure 2.3, the pressure drop in the fluidized bed state does not depend on the gas velocity and therefore remains constant, assuming that the bed mass is maintained.

$$\Delta p = (\rho_p - \rho_g)(1-\varepsilon)gH \tag{2.4}$$

Since the point of minimum fluidization is located at the transition from the fixed bed to the fluidized bed, the minimum fluidization velocity can be calculated by equating the pressure drop in the fixed bed (Equation 2.3) with the pressure loss in the fluidized bed (Equation 2.4).

$$\underbrace{\frac{\rho_g d_{sv}^3(\rho_p-\rho_g)g}{\mu_g^2}}_{Ar} = \underbrace{150\frac{(1-\varepsilon_L)}{\varepsilon_L^3}}_{C_1}\underbrace{\frac{\rho_g d_{sv} v_{mf}}{\mu_g}}_{Re} + \underbrace{1.75\frac{1}{\varepsilon_L^3}}_{C_2}\underbrace{\frac{\rho_g^2 d_{sv}^2 v_{mf}^2}{\mu_g^2}}_{Re^2} \tag{2.5}$$

By looking at Equation 2.5, Archimedes number (ratio of buoyancy force to friction force) and Reynolds number (ratio of inertia to viscous forces) can be identified. The remaining constant expressions are labeled C_1 and C_2. This notation allows the minimum fluidization velocity to be stated explicitly according to Equation 2.6.

$$v_{mf} = \frac{\mu_g}{\rho_g d_{sv}}\left(\sqrt{C_1^2 + C_2 Ar} - C_1\right) \tag{2.6}$$

In general, for an explicit expression of the minimum fluidization velocity v_{mf}, the porosity at the loosening point ε_L must be known. This quantity must be determined experimentally. A lot of research has already been done on this topic and Table 2.3 represents a selection of results for the two constants C_1 and C_2.

Author(s)	C_1	C_2	Particle diameter	Particle density
Richardson [23]	25.7	0.0365	-	-
Wen and Yu [36]	33.7	0.0408	2052 - 6350 µm	2360 - 7840 kg/m^3
Bourgeis and Grenier [6]	25.46	0.0382	86 - 25000 µm	1200 - 19300 kg/m^3
Babu, Shah and Talwalker [4]	25.25	0.0651	50 - 2870 µm	2560 - 3920 kg/m^3
Biń [5]	27.31	0.0386	40 - 2120 µm	1600 - 7500 kg/m^3

Table 2.3: Constants for Equation 2.6

2.1.4 Terminal velocity and drag

As can be seen in Figure 2.3, the terminal (free fall) velocity v_t forms the boundary between the fluidized bed area and the pneumatic transport. It corresponds to the lowest gas velocity at which the particles begin to move with the gas. The determination of the terminal velocity is based on the equilibrium of forces on the individual particle. The forces acting on the particle are marked in Figure 2.4. The resulting force balance is given in Equation 2.7.

$$\underbrace{\frac{\pi}{6}d_p^3\rho_p g}_{Gravity} - \underbrace{\frac{\pi}{6}d_p^3\rho_f g}_{Buoyancy} - \underbrace{C_d A_{pr}\frac{\rho_g v_t^2}{2}}_{Drag} = \underbrace{\frac{\pi}{6}d_p^3\rho_p\frac{dv_t}{dt}}_{Acceleration} \tag{2.7}$$

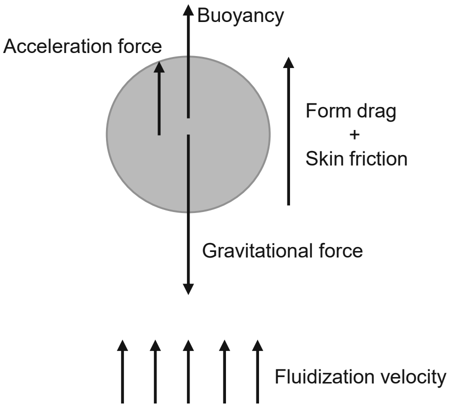

Figure 2.4: Force balance on the individual particle

Where ρ_f denotes the density of the fluid, A_{pr} the projection area of the particle perpendicular to the flow and C_d the drag coefficient which depends on the Reynolds number. In the case of reaching the terminal velocity, the acceleration respectively the right side of Equation 2.7 can be set to 0 and the following equation for the terminal velocity is obtained.

$$v_t = \sqrt{\frac{4(\rho_p - \rho_f)d_p g}{3\rho_f C_d}} \tag{2.8}$$

According to Hofbauer [15], the drag coefficient can be expressed depending on the Reynolds number ($Re = \frac{\rho_f v_t d_p}{\mu_f}$) as follows:

$$C_d = \begin{cases} \dfrac{24}{Re} & Re < 0.2 \\ \dfrac{24}{Re} + \dfrac{4}{\sqrt{Re}} + 0.4 & 0.2 \leq Re \leq 1000 \\ 0.43 & Re > 1000 \end{cases} \tag{2.9}$$

In the case of the transition regime, the terminal velocity can thus no longer be expressed explicitly and must be determined iteratively.

2.2 Flow structure of bubbling fluidized beds

In bubbling fluidized beds, bubbles are not only a visually dominant feature, but also determine properties such as heat and mass transfer. An understanding of the formation mechanisms and properties of bubbles helps to explain occuring effects in fluidized beds.

In general, the bubbling flow regime starts at the minimum bubbling velocity v_{mb}. This is equal to the minimum fluidization velocity v_{mf} for the Geldart groups B and D. For Geldart group A, $v_{mb} > v_{mf}$ applies. Bubble formation can be compared to turbulence in a single-phase pipe flow. In gas-fluidized beds, however, no eddies are formed as a result of turbulence, but rather almost solid-free bubbles of spherical-cap shape. The formation of such turbulence is usually very fast, so bubbles can be observed immediately above the distributor [11].

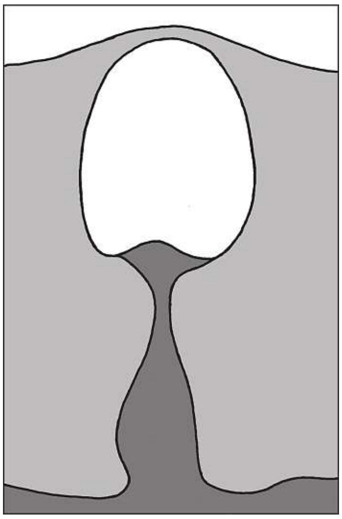

Figure 2.5: Structure of a bubble, Grace [11]

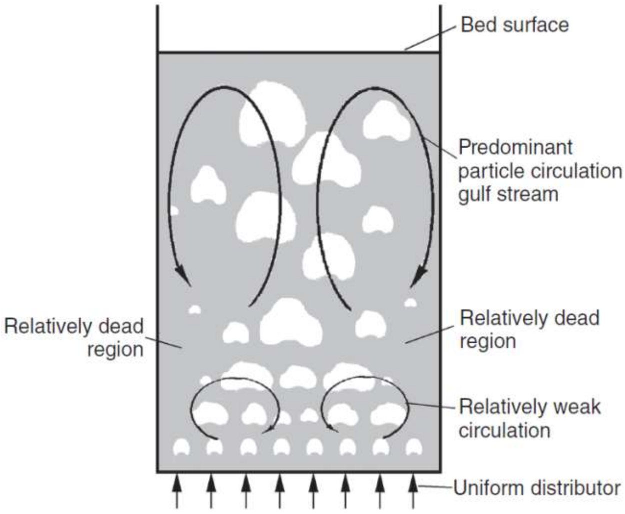

Figure 2.6: Circulation patterns, Grace [11]

Figure 2.5 shows a bubble penetrating a boundary layer between darker and lighter particles with otherwise identical properties in a two-dimensional fluidized bed. Before the bubble was injected, the boundary layer was horizontal. In this illustration, the wake that has formed on the bottom of the bubble and the particles that have been transported upwards as a result can be seen very clearly. Depending on the particle properties, different ratios of wake volume to void volume, also called wake fraction, occur. For example, the wake fraction is much larger for smooth spherical particles than for angular sand. An increase in particle size results in a decrease of the wake fraction. When bubbles arrive at the surface of the bed, eruptions of particles into the freeboard occur.

Together with wake transport, the drift effect is the most important mechanism for solids mixing in fluidized beds. In freely bubbling beds, there is a non-uniform spatial distribution of bubbles, as the bubbles grow by coalescence with increasing height. There is a lack of bubbles on the confining sidewalls even though the distributor delivers bubbles uniformly at the bottom of the bed. This leads to a weak up-the-outside, down-at-the-centre flow pattern, as shown schematically in

Figure 2.6 [11].

2.3 Heat transfer in fluidized beds

The fluidized bed key advantage is the excellent heat transfer. A distinction can be made between particle-fluid heat transfer and bed-surface heat transfer. Technically relevant surfaces can be heating or cooling coils, column walls, and bare or finned tube banks. A rough overview of different achievable bed-to-surface heat transfer coefficients is given in Figure 2.7. Overall, fluidized beds can achieve heat transfer coefficients that are an order of magnitude higher than those of fixed beds and even two orders of magnitude higher than air flowed empty tubes [16].

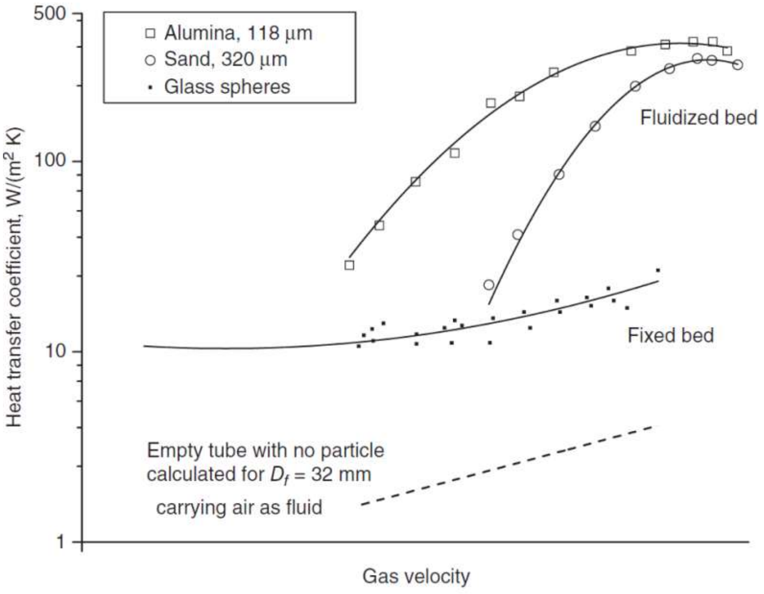

Figure 2.7: Orders of magnitude of the heat transfer coefficient, Dening [16]

Another important characteristic is the temperature uniformity of fluidized beds. Under most operating conditions the temperature difference between dense phase and bubbles is in the order of few degrees. Due to this rapid heat transfer, fluidized beds may be assumed isothermal. Interphase heat transfer needs not be considered, as thermal equilibrium usually is achieved within 25 mm of fluid injection. In case of materials with poor heat transfer properties such as biomass or exothermic reactions in the bed, this assumption is not correct [16].

In many instances the subject is still being researched, and no single design method has become

generally accepted. Empirical correlations are not able to capture the wide range of variables and conditions. Uncertainties in the prediction of heat transfer coefficients of $30 - 40\%$ are reality. Mechanistic models are more reliable but need to be carefully selected [7] [24] [40].
Nevertheless, the following subsections should provide an overview of the mechanisms and approaches for describing heat transfer in fluidized beds.

2.3.1 Particle-fluid heat transfer

In gas-solid fluidized beds, the heat transfer between particle and fluid is defined by:

$$h_p = \frac{\dot{Q}_{pg}}{A_p (T_g - T_p)_m} \tag{2.10}$$

This includes the heat flow $\dot{Q}_{pg}$ transferred from the fluid respectively gas to the particle, the total particle surface A_p and the driving temperature difference between fluid and particle surface $(T_g - T_p)_m$ averaged over the transfer area [15].
The heat transfer between the individual particle and the fluid is not very large, with magnitudes of 1 to 100 $\mathrm{W/m^2K}$. However, the heat transfer per unit bed volume is very high due to the large total particle surface. The particle-fluid heat transfer becomes increasingly complex when not only considering the convective heat transfer at the individual particle but the entire fluidized bed along with the complex flow pattern. The phenomenon is described with the help of the dimensionless Nusselt number, which characterises the heat transfer, and the Reynolds number for the consideration of the flow behaviour, which are defined as follows:

$$Nu_p = \frac{h_p d_p}{\lambda_g} \qquad Re_p = \frac{\rho_g U_g d_p}{\mu_g} \tag{2.11}$$

Based on numerous experimentally determined data, correlations for the particle Nusselt number as a function of the particle Reynolds number were established in order to predict the heat transfer between particle and fluid:

$$Nu_p = \begin{cases} 0.0282 Re_p^{1.4} Pr_g^{0.33} & 0.1 \leq Re_p \leq 50 \\ 1.01 Re_p^{0.48} Pr_g^{0.33} & 50 < Re_p \leq 10^4 \end{cases} \tag{2.12}$$

In principle, the heat transfer coefficient increases with increasing thermal conductivity of the gas λ_g, increasing fluid density ρ_g, decreasing viscosity μ_g and increasing relative velocity between particle and fluid. These relationships are well represented by Equation 2.12. But there are uncertainties associated with this correlation, since assumptions such as well mixed particles and plug flow from the gas were made with respect to the Prandtl number [40].

2.3.2 Bed-surface heat transfer

The heat transfer coefficient between a fluidized bed and the surfaces of heating or cooling elements installed therein is defined as:

$$h = \frac{\dot{Q}_{SB}}{A_S(T_S - T_B)} \tag{2.13}$$

This uses the heat flow transferred from the surface of the installation A_S to the fluidized bed $\dot{Q}_{SB}$, the surface temperature T_S and the uniformly assumed temperature of the fluidized bed at a sufficient distance from the surface T_B [15].

$$h = h_{pc} + h_{gc} + h_{rad} \tag{2.14}$$

One approach to describe the bed-surface heat transfer is to additively aggregate the individually occurring heat transfer phenomena, according to equation 2.14. Hence, the particulate convective h_{pc}, the gas convective h_{gc} and the radiative component h_{rad} contribute to the total heat transfer. This additive interaction is a common simplification that must be treated with caution when two or more components have the same magnitudes [16].

Due to the extremely small contact points between particle and surface, the direct particle-surface conduction is negligible [24].

Particle convection refers to the circumstance that a frequent particle renewal on the surface takes place. In a bubbling fluidized bed, the rising bubbles sweep past the heat exchange surface, washing away the particles resting there and bringing new bed particles into direct contact with the surface [18]. Especially in fluidized beds with small particles, bubble-induced motion of solid particles and bubble dynamics play an important role, since the predominant part of the heat transfer is particle convection [24].

Mechanistic approaches for describing this phenomenon are often divided into three categories:

- Single particle models: heat transfer through unsteady-state conduction to a single particle or a chain of particles (Figure 2.8a)
- Alternating layers of gas and solids: Agreement with experimental studies was achieved by selecting the layer thicknesses of gas and solid phases as shown in Figure 2.8b.
- Packet theory: Surfaces are contacted alternatively by gas bubbles and an emulsion of densely packed particles called packets (Figure 2.8c) [16]

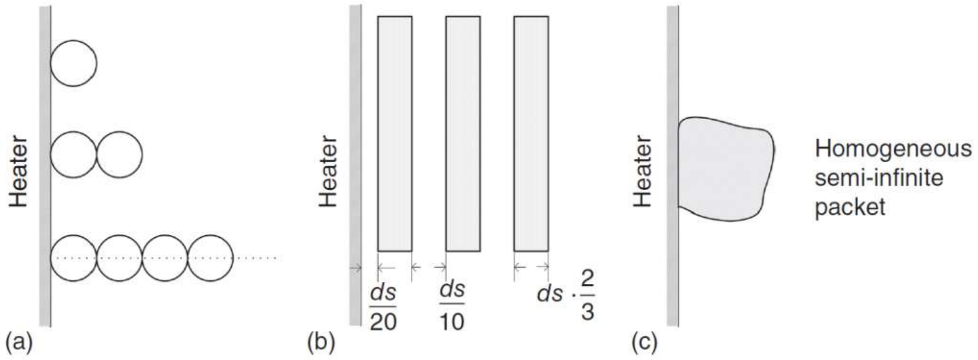

Figure 2.8: Mechanistic approaches, Dening [16]

Gas convection considers heat transfer to and from interstitial gas and gas bubbles [16]. This share of the total heat transfer is negligible for small particle diameters. Only for diameters above 1 mm are essential contributions due to gas convection obtained. Using the Archimedes number Ar and the Prandtl number Pr, the gas convection fraction can be predicted by a correlation of Baskakov [15].

$$Nu_{gc} = \frac{h_{gc} d_{sv}}{\lambda_g} = 0.009 Ar^{0.5} Pr^{0.33} \tag{2.15}$$

$$Ar = \frac{\rho_g (\rho_p - \rho_g) g d_{sv}^3}{\mu^2} \qquad Pr = \frac{c_g \mu}{\lambda_g}$$

Radiation effects are only relevant for temperatures above 500 °C. The radiative heat transfer is of increasing importance the higher the bed temperature and the larger the particles are [16]. Since neither high temperature levels nor large particles are used in the context of this work, this complex phenomenon will not be discussed further.

The maximum time-average heat transfer coefficients between gas-fluidized bed and fixed surfaces are reached at a certain fluidization velocity. When the superficial velocity exceeds the minimum fluidization velocity, the overall heat transfer coefficient increases steeply. Further increasing the fluidization velocity increases the bubble frequency, which in turn corresponds to higher particle renewal on the heat exchanger surface. If the fluidization velocity is increased even further, the residence time of the particles at the surface becomes so short that at a certain point the heat transfer coefficient starts decreasing [16].

Furthermore, the heat transfer coefficient between gas-fluidized bed and fixed surfaces decreases with increasing particle diameter and depends on local conditions. For example, horizontal heat exchanger tubes show different heat transfer coefficients at different circumferential positions.

For small particles, the highest heat transfer coefficients were identified on the bottom and sides. On the top of the tube, however, there is a significantly lower heat transfer due to a stagnant cap of solid particles. As the defluidized area on the top of the tube increases with increasing tube diameter, a reduction in the heat transfer coefficient is expected [7] [24].

Zabrodsky [41] developed a correlation that quantifies the maximum heat transfer coefficient h_{max} between bed and surface:

$$\frac{h_{max} d_p}{\lambda_g} = 0.88 Ar^{0.213} \quad \text{for} \quad 10^2 < Ar < 1.4 * 10^5 \tag{2.16}$$

Equation 2.16 can be applied to vertical and horizontal tubes. However, it only gives satisfactory results for particle diameters ≤ 1 mm. For larger particles, the correlation of Maskaev and Baskakov[19] is suggested.

$$\frac{h_{max} d_p}{\lambda_g} = 0.21 Ar^{0.32} \quad \text{for} \quad 1.4 * 10^5 < Ar < 3 * 10^8 \tag{2.17}$$

2.4 Barracuda Virtual Reactor®

For the research in this thesis, the commercial software Barracuda Virtual Reactor® is used. In the following subsections, the relevant approaches and models used by this simulation tool are briefly introduced.

Barracuda® was developed for problem solving and optimisation of fluidized bed reactors and other particle-fluid systems on an industrial scale. The so called CPFD (Computational Particle Fluid Dynamics) model is an combined Euler-Lagrangian approach that allows the simulation of simultaneous gas and particle flows, with consideration of fluid-particle interactions such as thermal and chemical processes. This Euler-Lagrangian approach based MP-PIC (multiphase particle-in-cell) method, was first mentioned in literature by Andrews et al. [3] and extended to three dimensions by Snider [28]. Thus, the large number of real particles (10^{16} or more in industrial-scale systems) is represented by a smaller number of computational particles respectively particle parcels, for which the mass, momentum, and energy transport equations are solved [1].

In this work, simulations are performed in the order of up to 1.000.000 cells and real time of 120 s. Despite the reduction of calculation effort resulting from the MP-PIC method and the possibility of parallel calculation using GPU provided by Barracuda®, a calculation time in the order of weeks must be taken into account. In the course of this work, investments were made in new hardware and software. In combination with an update from Barracuda Virtual Reactor® version 17.3.1 to 21.1.1, this resulted in a reduced computing time by a factor of 6 for the last simulations.

2.4.1 Multiphase particle-in-cell method

In general, there are different mathematical approaches avaliable to describe a flow system. Two important representatives are the Eulerian continuum approach and the Lagrangian trajectory approach. The Eulerian approach assumes a fluid as a continuum and describes all variables of the flow as field variables, i. e. pressure, mass flux, temperature, concentration and velocity are specified at all fixed location points of any time step. On the other hand, in the Lagrangian approach trajectories of the individual fluid elements or particles are followed. Based on a starting point, all flow variables are therefore balanced at the individual element or particle [9].
Building on these mathematical description possibilities, two main numerical modelling options for gas-solid flows were developed. One option for the numerical description of fluidized beds is the Euler-Euler two-fluid model (TFM). In this model, the solid phase is considered as a pseudo-fluid. In combination with the kinetic theory of granular flow, both phases can be modelled as interacting continua. The main advantages of TFM are the low computational costs and thus potentially high amounts of particles that can be modelled. However, the accuracy depends on the used closure models and the additional modelling of multiple phases or chemical reactions becomes increasingly complex. These issues led to the development of discrete element modelling (DEM), which models each individual element separately, including all physical interactions. This method results in very high computational costs [29].

The MP-PIC method combines the advantages of the Eulerian-Eluerian continuum method and the Eulerian-Langrangian discrete method. Hence a possible high number of particles with different properties, such as size, density and velocity, can be simulated. The MP-PIC method uses a mapping technique of Lagrangian particles to a computational grid and mapping back computed stress tensors to the particle positions [3].
The fluid phase is simulated in the MP-PIC method by a continuum approach and the solid phase is modelled by virtual Langrangian points. In contrast to the DEM method, the MP-PIC method simulates the movement of virtual particle parcels. This procedure is illustrated schematically in Figure 2.9. The image shows a fluidized bed with a coarse Cartesian grid constructed over it. Each cell in the grid contains a certain number of particle parcels. The parcels represent a

cluster of identical particles with the same velocity, density and size. Therefore a certain number of parcels fits into one cell and there must be correspondingly sufficient space for specific parcels in a adjacent cell, if there is a potential exchange of parcels in the next time step. For this reason, the cell size must be kept fairly coarse and must not change significantly between adjacent cells. Following this, the MP-PIC method does not simulate the individual particle interactions, but converts the parcel position via interpolation polynomials to the Cartesian grid, where the solid phase normal stress is calculated. After this stress gradient has been determined on the grid, the effect is interpolated back to the particle position [29].

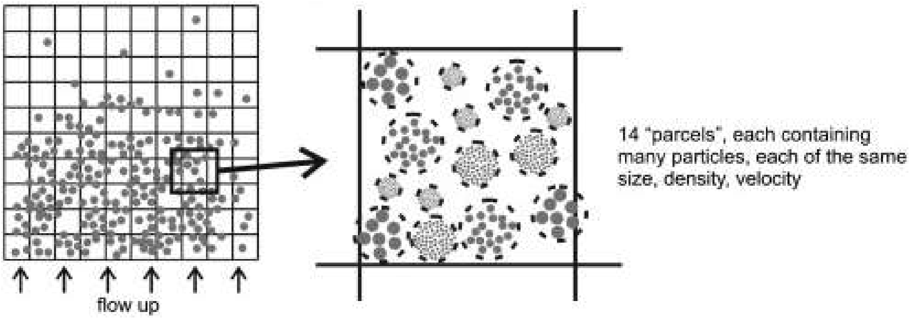

Figure 2.9: Particles parcels used in MP-PIC, Solnordal et al. [29]

2.4.2 Governing equations gas phase

Based on Snider [28], the continuity and the momentum equation for the gas phase without interphase mass transfer are shown in Equations 2.18 and 2.19.

$$\frac{\partial(\theta_f \rho_f)}{\partial t} + \nabla \cdot (\theta_f \rho_f \vec{u_f}) = 0 \tag{2.18}$$

$$\frac{\partial(\theta_f \rho_f \vec{u_f})}{\partial t} + \nabla \cdot (\theta_f \rho_f \vec{u_f} \vec{u_f}) = -\nabla p - \vec{F} + \theta_f \rho_f \vec{g} + \nabla \cdot (\theta_f \overrightarrow{\overrightarrow{\tau_f}}) \tag{2.19}$$

These include the volume fraction of the fluid resp. gas θ_f, the fluid density ρ_f, the fluid velocity $\vec{u_f}$, the fluid pressure p, the momentum exchange rate per volume between gas and particles $\vec{F}$, the gravitational acceleration $\vec{g}$ and the macroscopic fluid stress tensor $\overrightarrow{\overrightarrow{\tau_f}}$. The index notation of the stress tensor $\overrightarrow{\overrightarrow{\tau_f}}$ is defined according to Equation 2.20.

$$\tau_{f,ij} = \mu \left(\frac{\partial u_i}{\partial x_j} + \frac{\partial u_j}{\partial x_i} \right) - \frac{2}{3} \mu \delta_{ij} \frac{\partial u_i}{\partial x_i} \tag{2.20}$$

δ_{ij} represents the Kronecker delta, which is 1 if $i = j$ and 0 if $i \neq j$. x_i is the spatial variable. The viscosity μ is the sum of the dynamic viscosity of the fluid and a turbulent viscosity μ_t calculated according to a turbulence model by Smagorinsky [26], stated in Equation 2.21.

$$\mu_t = C_S^2 \rho_f \Delta^2 \sqrt{\left(\frac{\partial u_i}{\partial x_j} + \frac{\partial u_j}{\partial x_i}\right)^2} \tag{2.21}$$

The Smagorinsky coefficient C_S in Barracuda® is set to a constant default value of 0.1 and Δ is equivalent to the local computational grid size [20]. The energy equation for the fluid phase is given in Equation 2.22.

$$\frac{\partial(\theta_f \rho_f h_f)}{\partial t} + \nabla \cdot (\theta_f \rho_f h_f \vec{u_f}) = \theta_f \left(\frac{\partial p}{\partial t} + \vec{u_f} \cdot \nabla p\right) + \Phi + \nabla \cdot (\theta_f \lambda_f \nabla T_f) + \dot{Q} + \dot{q}_D + S_h \tag{2.22}$$

Including the fluid enthalpy h_f, the viscous dissipation Φ, the fluid thermal conductivity λ_f, the fluid temperature T_f and the conservative energy exchange from the particle phase to the fluid phase S_h. The issue treated in this thesis, neither comprise a source of energy per volume $\dot{Q}$ nor enthalpy diffusion associated with chemical reactions $\dot{q}_D$.

The gas respectively fluid density ρ_f is computed using the ideal gas equation of state:

$$p = \rho_f R_g T \tag{2.23}$$

2.4.3 Governing equations solid phase

Based on Snider [28], the particle phase in Barracuda® is described by a particle probability distribution function ϕ. This is a function of particle position, particle velocity, particle volume, particle density, particle temperature and time. The particle probability distribution function can be expressed by the Liouville equation. Without interphase mass transfer, the Liouville equation reads as follows:

$$\frac{\partial \phi}{\partial t} + \nabla \cdot (\phi \vec{u_p}) + \nabla_{\vec{u_p}} \cdot \left(\phi \frac{\partial \vec{u_p}}{\partial t}\right) = 0 \tag{2.24}$$

$\nabla_{\vec{u_p}}$ represents the divergence operator of particle velocity. The Liouville equation also includes particle acceleration, which can be expressed by Equation 2.25.

$$\frac{\partial \vec{u_p}}{\partial t} = D_p(\vec{u_f} - \vec{u_p}) - \frac{1}{\rho_p}\nabla p + \vec{g} + \frac{\overline{\vec{u_p}} - \vec{u_p}}{2\tau_D} - \frac{1}{\theta_p \rho_p}\nabla \tau_p + X \tag{2.25}$$

The first term considers the flow drag expressed via the drag function D_p and the relative velocity between fluid and particle. The second term takes into account the buoyancy force via the pressure gradient of the fluid and the third term the gravity. The fourth term models the damping due to inelastic collision processes. Particles whose velocity deviates from the mean velocity receive an acceleration in the respective direction. τ_D is the damping time and depends on the particle volume fraction and the elastic properties of the particles. The particle-particle interaction force is calculated via the gradient of the particle normal stress τ_p, which will be described further below. The term X denotes the influence of particle contact at different particle volume fractions. For a detailed explanation, it is referred to O'Rourke et al. [22].

The particle volume fraction at a given location at a given time is obtained by integrating the particle distribution function multiplied by the particle volume over mass, velocity and temperature [39].

$$\theta_p = \iiint \phi \frac{m_p}{\rho_p} dm_p d\vec{u}_p dT_p \tag{2.26}$$

In Barracuda® the Harris and Crighton model[12] is used to compute the particle normal stress. The stress function τ_p is a function of the particle volume fraction θ_p and defined in Equation 2.27.

$$\tau_p = \frac{P_s \theta_p^{\beta}}{max[(\theta_{cp} - \theta_p), \varepsilon(1 - \theta_p)]} \tag{2.27}$$

The used default values for the remaining constants are listed below. The model is designed in a way that the particle stress tends to zero with the particle volume fraction at very low solids loading and to infinity in the fixed bed. The maximum function with the very small value ε in the denominator was introduced to avoid a singularity [1].

$P_s = 1\,Pa$	$\beta = 3$	$\varepsilon = 10^{-8}$

The interphase momentum exchange rate per volume used in Equation 2.19 is given according to Snider [28] as follows:

$$\vec{F} = \iiint \phi V_p \rho_p \left[D_p(\vec{u}_f - \vec{u}_p) - \frac{1}{\rho_p} \nabla p \right] dV_p d\rho_p d\vec{u}_p \tag{2.28}$$

In Barracuda®, only the heat transfer between particles and fluid is considered. The energy equation of the particle phase can be formulated according to Equation 2.29. In its general form, it would include convective heat flux as well as radiation and heat of reactions. However, the last two do not play a role in this thesis.

$$m_p c_v \frac{dT_p}{dt} = A_p h_p (T_f - T_p) \tag{2.29}$$

Among other variables, the specific heat capacity of the particles c_v, the particle surface area A_p and the heat transfer coefficient between the fluid and the particles h_p are included. This leads to the expression for the energy exchange from the particle phase to the fluid phase already used in Equation 2.22.

$$S_h = \iiint \phi m_p \left[D_p(\vec{u_f} - \vec{u_p})^2 - c_v \frac{dT_p}{dt} \right] dm_p d\vec{u_p} dT_p \tag{2.30}$$

2.4.4 Drag model

For the calculation of the drag function of Equation 2.25, different models are offered for selection in Barracuda®. In general, a drag model calculates the force $\vec{F_p}$ exerted by the fluid on a particle. This force can be calculated as a function of the particle mass m_p, the drag function D_p and the relative velocity between fluid and particle as follows: [1]

$$\vec{F_p} = m_p D_p (\vec{u_f} - \vec{u_p}) \tag{2.31}$$

The drag function is related to the drag coefficient C_d according to equation 2.32. Among other variables, it also includes the volume-based particle radius r_p.

$$D_p = \frac{3}{8} C_d \frac{\rho_f |\vec{u_f} - \vec{u_p}|}{\rho_p r_p} \tag{2.32}$$

In many drag model options, the drag coefficient depends on the flow conditions and thus on the Reynolds number, which is defined as follows:

$$Re = \frac{2 \rho_f r_p |\vec{u_f} - \vec{u_p}|}{\mu_f} \tag{2.33}$$

In Barracuda® there is the possibility to choose between 10 different drag models (see [1] for detailed listing) and it is possible to create user-defined models. In this thesis the Wen-Yu model [37] is used. Similarly as already discussed in chapter 2.1.4, the drag coefficient is calculated as a function of the Reynolds number according to Equation 2.34.

$$C_d = \begin{cases} \frac{24}{Re} \theta_f^{-2.65} & Re < 0.5 \\ \frac{24}{Re} \theta_f^{-2.65} (1 + 0.15 Re^0.687) & 0.5 \leq Re \leq 1000 \\ 0.44 \theta_f^{-2.65} & Re > 1000 \end{cases} \tag{2.34}$$

This model is based on a single particle drag model and considers the particle packing via the fluid volume fraction multiplier $\theta_f^{-2.65}$. For small Reynolds numbers Stokes drag $\frac{24}{Re}$, for large Reynolds numbers an initial drag coefficient of 0.44 and in the transition region an expression of Schiller and Naumann is used.

2.4.5 Modelling the heat transfer

For the fulfilment of the energy equation, the local heat transfer coefficients between fluid and wall and between fluid and particle are determined in Barracuda®. In addition, a radiative heat transfer model can be defined. However, this is not treated in this work, as due to the low temperature ranges of below 500 °C this type of heat transfer can be neglected.

The following calculation equations for the heat transfer coefficients h are based on power approaches. The general relation between Nusselt Nu, Reynolds Re and Prandtl number Pr, as well as the heat transfer coefficient h, the characteristic length L and the thermal conductivity λ can be formulated according to Equation 2.35.

$$Nu = f(Re, Pr) = \frac{h \cdot L}{\lambda} \tag{2.35}$$

The local **convective fluid-to-wall heat transfer coefficient** h_{fw} in Barracuda® is defined by a combination of a lean gas phase heat transfer coefficient h_l and a dense particle phases heat transfer coefficient h_d. As can be seen in Equation 2.36 the contribution of the dense phase is weighted by the function f_d, which considers the influence of the time fraction of dense phase contact. In this, θ_p represents the particle volume fraction at the wall and θ_{cp} the close pack volume fraction. The latter corresponds to the counterpart of porosity. ($\theta_{cp} = 1 - \varepsilon$)

$$h_{fw} = h_l + f_d h_d \quad \text{with} \quad f_d = 1 - e^{-10(\theta_p/\theta_{cp})} \tag{2.36}$$

$$h_l = \left((c_0 Re_L^{n_1} Pr^{n_2} + c_1) \frac{k_f}{\Delta} + c_2 \right) \frac{W}{m^2 K} \tag{2.37}$$

The heat transfer coefficient in the lean phase is calculated according to Equation 2.37 and follows a correlation of Douglas and Churchill. This includes the Reynolds number of the lean phase Re_L, the Prandtl number Pr, the thermal conductivity of the fluid k_f, the cell length Δ, as well as five adjustable model parameters. According to Yang et al. [40] their default values are set to:

$c_0 = 0.46$	$c_1 = 3.66$	$c_2 = 0$	$n_1 = 0.5$	$n_2 = 0.33$

Using the density of the fluid ρ_f, the velocity of the fluid U_f, the cell length L, the viscosity of the fluid μ_f, the fluid heat capacity $c_{p,f}$ and the thermal conductivity of the fluid k_f, the Reynolds and Prandtl number in the context of the lean phase heat transfer coefficient are defined as:

$$Re_L = \frac{\rho_f U_f \Delta}{\mu_f} \qquad Pr = \frac{\mu_f c_{p,f}}{k_f}$$

The heat transfer coefficient in the dense phase is calculated according to Equation 2.38. This correlation was developed by Leva and Grummer and, in addition to the already mentioned variables, includes the particle diameter d_p [42].

$$h_d = \left(c_0 Re_p^{n_1} \frac{k_f}{d_p} \right) \frac{W}{m^2 K} \tag{2.38}$$

The particle Reynolds number is calculated as follows and the default values according to Yang et al.[40] are listed below.

$$Re_p = \frac{\rho_f U_f d_p}{\mu_f} \qquad Pr = \frac{\mu_f c_{p,f}}{k_f}$$

$c_0 = 0.525$	$n_1 = 0.75$

The local **fluid-to-particle heat transfer coefficient** is modelled in Barracuda® according a correlation proposed by McAdams:

$$h_p = \left((c_0 Re_L^{n_1} Pr^{0.33} + c_1) \frac{k_f}{d_p} + c_2 \right) \frac{W}{m^2 K} \tag{2.39}$$

The Reynolds number contained therein is determined by the density of the fluid ρ_f, the particle diameter d_p, the viscosity of the fluid μ_f and the relative velocity between particle and fluid $|U_f - U_p|$. The Prandtl number is composed analogously to the previous model.

$$Re_p = \frac{\rho_f |U_f - U_p| d_p}{\mu_f} \qquad Pr = \frac{\mu_f c_{p,f}}{k_f}$$

According to Fan et al. [9] the default values of Equation 2.39 are set in Barracuda® to:

$c_0 = 0.37$	$c_1 = 0.1$	$c_2 = 0.0$	$n_1 = 0.6$

2.4.6 Numerical solution

In Barracuda ®, the fluid phase equations are solved by a numerical control volume approach. The mass, momentum and energy conservation equations (Equation 2.18, 2.19 and 2.22) are integrated over a defined control volume respectively cell. Density, velocity and pressure of the fluid mixture are coupled by a semi-implicit pressure equation, which is derived from the fluid mass conservation equation. A conjugate gradient solver is used to solve the fluid pressure, energy and momentum equation [27].

As already mentioned, the MP-PIC method is used to describe the interaction of fluid and particle phase. Thus, particles with identical properties are aggregated into numerical parcels whose, movement is calculated using a finite difference method. The new particle position $\vec{x_p}^{n+1}$ is therefore calculated from the old one $\vec{x_p}^{n}$, under consideration of the current velocity $\vec{u_p}^{n+1}$ and the time step Δt, as follows:

$$\vec{x_p}^{n+1} = \vec{x_p}^{n} + \Delta t \, \vec{u_p}^{n+1} \tag{2.40}$$

The detailed derivation of the equation for determining the particle velocity $\vec{u_p}^{n+1}$ can be taken from O'Rourke [22].

Equation 2.40 and the corresponding velocity are calculated at the particular parcel position. The equations of the fluid phase are solved for the respective cell on the grid. In order to solve the fluid-solid interactions numerically efficiently, the discrete particle properties are mapped onto the grid and back by interpolation polynomials. In turn, fluid properties are mapped form the Eulerian grid to the parcel position [27].

Momentum properties are calculated at cell faces and scalar properties at cell centers. Therefore four sets of interpolation operators, one for the center and three for the adjacent faces, in three dimensions are required. Barracuda® uses linear interpolation operators for the x, y and z directions. The three-dimensional interpolation operator results from the product of the operators of the three spatial directions.

$$S = S^x S^y S^z \tag{2.41}$$

For a particle located at position $\vec{x_p} = [x_p, y_p, z_p]^T$, the x-directed component of the interpolation operator for the grid cell center i is an even function. It is independent of the y and z coordinates and has the following properties:

$$S_i^x(x_p) = \begin{cases} 0 & x_p \leq x_{i-1},\ x_p \geq x_{i+1} \\ 1 & x_p = x_i \end{cases} \tag{2.42}$$

Analogously, the interpolation operators can be formed for the y- and z-direction [3].

Figure 2.10 sketches the linear interpolation function for the x-direction of cell-centred variables. It is 1 in the centre of the cell and varies linearly to 0 at the centres of the neighboring cells. In the range from x_{i+1} to x_{i+1} the interpolation function can be described according to Equation 2.43.

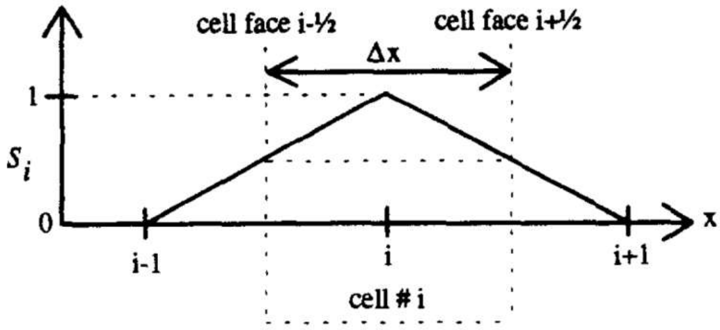

Figure 2.10: Linear interpolation function, Andrews et al. [3]

$$S_i^x = \frac{x_{i+1} - x_p}{x_{i+1} - x_i} \tag{2.43}$$

In Barracuda ®, the time step is automatically adjusted by the so-called CFL control. The Courant-Friedrichs-Lewy number expresses how many cells of the dimension Δx_{cell} a fluid with the velocity u_f will cross within a time step Δt. It can be calculated as follows:

$$CFL = \frac{u_f \Delta t}{\Delta x_{cell}} \tag{2.44}$$

The choice of the lower and upper limit of the CFL number affects the accuracy, speed and stability of the calculation. It is recommended to choose the limits between 0.8 and 1.5 [1].

3 Procedure

Based on available literature and previously performed research on the fluidized bed issue, three main geometries were chosen to investigate the flow structure and heat transfer in bubbling fluidized beds. This chapter covers the choosen geometries as well as their simulative implementation. At this point it should be mentioned that there is a large number of selectable parameters and models in Barracuda. Unless otherwise stated, the default settings recommended by the user manual [1] have been used. Furthermore, data evaluation is also discussed in this chapter.

3.1 Geometries

Since Barracuda® has to be provided with a stl-file of the flow domain, the following figures show transparent models of the geometries that can be occupied by the flow. The geometries were constructed with Creo Parametric 7.0.6.0. Technical drawings of all geometries and variants can be found in Appendix C.

Geometry 1 is a cuboid volume with a square base area and also known as Micro. The bubbling behaviour and heat transfer at the integrated tube banks will be investigated. In the range of low fluidization degrees, the heat transfer at tube banks is greater compared to single tubes in a fluidized bed. The tube banks capture rising bubbles and the collapse of these creates smaller bubbles that promote mixing compared to a few large bubbles. The heat transfer coefficient of staggered tube bundles is higher than that of in-line tube bundles [24].

Based on this, 5 different variants of Geometry 1 with different tube spacing and tube types were created. The number of used tubes is constant. The specifications of the variants are listed in Table 3.1. Geometry 1c with longitudinal fins has a surface factor of 1.5 in relation to the plain tubes. Geometries 1d and 1e were designed with a pitch of 11 mm and have 3.6 times the surface area related to the plane tubes.

Geometry	Horizontal Spacing in mm	Vertical Spacing in mm	Tube Type
1a	50	62.5	plain
1b	50	45	plain
1c	50	62.5	longitudinal fins
1d	50	62.5	transversal fins
1e	50	62.5	helical fins

Table 3.1: Variants of Geometry 1

Pictures of the volumes can be seen in Figures 3.1, 3.2, 3.3, 3.4 and 3.5.

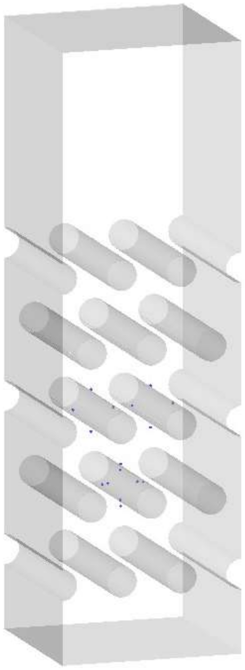

Figure 3.1: Geometry 1a

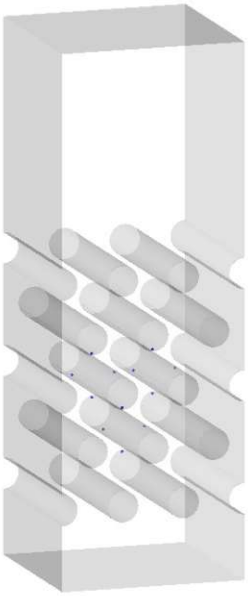

Figure 3.2: Geometry 1b

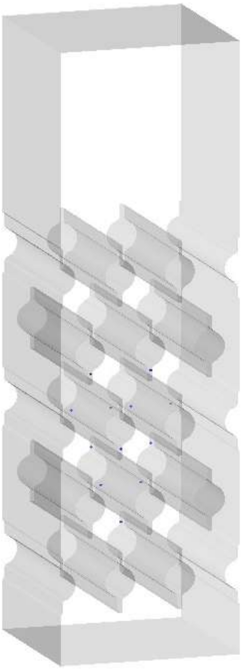

Figure 3.3: Geometry 1c

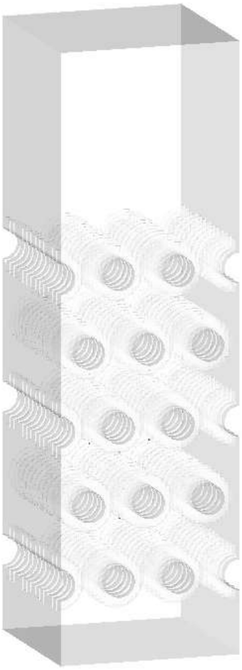

Figure 3.4: Geometry 1d

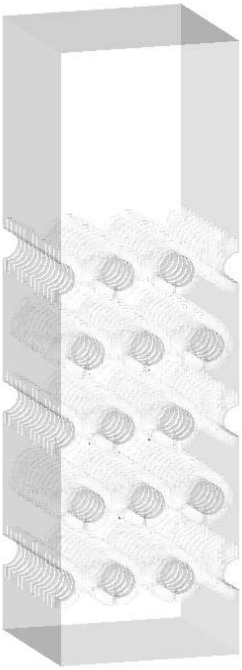

Figure 3.5: Geometry 1e view 1

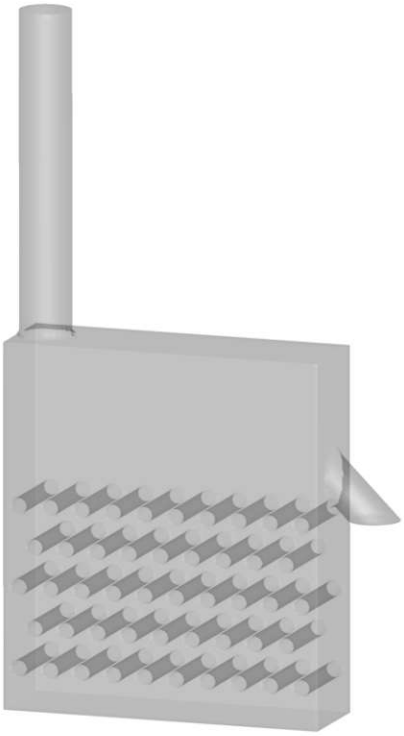

Figure 3.6: Geometry 2a

Geometry 2 represents a simplified form of the counterflow fluidized bed heat exchanger. It consists of only one fluidized zone. In the short version 2a, 10 rows of tubes are integrated and in the longer version 2b, 20. The two versions are shown in Figures 3.6 and 3.7. The cylindrical extension on the left side is used for the particle feed. The extension on the right has an elliptical basic shape in order to create an equal outlet area for the fluidized particles due to the inclination. The horizontal tube spacing is 50 mm and the vertical 62.5 mm.

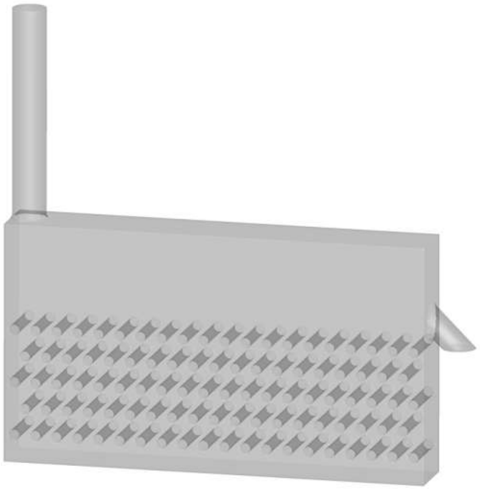

Figure 3.7: Geometry 2b

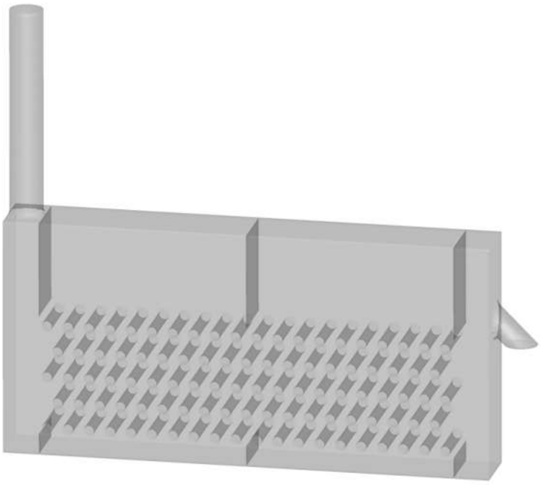

Figure 3.8: Geometry 3

Fundamentally Geometry 3 corresponds to Geometry 2b. But in Geometry 3 are 4 fluidized zones integrated that are separated from each other by baffles, as can be seen in Figure 3.8. This is to avoid bypass flows and to enable a higher heat exploitation. The identification of such phenomena and the effectiveness of the measures are to be investigated.

3.2 Modelling and simulation setup

Modelling in Barracuda® basically starts with the creation of the geometry respectively the grid, continues with the definition of particle and fluid properties and ends with the specification of initial and boundary conditions. In order to be able to follow the particle movement, fluid and particle properties, there is the possibility to position transient data points and flux planes before starting the simulation. These aspects will be briefly discussed in the following. The remaining options in Barracuda® essentially concern the numerical solver settings and the data output, as well as the options for simulating chemical reactions, which are irrelevant in the context of this work.

3.2.1 Grid

As already mentioned, the geometry of the flow volume must be provided in STL format for the creation of the grid in Barracuda®. After the import, the grid can be specified and baffles can be created.

Baffles are two-dimensional sub-grid structures with an infinitely thin wall thickness that can influence particle and fluid flow. Particles bounce off as with solid walls and for fluids a pressure drop can be induced by specifying a K-factor [1].

As discussed in Section 2.4.1, the grid size should not change significantly between adjacent cells. Therefore, for the simple geometries with plain tubes, a uniformly spaced grid was chosen. This can be seen in Figure 3.9. However, for the bigger or more complicated tube shapes, such as finned tubes and helical tubes, a compromise must be found between high resolution and the minimised number of cells for a short calculation time. As can be seen in Figure 3.10, the central area, where the points for temperature and porosity measurements are placed, has a smaller grid spacing than the areas close to the wall.

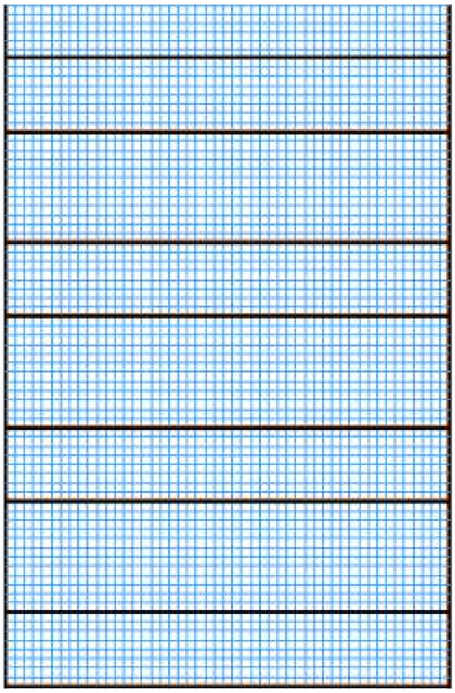

Figure 3.9: Grid Geometry 1a

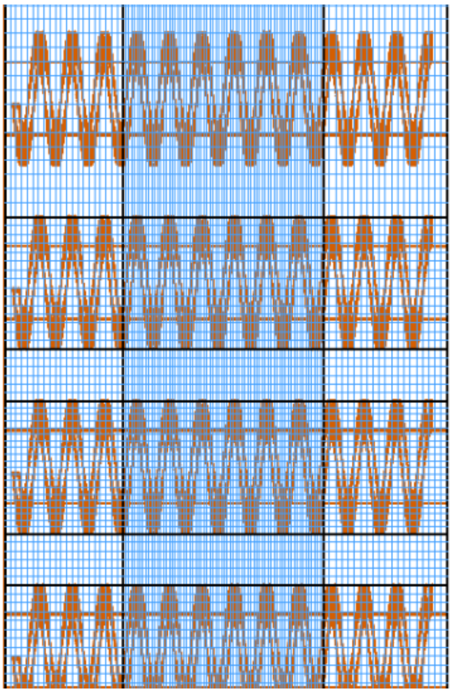

Figure 3.10: Grid Geometry 1e

3.2.2 Particles

In experiments already conducted at the Institute for Energy Systems and Thermodynamics, the particles specified in Appendix A were used. In addition to the bulk density (1340 $\frac{kg}{m^3}$) and the average grain size (146 µm), the grain size distribution is also given for the corresponding quartz sand (SiO_2). This is approximated in Barracuda® by specifying a maximum and minimum particle radius and the sphericity as a normal distribution. Furthermore, the close pack volume fraction is used to describe the particle phase. It is defined as $\theta_{cp} = \frac{\rho_b}{\rho_p}$ and corresponds to the counterpart of the fixed bed porosity using Equation 2.2. ($\theta_{cp} = 1 - \varepsilon = 0.506$)
For the particle-fluid interaction, Wen-Yu's drag model was used with the standard parameters. For the visualisation of the mixing dynamics in Geometry 2 and 3, several areas were coloured differently with so-called species, as shown in Figure 3.11. Nevertheless, these are particles with the same properties.

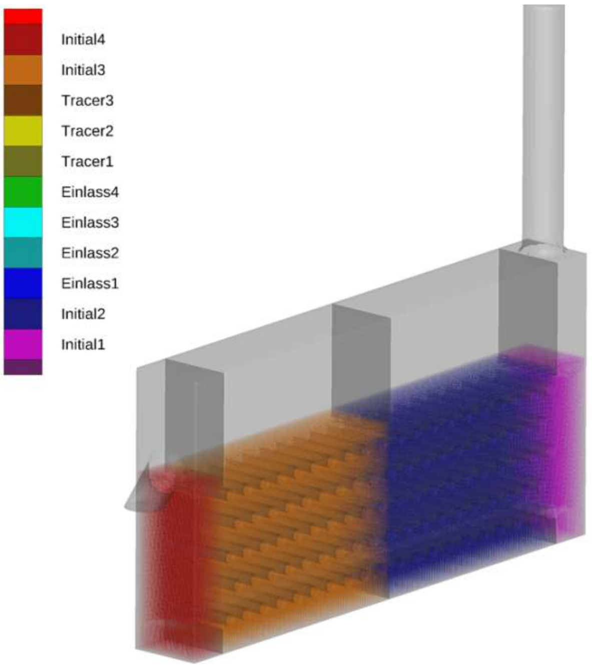

Figure 3.11: Species Geometry 3

3.2.3 Boundary and initial conditions

By default, all boundary surfaces are defined as impermeable and adiabatic in Barracuda®. In order to be able to map the desired simulation, various boundary conditions must be specified.

For the heating tube, a **thermal wall boundary condition** is specified in each case, at which a fixed surface temperature is set. These boundary conditions are marked pink in Figure 3.12. For the isothermal simulations of Geometry 2 and 3, this type of boundary condition is omitted.

Flow boundary conditions were defined for fluidization from below, marked red in Figure 3.12. This allows the temperature, pressure and velocity with which the air enters the system to be defined. In practice, fluidization is realized by sintered plates, where air can be introduced into the fluidized bed from below through the fine pores of the plates. In all simulations, the fluidization velocity corresponds to four times the minimum fluidization velocity, which is equivalent to fluidization degree 4. The minimum fluidization velocity was determined with Equation 2.6 and the constants of Richardson [23]. The particle feed into the system can also be defined via flow boundary conditions. This is applied in the simulations of Geometry 2 and 3.

Pressure boundary conditions are used for particle and air outlet. These are coloured yellow in Figure 3.12. A pressure of 10^5 Pa and a temperature of 298 K were defined for this. Depending on whether it is a particle outlet or not, the particle behaviour was defined accordingly.

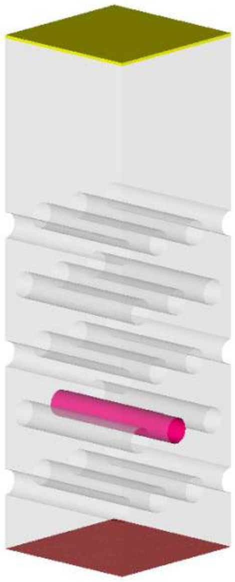

Figure 3.12: Boundary conditions Geometry 1a

All simulations are carried out with the same particle and fluid starting temperatures of 298 K and a fluid pressure of 10^5 Pa. Only the particle fraction is selected depending on the geometry.

3.2.4 Data output

For the data evaluation, representative points in the system must be defined first at which fluid and particle properties are to be output. In order to avoid boundary effects, these are placed close to the symmetry plane. In the specific case, mainly particle temperature and particle volume fraction are of interest, but many more variables can be output. After defining the so-called transient data points in Barracuda®, the specific cell data for each time step are written to a transient data file. The transient data points for the temperature determination of the particles are located at a distance of 5 mm from the outer tube diameter, as can be seen in Figure 3.13 and 3.15. The transient data points for the determination of the particle volume fraction are located at a distance of 5 mm from the inner tube diameter, as can be seen in Figure 3.14 and 3.16.

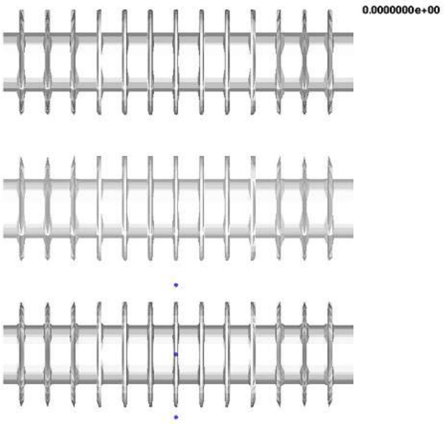

Figure 3.13: Transient data points for temperature, Geometry 1d

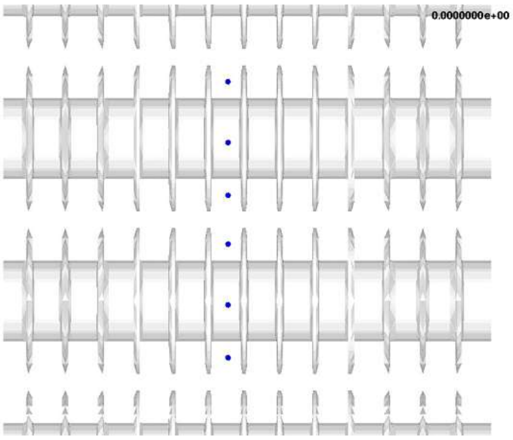

Figure 3.14: Transient data points for particle volume fraction, Geometry 1d

For tracking particle movements, Barracuda® offers the application of Flux Planes. These are two-dimensional planes that register every particle passing through. Variables such as time integrated fluid mass crossing flux plane and particle mass flow rate are written to a data file for each time step. The directional dependency of all variables can also be output. Figure 3.17 shows an example of the flux planes used to investigate the particle movement of Geometry 2b.

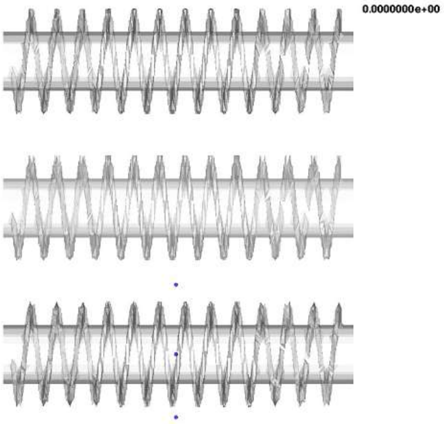

Figure 3.15: Transient data points for temperature, Geometry 1e

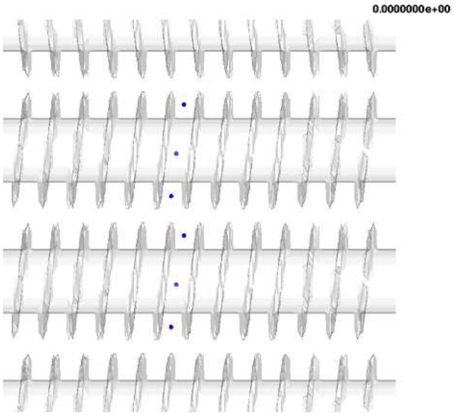

Figure 3.16: Transient data points for particle volume fraction, Geometry 1e

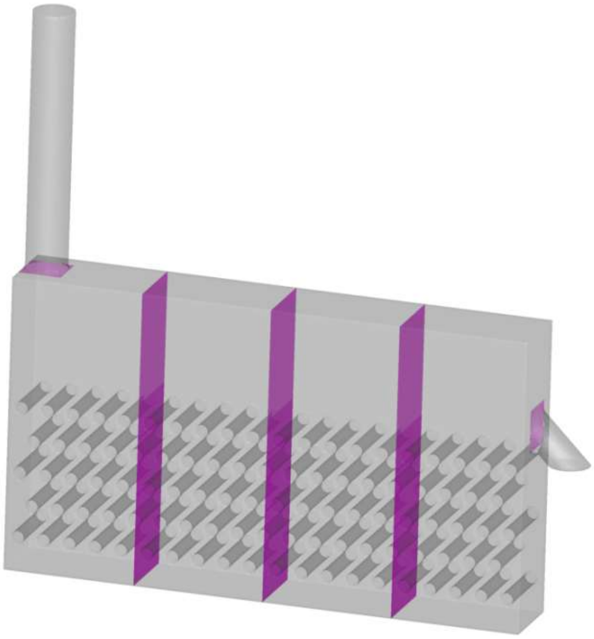

Figure 3.17: Flux planes, Geometry 2b

3.3 Evaluation

The collected data can be analysed in different ways. This and other things to consider in the evaluation will be dealt within this section.

3.3.1 Data analysis

Depending on the version, Barracuda® provides various visualization tools for graphical data evaluation. For version 17.3.1 the General Mesh Viewer was used for the 3D visualization of the simulation data, for version 21.1.1 Tecplot 360 EX 2021 R2. These applications turned out to be very helpful, especially for a first plausibility check and the visualisation of flow structures.

For the numerical evaluation of the data files of the transient data points and the flux planes, as well as the further processing of the data, MATLAB R2020b was used. The main code sections can be found in Appendix B.

3.3.2 Averaging

As already mentioned in Section 2.4.6, the time step size is dynamically adjusted by the so-called CFL control. Therefore, the results are available at irregular time intervals. A direct averaging of the values would lead to incorrect results, as areas with smaller time steps would be weighted greater. Equation 3.1 was applied for the averaging in this thesis.

$$\overline{x} = \frac{1}{t_2 - t_1} \sum_{t_1}^{t_2} x_i(t_i) \cdot \Delta t_i(t_i) \tag{3.1}$$

In this, the mean value $\overline{x}$ in the period t_1 to t_2 is formed from the sum of each value x_i weighted with the associated step size Δt_i and divided by the complete time span.

4 Simulations and results

In this chapter, all essential simulations and the corresponding results are discussed. First, uncertainties regarding minimum fluidization and degree of fluidization will be addressed. Then the heat transfer behaviour and the flow characteristics of the selected geometries are discussed in detail.

4.1 Verification of minimum fluidization

As already mentioned in Section 2.1.3, there are numerous different correlations for the determination of the minimum fluidization velocity, which all show different results. Since the minimum fluidization velocity is an essential operating parameter of fluidized beds, this section is used to evaluate the correlations, compare it to results from a simulation and determine the extent of the deviation.

Thanheiser [33] demonstrates the significant influence of the fluidization degree on the heat transfer behaviour at the examined test rigs. Therefore, a verification of the minimum fluidization velocity provides the basis for a classification and comparability of the results produced in this diploma thesis. Such a verification was already carried out by Heindl [13], but with a different particle sizing.

As already described in Section 2.1.3, the measurement of the pressure drop across the bed height provides information about the point of minimal fluidization. For the simulative determination, a simple cuboid fluidized bed apparatus with constant sand content is modelled in Barracuda® and the velocity profile shown in Figure 4.1 is applied as flow boundary condition.

In the experimental determination it must be ensured that the loosest bulk is present in the fixed bed. If the bed is densified, a greater pressure may occur and thus another minimum fluidization velocity. For this reason, fluidization was initially carried out well above the point of minimum fluidization, but this would not have been possible anyway according to the mathematical model. Then the fluidization velocity was gradually increased and at a certain point lowered again. The blue line in Figure 4.2 shows the resulting pressure drop. Linear regression was used to replicate the theoretically linear respectively constant behaviour of the three states. The intersections of these red lines give two time values from which the minimum fluidization velocity can be derived in Figure 4.1. This results in 0.0187 m/s.

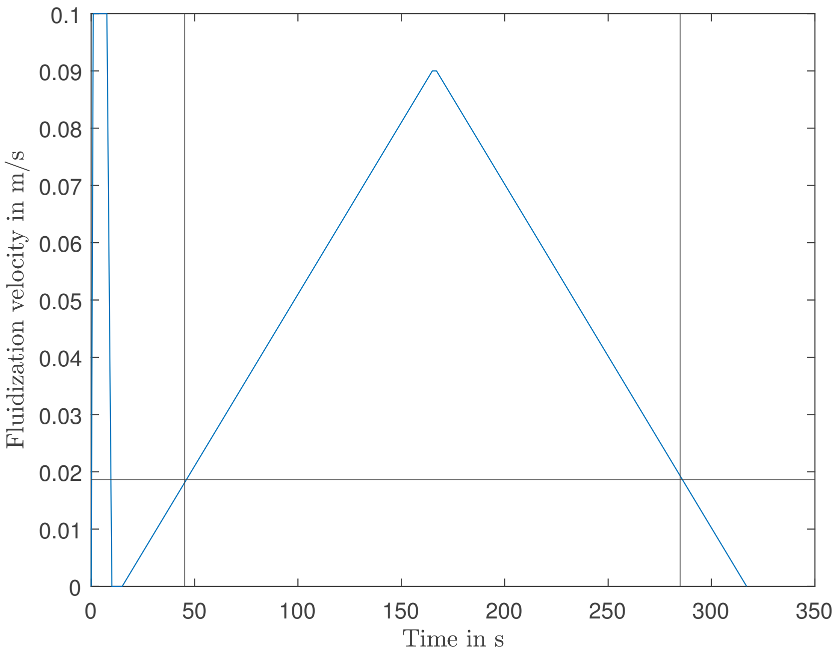

Figure 4.1: Fluidization velocity

Compared to Figure 2.3 and Heindl's [13] results, there are significant deviations in the curve of the pressure drop. One concerns the smooth transition between the states and the other the noise of the simulation data in the fluidized bed area.

According to Hofbauer [15], the transition from the fixed bed to the fluidized bed is only pronounced when there is a very narrow distribution of particles. If a wide spectrum of particles is present, the transition is gradual. At first, the particles with the smallest diameter begin to swirl, whereas the larger particles are not yet in a swirl state. Here the minimum fluidization velocity is determined by extending the straight lines in the fixed bed and fluidized bed and bringing them to the point of intersection. In contrast to Heindl [13], the real grain size distribution was simulated here according to the information provided by the sand manufacturer, available in Appendix A.

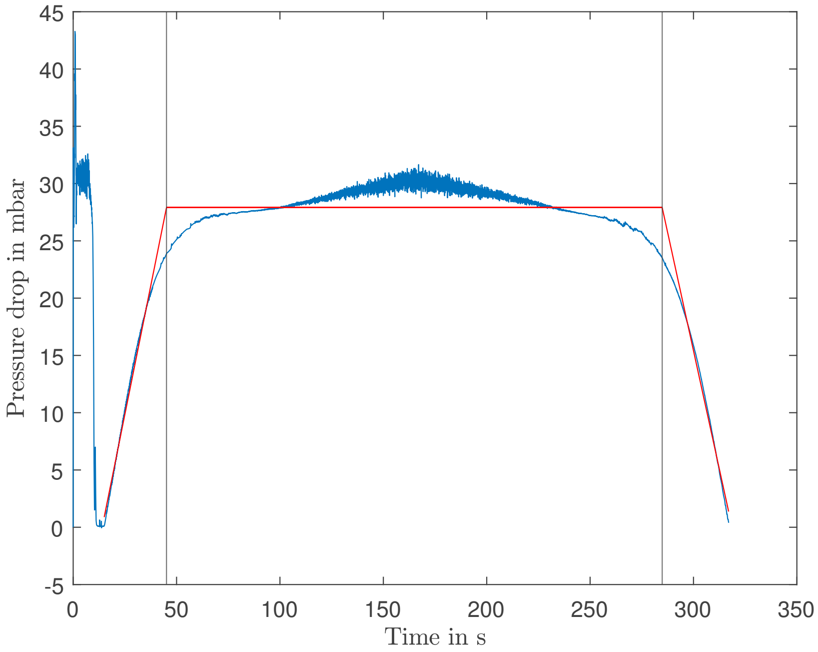

Figure 4.2: Pressure drop

Furthermore, an unnecessarily high maximum fluidization was applied, which causes pneumatic transport of the small particles and thus pressure fluctuations.

Author(s)	v_{mf} in $\frac{m}{s}$	rel. deviation
Simulation	0.0187	0
Richardson [23]	0.0215	-0.1514
Wen and Yu [36]	0.0184	0.0171
Bourgeis and Grenier [6]	0.0227	-0.2160
Babu, Shah and Talwalker [4]	0.0389	-1.0831
Biń [5]	0.0214	-0.1461

Table 4.1: Result matrix for the minimum fluidization velocity

Table 4.1 compares the obtained results and the calculated correlations. Although the density and diameter ranges, given for all correlations except for Wen and Yu, correspond to the investigated particles, paradoxically Wen and Yu show the smallest deviations from the simulated value. Richardson's correlation, which is mainly used in the course of the SandTES research, provides reasonable values with a relative deviation of -15% in relation to the simulated results. Therefore, for the sake of comparability, the correlation of Richardson was used as the basis for the fluidization degree in this work. This means that the used fluidization degree relative to the numerical determined minimum fluidization velocity was 15% higher, hence 4.6 and not 4 as originally intended.

4.2 Heat transfer behaviour

The heat transfer behaviour between particles and surfaces in fluidized beds is described and quantified according to Equation 2.13. For this, in addition to the constant kept surface temperature, the particle temperature and heat transfer rate are required.
In the following sections these values are determined in order to finally get the heat transfer coefficient of the different variants.

4.2.1 Particle temperature

The particle temperature was tracked at four different points using transient data points. These are located at a distance of 5 mm from the outermost tube diameter above, right, below and left of the tube.
Analogous to the particle temperatures of Geometry 1a shown in Figure 4.3, this was carried out for Geometries 1b, 1c, 1d and 1e. In the plots of of the temperature curves, outliers with a particle temperature of 0 K can be found repeatedly. This is due to the point-like property of the tracking location. Since only the particle temperature is output, the temperature output is 0 K, if at a certain time step there is only fluid and no particle at the transient data point. Since this would falsify the heat transfer coefficient, in the case of an outlier the 0 K value was replaced with the temperature value of the previous time step and then the mean value was calculated from all four measured values. This curve is marked as processed mean in Figure 4.3.

Figure 4.4 (a) to (e) show the particle temperature distributions of all tube types at the simulation time of 20 s. The thinner the areas are coloured, the lower the particle temperature. The colour red indicates the highest particle temperature in these figures. The different heat input into the systems can already be guessed at this point.

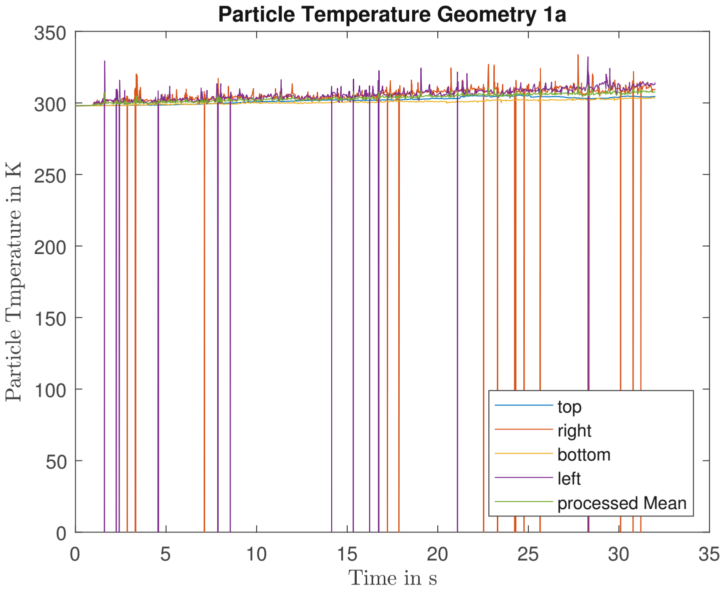

Figure 4.3: Particle Temperature Geometry 1a

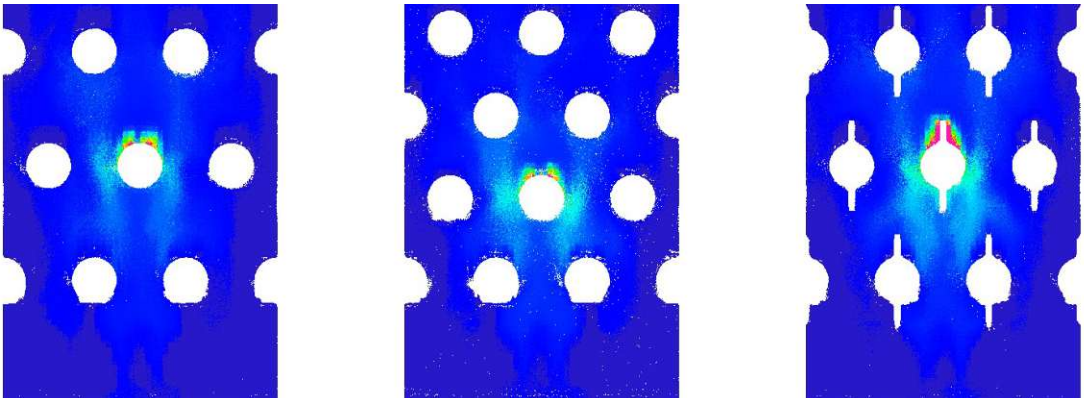

(a) 1a (b) 1b (c) 1c

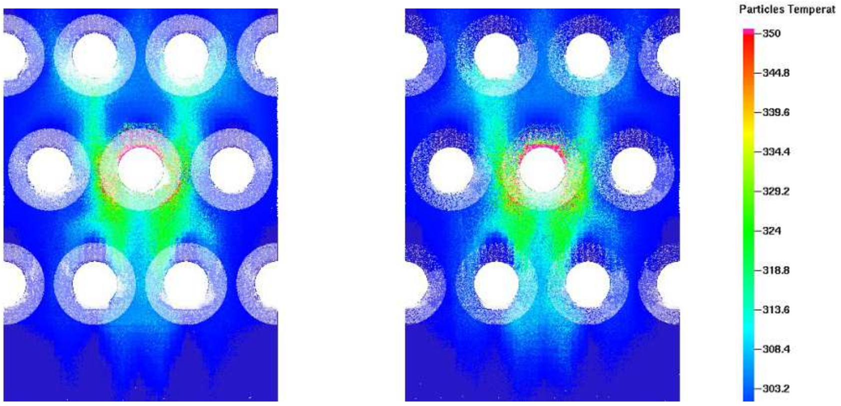

(d) 1d (e) 1e (f) Legend

Figure 4.4: Temperature distribution 20 s

4.2.2 Heat transfer rate

Barracuda® outputs the heat transferred by all thermally active surfaces per time step. Since in the present simulations all surfaces except of the one heat exchanger tube are thermally inactive, the heat transfer rate can thus be used directly. Figures 4.5, 4.6, 4.7, 4.8 and 4.9 show the temporal course of the heat transfer rates of Geometries 1a, 1b, 1c, 1d and 1e calculated with default constants for heat transfer. Since these quantities are subject to relatively high fluctuation, the mean value in the period 0 - 30 s was calculated according to Equation 3.1 and added for better comparison.

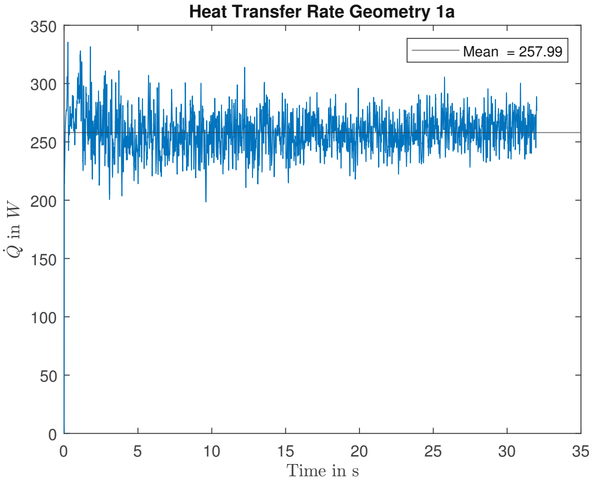

Figure 4.5: Heat Transfer Rate Geometry 1a

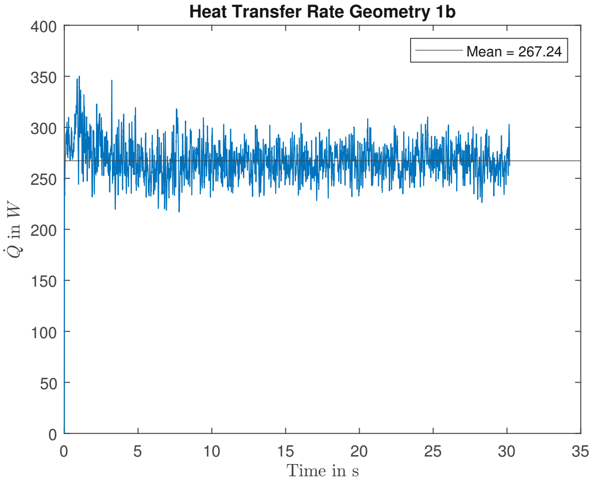

Figure 4.6: Heat Transfer Rate Geometry 1b

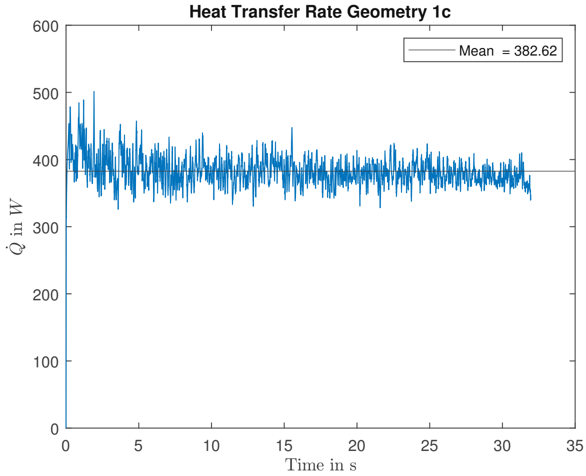

Figure 4.7: Heat Transfer Rate Geometry 1c

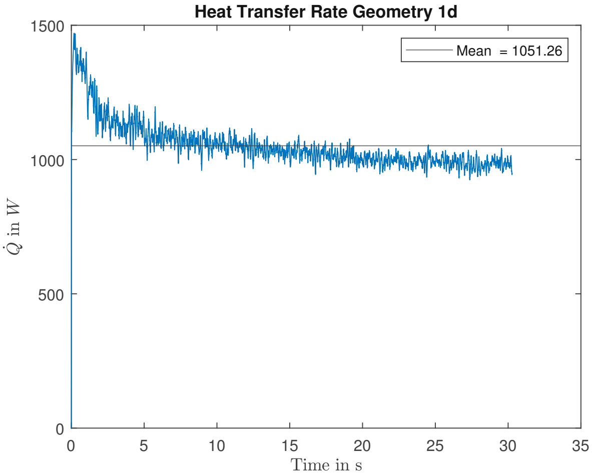

Figure 4.8: Heat Transfer Rate Geometry 1d

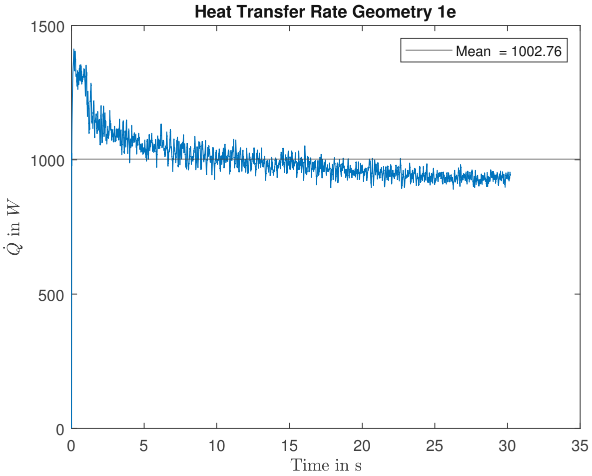

Figure 4.9: Heat Transfer Rate Geometry 1e

Compared to the remaining geometries, the largest amount of heat could be transferred in Geometry 1e and 1d, whereby the heat transfer rate of Geometry 1d is even a bit higher. A asymptotic behaviour was also observed in both of these geometries. The initial heat transfer is very high and decreases over time. This can be explained by the reduction of the driving temperature difference. At this point it should also be mentioned that no fin efficiencies were taken into account in these investigations. This is assumed due to the good heat conduction properties of the pipe material and the low wall thicknesses. An estimation based on Hesselgreaves et al. [14] gave a fin efficiency for the transversal fin in the order of 0.98. This justifies the simplification in the context of this basic research.

4.2.3 Heat transfer coefficient

In order to get to the course of the heat transfer coefficient, Equation 2.13 was evaluated for each time step with the corresponding heat transfer rate from Section 4.2.2 and the processed mean sand temperature from Section 4.2.1. Therefore, this is also the heat transfer coefficient averaged over the tube surface. Numerous works, such as those of Saxena [24] and Sung et al. [17], report that the heat transfer coefficient varies along the pipe circumference. The highest heat transfer coefficients were identified at the sides and bottom, while a defluidized cap forms at the top of the tubes and leads to a reduced heat transfer.

In addition, the temperature effect should be mentioned. This means that compared to ambient conditions, the heat transfer coefficient at 800 °C is up to 200 $\mathrm{W/m^2K}$ higher. This is attributed to increased gas thermal conductivity and increased radiant heat transfer at higher temperatures [18].

However, these simulations were carried out with a tube temperature of 498 K and without selecting a radiation model.

Figures 4.10, 4.11, 4.12, 4.13 and 4.14 show the heat transfer coefficient curves of Geometries 1a, 1b, 1c, 1d and 1e. Again, Equation 3.1 was used to average the heat transfer coefficient over the time course of 30 s for better comparison.

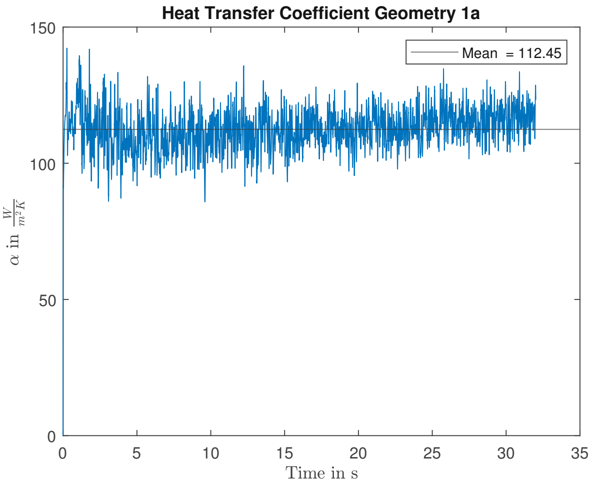

Figure 4.10: HTC Geometry 1a

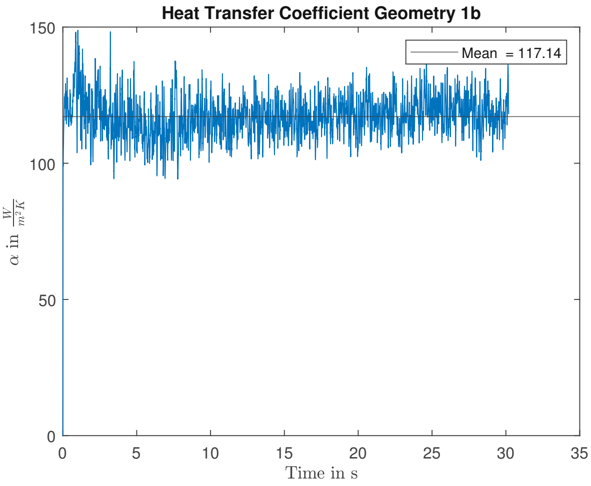

Figure 4.11: HTC Geometry 1b

As can be seen in Figures 4.10 and 4.11, an increase in the heat transfer coefficient is possible by reducing the vertical tube spacing. The tube geometry and all other simulation settings are kept identical.

All mean heat transfer coefficients and mean heat transfer rates together with the surface area multiplier and the surface sizes used for the calculation are listed in Table 4.2. The surface size was provided by Barracuda® and results from the discretisation respectively grid generation.

Compared to experimentally determined heat transfer coefficients, such as those of Thanheiser [33], a qualitative agreement of the experimental results can be confirmed. When comparing the average heat transfer coefficients of Geometry 1a and 1b, an increase could be observed. A similar trend was found in the experimental setup. However, the simulated heat transfer coefficients are much lower than the experimentally determined values. The heat transfer coefficients determined by Heindl [13] also show this circumstance. Such a quantitative deviation but agreement

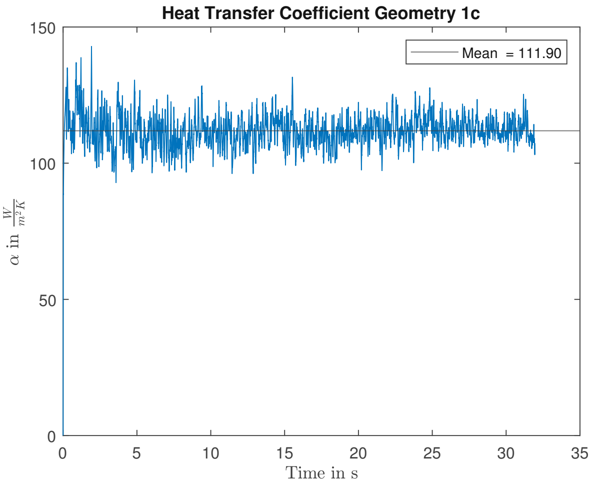

Figure 4.12: HTC Geometry 1c

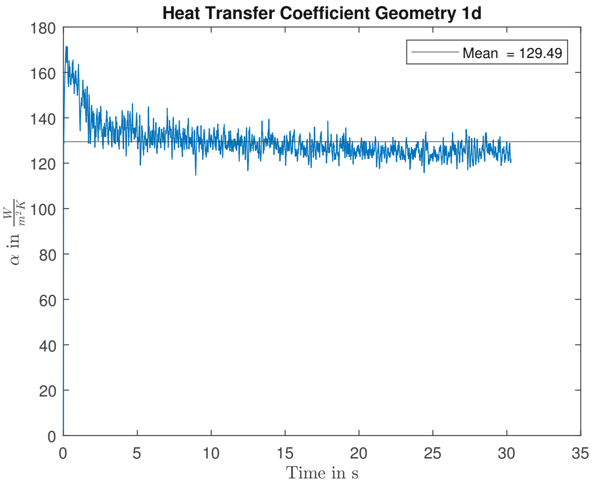

Figure 4.13: HTC Geometry 1d

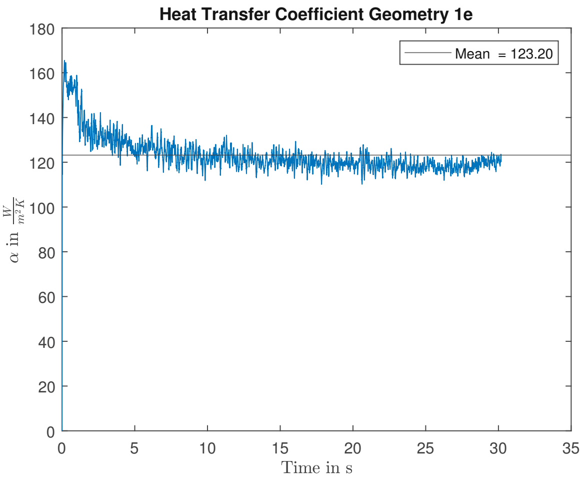

Figure 4.14: HTC Geometry 1e

Geometry	$\overline{\dot{Q}}$ in W	A in m^2	Area multiplier	$\overline{\alpha}$ in $\frac{W}{m^2K}$
1a	257.99	0.01180	1	112.45
1b	267.24	0.01180	1	117.14
1c	382.62	0.01773	1.5	111.90
1d	1051.26	0.04286	3.6	129.49
1e	1002.76	0.04267	3.6	123.20

Table 4.2: Heat Transfer Results

of trends was also affirmed by Zhang et al. [42]. They identified the cause for the quantitative deviation in the correlation for heat transfer in the dense phase (Equation 2.38). The correlation was obtained from a fluidized bed of larger sized particles and seems to be inappropriate for smaller particle diameters. Zhang et al. [42] suggest the use of another correlation, such as the one of Vreedenberg [34], for a better agreement of the simulation with the experimental results. Vreedenberg's empirical correlation was obtained for smaller particle sizes and is shown in Equation 4.1. In addition to the model already explained, it contains the porosity ε. Since only the parameters of the heat transfer models can be changed in Barracuda® and not the structure of the correlations, the proposed model could not be verified.

$$h_d = \left(\frac{k_f}{d_p} 0.66 Pr^{0.3} Re^{0.44} \left(\frac{\rho_p(1-\varepsilon)}{\rho_f \varepsilon}\right)\right) \frac{W}{m^2K} \tag{4.1}$$

4.2.4 Parameterising the fluid-particle heat transfer coefficient

Through contact with CPFD support, it was recommended that the fluid-to-particle heat transfer coefficient (Equation 2.39) should be adjusted, by way of constants. The ranges of the constants are recommended as follows:

$c_0 = 0.6 - 1.8$	$c_1 = 2$	$c_2 = 0.0$	$n_1 = 0.5$

They argue that with convective heat transfer in Barracuda®, no energy is exchanged directly between a particle and the wall. It is all transferred from particles to fluid and then fluid to other particles or walls, unless a radiation model is selected. So if the heat transfer between particles and fluid is low then the heat transfer from fluid to wall may also be low. Only if the parametrisation of the fluid-particle heat transfer coefficient does not yield the targeted results, the correlation of the fluid-wall heat transfer coefficient should be re-parametrised.

The simulation of Geometry 1a with the parameters for the fluid-particle heat transfer listed above and $c_0 = 1.8$ was carried out. In order to be able to compare the simulation results with experimentally determined results, identical initial and boundary conditions as specified in Thanheiser's [33] MICRO Rig with sandTES-spacing experiment were chosen.

The experiments made by Thanheiser [33] gave results in the order of 250 W/m^{2}K at fluidization degree 4. As can be seen in Figure 4.15, an evaluation of the simulation results showed an average heat transfer coefficient of 126.39 W/m^{2}K. Thus, the new parameterisation of the fluid-particle heat transfer coefficient still led to a deviation by a factor of 2.

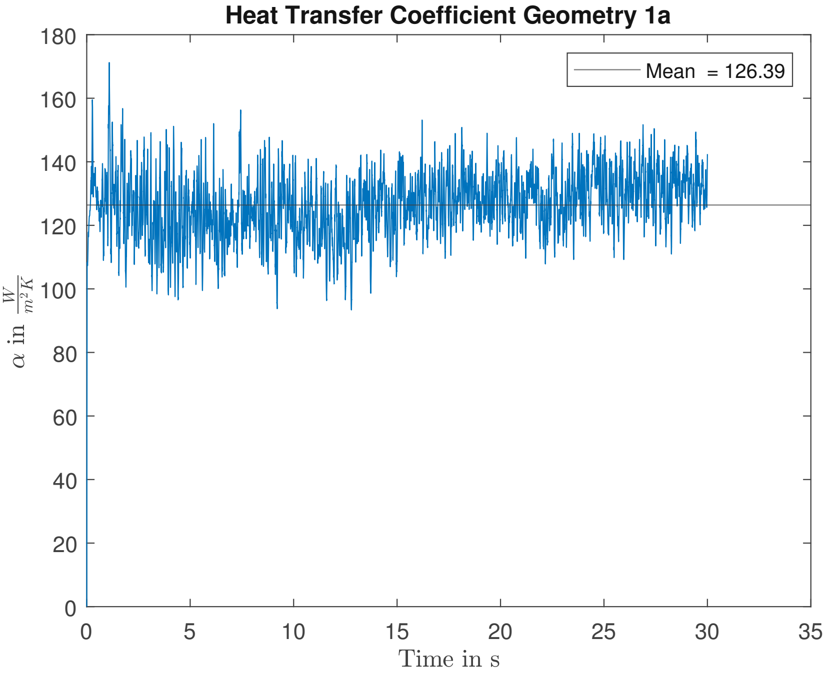

Figure 4.15: HTC Geometry 1a with modified fluid-particle heat transfer correlation

4.2.5 Parameterising the fluid-wall heat transfer coefficient

Since the new parameterisation of the fluid-particle heat transfer coefficient did not lead to the expected results, the parameters of the fluid-wall heat transfer coefficient correlation are now modified.

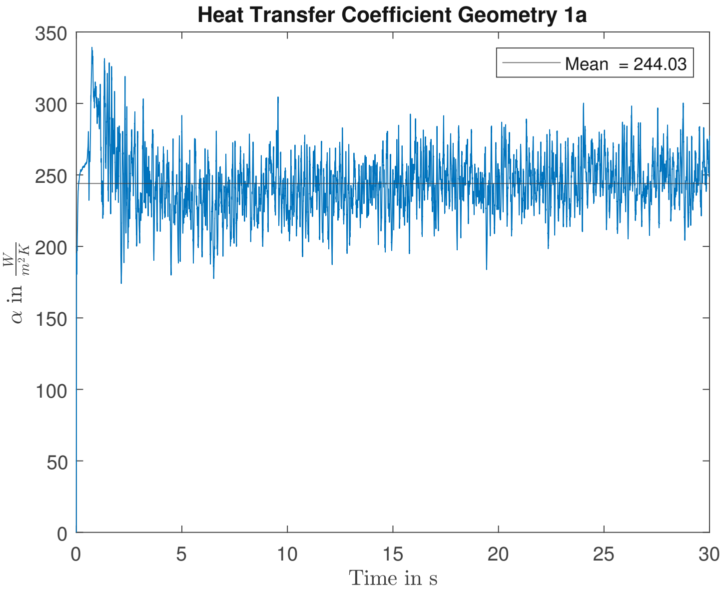

Figure 4.16: HTC Geometry 1a with modified fluid-particle and fluid-wall HT correlation

In particular, the parameter c_0 of Equation 2.38 for the dense phase is varied from 0.525 to 1.575. The parameters of the fluid-particle heat transfer coefficient were set to the same values as in Section 4.2.4. The parameter c_0 was chosen to be 1.8 according to the upper limit communicated by Barracuda®.

As can be seen in Figure 4.16, a heat transfer coefficient of 244.03 W/m^{2}K is achieved with the new parameterisation. This agrees in terms of magnitude with the values determined experimentally by Thanheiser [33].

For the direct comparison, the simulations of the geometries 1a, 1b and 1d were carried out with the new parameterisation of the heat transfer and a surface temperature of 498 K. The results are shown in Table 4.3.

Geometry	$\overline{\dot{Q}}$ in W	A in m^2	$\overline{\alpha}$ in $\frac{W}{m^2K}$
1a	521.62	0.01180	234.30
1b	528.83	0.01180	240.30
1d	1884.39	0.04286	243.90

Table 4.3: Heat transfer results with new parameterisation

Heat transfer coefficients of the same order of magnitude were found for all geometries, whereby the highest heat transfer coefficient was determined for the geometry with finned tubes. Again, the smaller vertical tube spacing causes a slightly higher heat transfer coefficient.

4.3 Flow characteristics

In this chapter, the flow characteristics of the geometries mentioned in Chapter 3.1 are investigated. In particular, the influence of the different tube types on the bubble frequency is investigated in realtion to the heat transfer. In addition, the particle movement of countercurrent fluidized bed heat exchangers without and with auxiliary measures is analysed.

4.3.1 Numerical determination of the bubble frequency

As already discussed in Section 2.3.2, bubble formation and the associated particle convection has a significant impact on bubbling fluidized beds. It is important to understand how bubbles form and how they behave within bundles of horizontal heat exchanger tubes. This allows conclusions to be drawn about characteristic properties, such as heat transfer capability between the bed and immersed surfaces.

Analyzing bubble flow patterns in fluidized beds is challenging. Various experimentally approaches, like measuring pressure fluctuations, x-ray measurements, capacitance-based imaging, and infrared transmitter-detector were applied.[38]

In this work, the bubble frequency at different locations of the fluidized bed is determined numerically. For this purpose, transient data points were set in Barracuda® at a horizontal distance of 5 mm from the outer diameter, at which the particle volume fraction is delivered at each time step. In post processing with MATLAB R2020b, the particle volume fraction profile is examined with regard to local minima. Every local minimum at which the particle volume fraction approaches or reaches zero corresponds to the presence of a bubble. The temporal extension of the minimum provides information about the bubble size. Due to the fact that bubbles in fluidized beds are not completely free of solids and the point-like property of transient data points, a local minimum is detected at a particle volume fraction less than 0.2.

To determine the bubble frequency on a horizontal tube, the transient data points to the left and right of the tube were used for post processing. As can be seen in Figure 4.18, the number of local minima, left n_l and right n_r, was determined. As a result bubble frequency was calculated according to Equation 4.2.

$$f_B = \frac{(n_r + n_l)/2}{\Delta t} \tag{4.2}$$

Since the bubbles almost always alternate between the left and right of the tube, the bubble frequency is formed from the average of the two numbers and the corresponding time interval Δt. This is often referred to as half bubble frequency.

For the verification of this method, the processed particle volume fraction of Geometry 1b was compared with screenshots from the graphical output of the same period provided by Barracuda®. Looking at the central tube in Figure 4.17(a), bubble formation can be observed on the right side. Shortly after time point 17.30 s in Figure 4.17(b), the bubble is fully developed and detaches. Comparing this with figure 4.18, a local minimum could be identified corresponding to this point in time. The same applies, for example, to the bubble that is already in the process of detachment at 17.40 s on the left side.

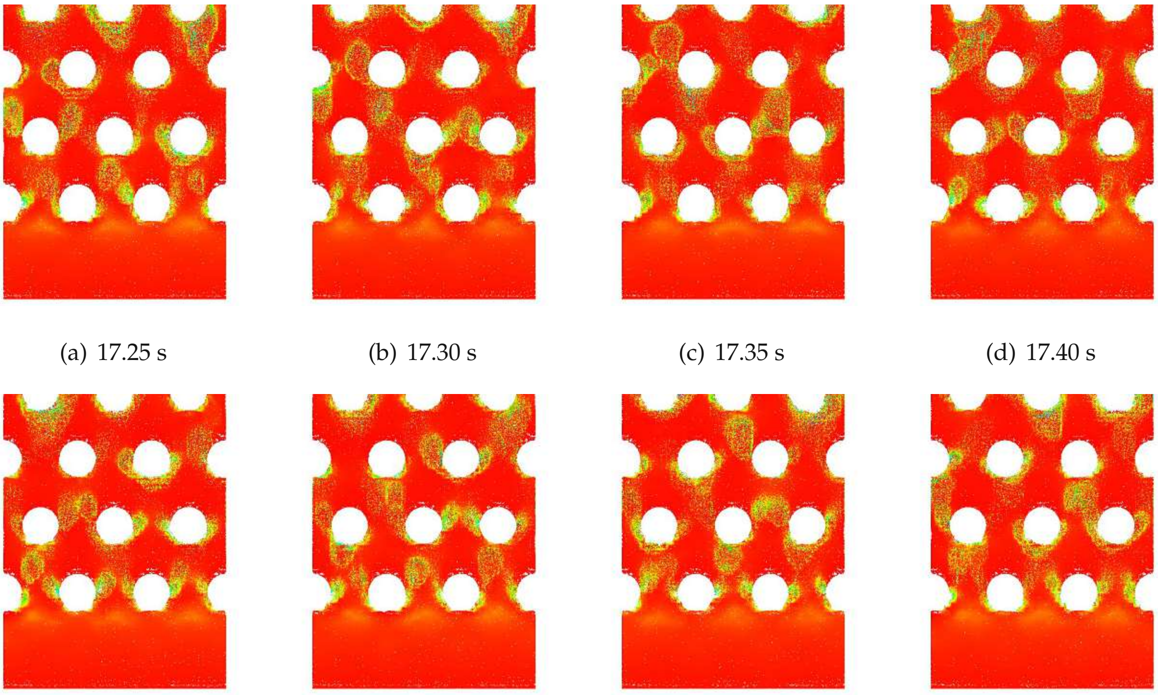

(a) 17.25 s (b) 17.30 s (c) 17.35 s (d) 17.40 s

(e) 17.45 s (f) 17.50 s (g) 17.55 s (h) 17.60 s

Figure 4.17: Verification bubble frequency

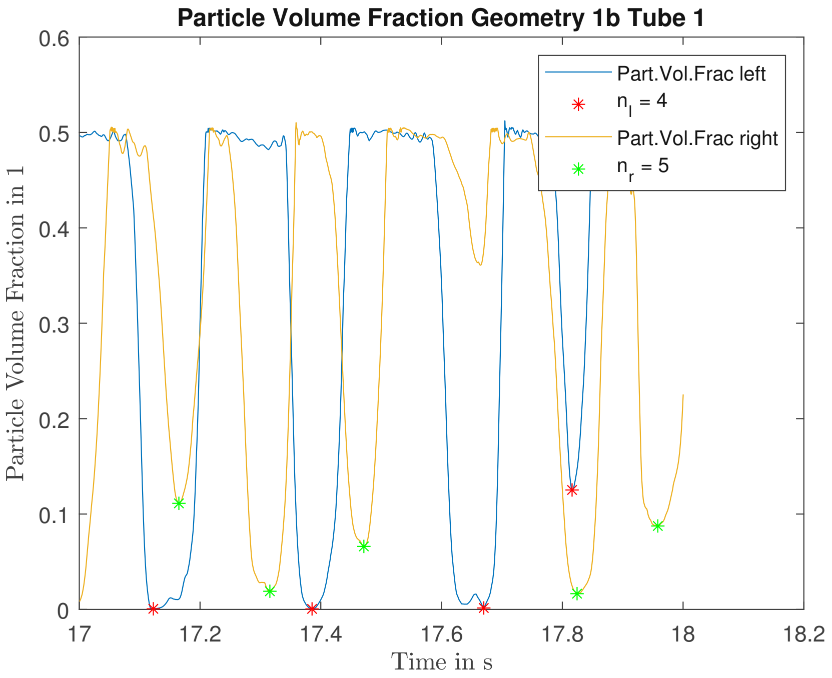

Figure 4.18: Number of bubbles, Geometry 1b

4.3.2 Bubble frequency

The method explained in Section 4.3.1 is now applied to all variants of Geometry 1. Specifically, this was applied to the central tube (Tube 1) of the second tube layer from below and the two complete tubes one layer above (Tubes 2 and 3), illustrated in Figure 4.19.

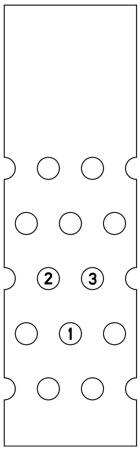

Figure 4.19: Tube numbering

The result of Tube 1 for Geometry 1a and 1b can be found as examples in Figures 4.20 and 4.21. The number of identified local minima respectively bubbles to the left and right of the corresponding tubes are given in these Figures.

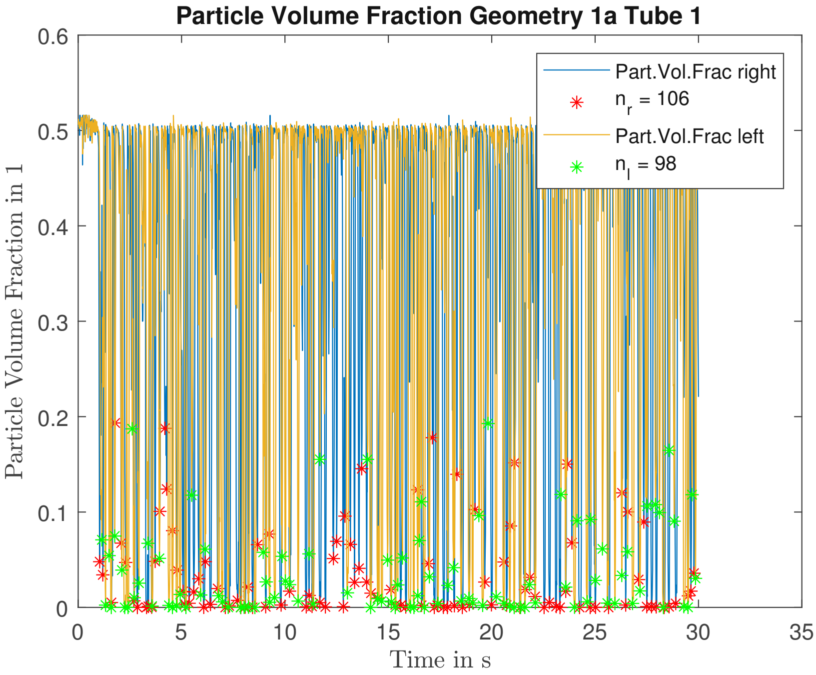

Figure 4.20: Number of bubbles, Geometry 1a Tube 1

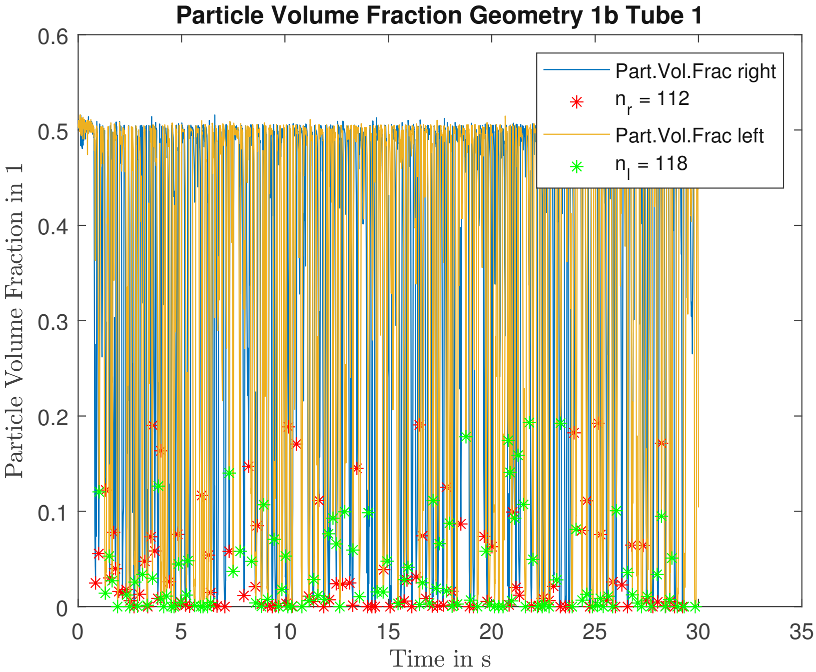

Figure 4.21: Number of bubbles, Geometry 1b Tube 1

If Equation 4.2 is now evaluated with the identified bubble numbers, the bubble frequencies can be calucalted. Gathering all information and including the results from Section 4.2.3 for Tube 1 with the default values for heat transfer leads to Table 4.4.

Geometry	Tube 1	Tube 2	Tube 3	$\bar{\alpha}$ in $\frac{W}{m^2K}$
1a	3.40	2.82	3.23	112.45
1b	3.83	3.22	2.87	117.14
1c	3.38	3.17	3.10	111.90
1d	4.23	3.78	3.95	129.49
1e	4.30	3.88	3.53	123.20

Table 4.4: Bubble frequency in $1/s$, reference period 30 s

This generally shows a higher heat transfer coefficient with increasing bubble frequency of the Tube 1. In Geometry 1a to 1d, an almost linear correlation between bubble frequency and heat transfer coefficient can be detected. Only in Geometry 1e a deviation of this trend was observed, as a higher bubble frequency in relation to the heat transfer coefficient was observed there.

4.3.3 Spatial dependence of the bubble frequency

Fluidized bed heat exchangers on an industrial scale can have much larger dimensions than previously simulated. In particular, the flow conditions that change with increasing height and the associated heat transfer behaviour are of considerable interest. Therefore, this section is used to investigate the bubble frequency at all tube bundle levels, as well as the heat transfer at selected heights.

In addition, the real fluidization conditions were approximated by modelling the sinter plate. This was done by placing a baffle at a distance of 10 mm from the bottom and defining a linear pressure drop. A K-factor of 800 was chosen. Figure 4.23 shows the particle volume fraction of the variant with the imitated sintering plate. Compared to the simple variant, shown in Figure 4.22, no difference in bubble formation was observed.

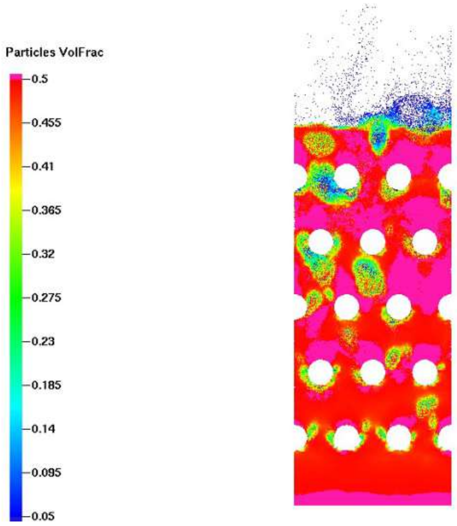

Figure 4.22: Geometry 1a particle volume fraction

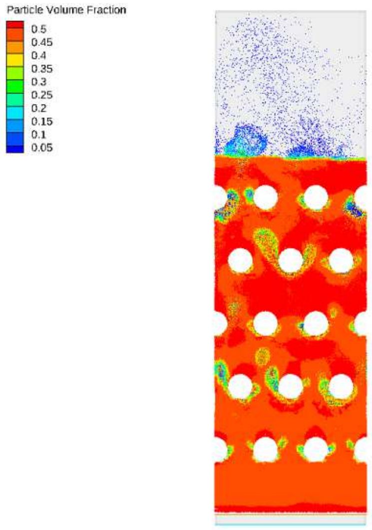

Figure 4.23: Geometry 1a particle volume fraction with baffle

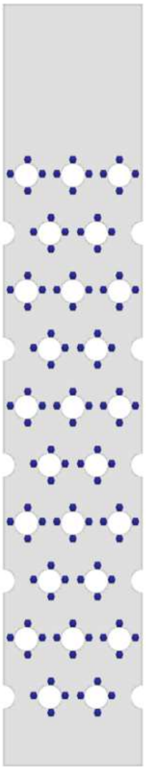

Figure 4.24: Geometry 1a double height transient datapoints

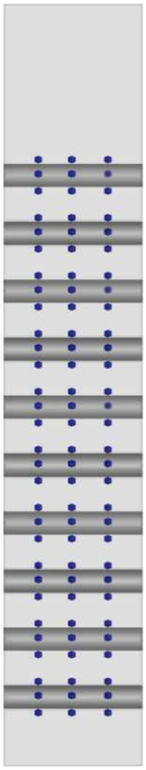

Figure 4.25: Geometry 1a double height transient datapoints side view

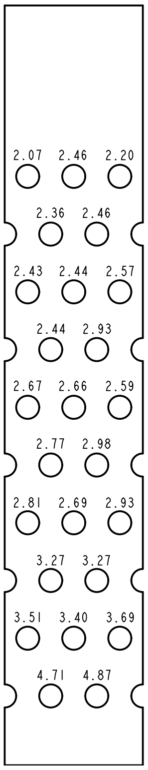

Figure 4.26: Geometry 1a double height bubble frequency in $1/s$

Figure 4.24 and 4.25 show about 300 different transient data points recording particle volume fraction and temperature at each time step. In this variant of Geometry 1a, twice as many tube levels were simulated to determine the dependence of bubble frequency on height. Figure 4.26 provides an overview of the bubble frequencies determined via the transient data points. These are noted above the corresponding tube. Since the bubble frequency was determined not only in the symmetry plane but also at two other points per tube, the average of the three results is shown in Figure 4.26. A clear decrease of the bubble frequency with increasing height is recognisable.

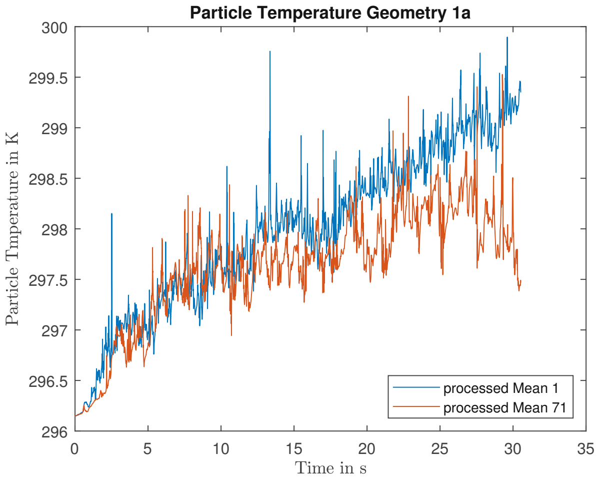

Figure 4.27: Geometry 1a double height particle temperature

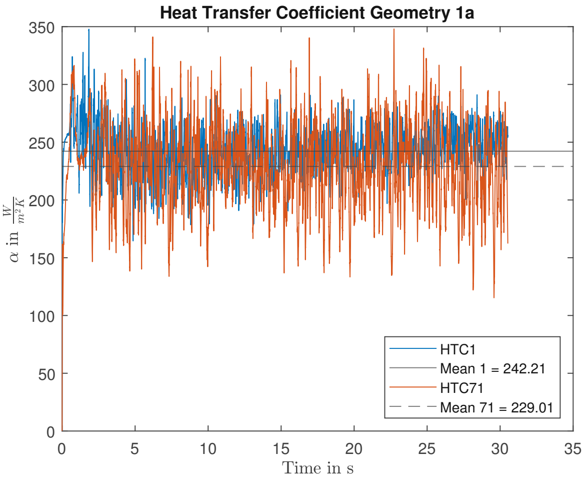

Figure 4.28: Geometry 1a double height HTC

In addition, the central tubes of the second and eighth level were heated in this simulation. Figure 4.27 and 4.28 show the graphical evaluation of the temperatures and determined heat transfer coefficients. For the tube with a higher heat transfer coefficient, a higher bubble frequency was calculated.

The same was done for a variant of geometry 1a with the triple number of pipe levels. Figure 4.29 again illustrates the decrease in bubble frequency with increasing height. However, compared to the double height variant, lower bubble frequencies were calculated for the lower pipe levels. Nevertheless, the decrease in bubble frequency with increasing height stagnates relatively quickly in the range of 2.4 to 2.7 $1/s$.

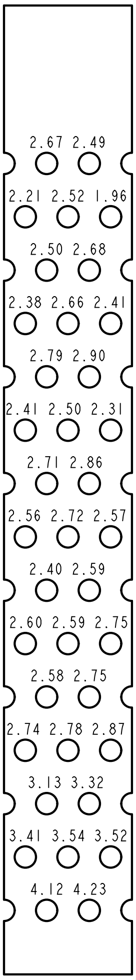

Figure 4.29: Geometry 1a triple height bubble frequency overview

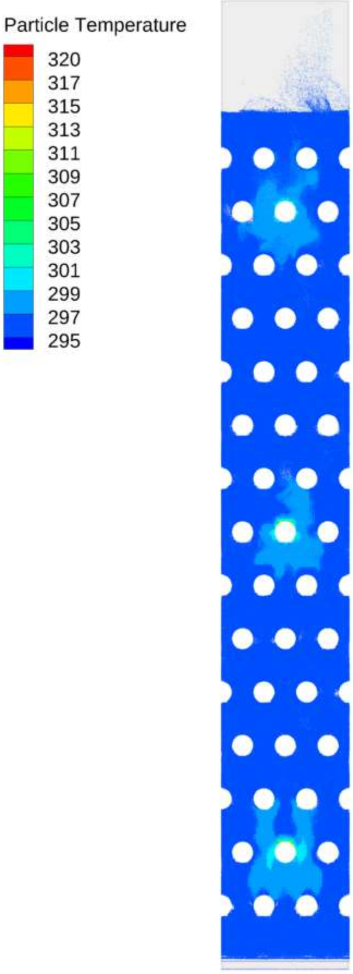

Figure 4.30: Geometry 1a triple height particle temperature distribution

In this simulation, three tubes were heated and the heat transfer coefficients were determined. Figure 4.30 shows that the particles only heat up locally around the heated tubes. Also the fluid temperature only heats up in the vicinity of the heated tubes. Thus, a falsification of the heat transfer determination for the two upper tubes can be excluded.

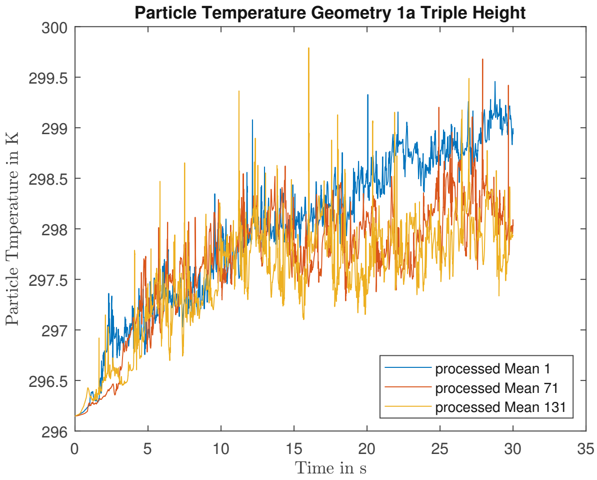

Figure 4.31: Geometry 1a triple height particle temperature

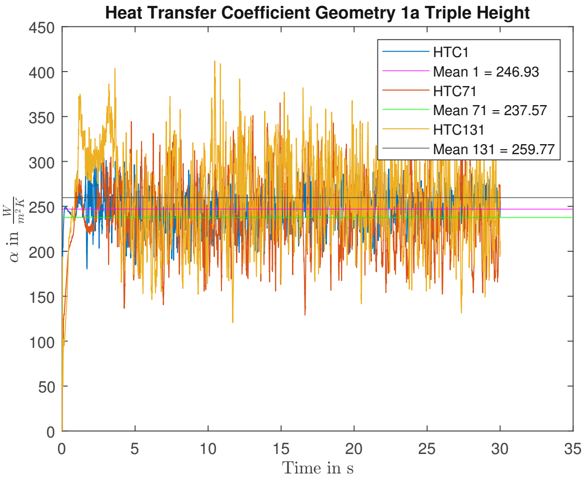

Figure 4.32: Geometry 1a triple height HTC

Again the evaluation of the lower two heated tubes showed a decrease in the heat transfer coefficient with increasing height. Contrary to expectations, however, the highest heat transfer coefficient was determined for the top tube, although the bubble frequency is lowest there. Nevertheless, the determined heat transfer coefficients are values with the same order of magnitude. With results of 250 ± 5 %, an approximately constant heat transfer over the height can be confirmed.

4.3.4 Flow conditions in the counter-current fluidized bed heat exchanger without auxiliary measures

In this section the results of the simulations of Geometry 2a and Geometry 2b are presented. Starting with Geometry 2a, fluxplanes were placed at the particle inlet, at the particle outlet and at three representative cross sections (CS), shown in Figure 4.33 (a). The cross sections are placed at $x = 0.1$ m (CS 1), at $x = 0.25$ m (CS 2) and at $x = 0.45$ m (CS 3). The fluidized bed chamber has a height of 0.565 m. To assess the quality of the directional particle flow and investigate whether there is a height dependence of the particle flow, the three flux planes were halved again. Thus, for each cross section there is one fluxplane that covers the entire cross section, one that goes from the floor to a height of 0.2825 m and one that goes from 0.2825 m to 0.565 m. Figure 4.33 (b) shows this for cross section 1 as an example.

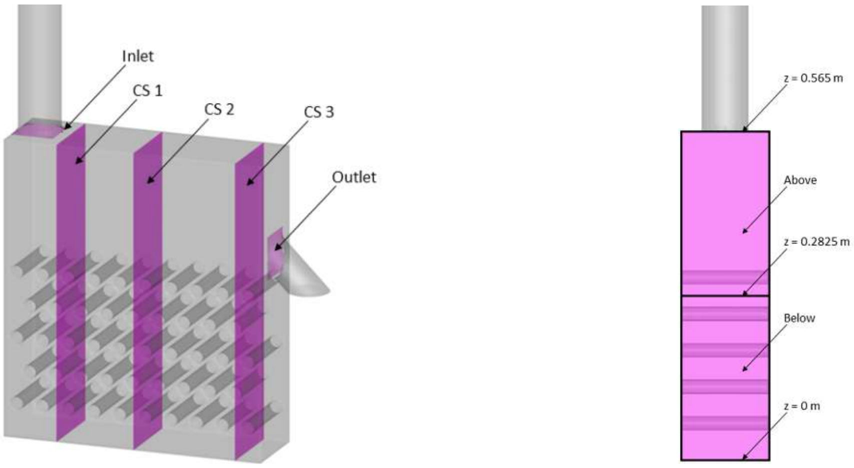

(a) Overview (b) Detail of CS 1

Figure 4.33: Fluxplanes of Geometry 2a

The evaluation of the over time integrated particle mass and the particle mass flow rate at the particle inlet and particle outlet are depicted in Figure 4.34 and 4.35. The small discontinuities of the particle mass flow rate at the inlet at 30 s, 30 s and 90 s result from the change of species, which was intended to visualise the mixing dynamics. Figure 4.35 shows the particle mass flow rate of 0.9 kg/s passing through the system. Related to the tube bundle cross section (150x(250+25+25) mm^2), this results in a mass flow density of 20 $\text{kg/m}^2\text{/s}$.

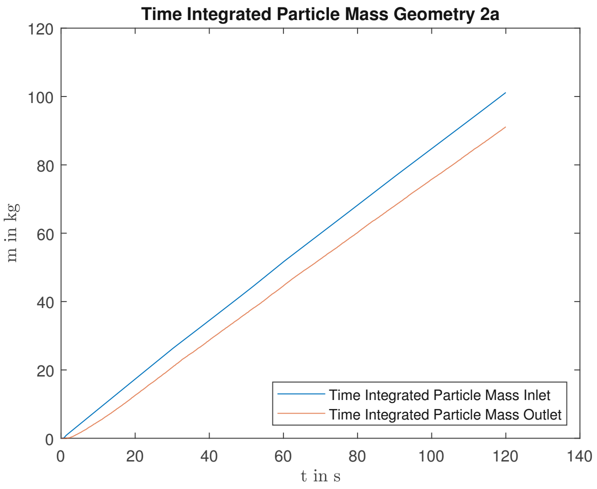

Figure 4.34: Geometry 2a particle mass

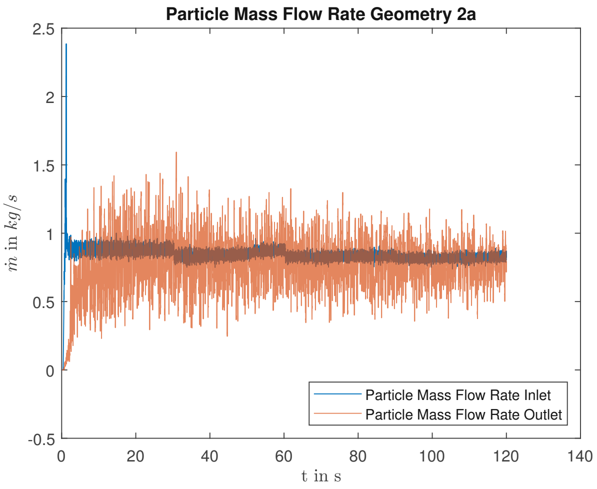

Figure 4.35: Geometry 2a particle mass flow

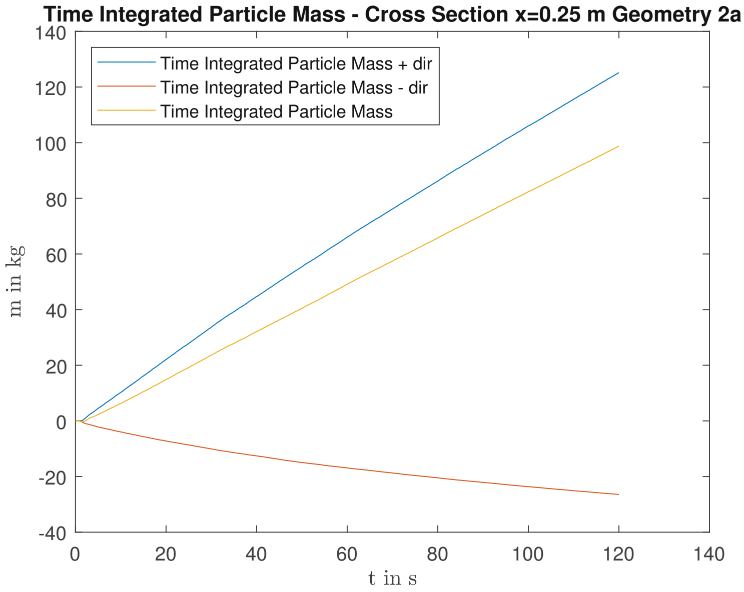

Figure 4.36: Geometry 2a particle mass, cross section 2

Figure 4.36 shows the evaluation of the flux plane at $x = 0.25$ m. A similar behaviour of the time integrated particle mass can be observed for the other two cross sections.

As already mentioned in Section 3.2.4, the particle mass integrated over time can be output depending on the passing direction of the particles. In Figure 4.36, the positive direction is in the direction of the particle outlet and the negative direction is to the left respectively in the direction of the particle inlet. The sum of the two signed curves gives the actual particle displacement. Accordingly, a directed particle flow in the desired direction could be identified.

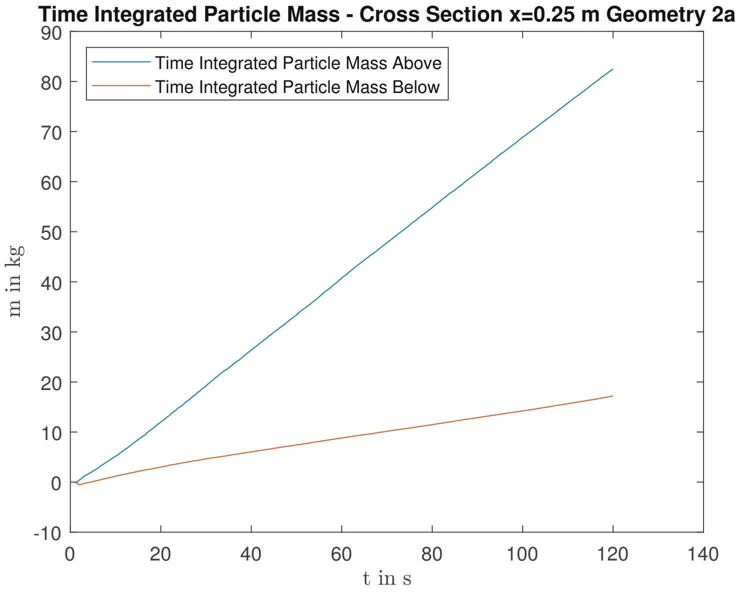

Figure 4.37: Geometry 2a particle mass, cross section 2 above/below

Figure 4.37 shows the evaluation of the flux planes already illustrated in Figure 4.33 (b). In all cross sections, a significantly higher mass flow in the upper half of the cross section could be identified. Considering that a large part of the upper half is not occupied by the fluidized bed but by the freeboard and that smaller particles tend to be located in this area, a significant bypass flow can thus be identified.

The simulation of Geometry 2b was carried out with the same boundary conditions as in the simulation of Geometry 2a. According to Figure 4.38 (a) flux planes were placed at the particle inlet, at the particle outlet, at $x = 0.25$ m (CS 1), at $x = 0.5$ m (CS 2) and at $x = 0.75$ m (CS 3). Figure 4.38 (b) again shows the halving of the flux planes for each cross section.

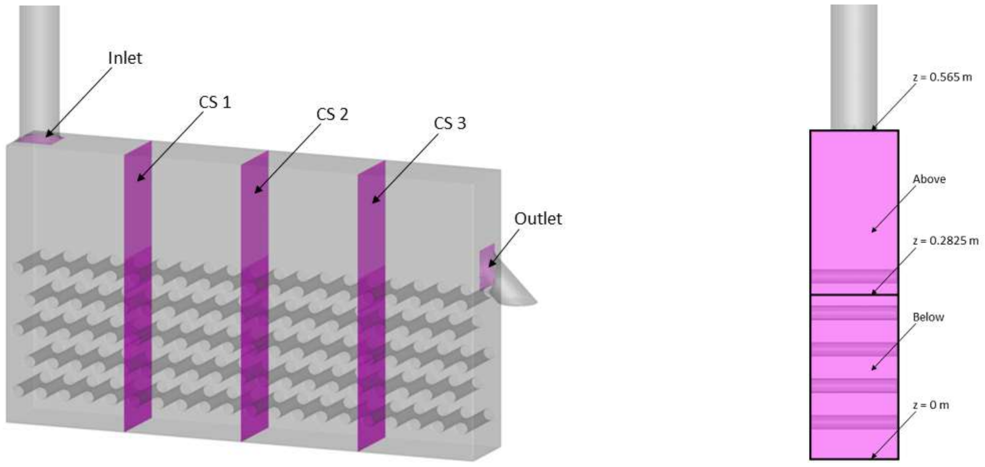

(a) Overview (b) Detail of CS 1

Figure 4.38: Fluxplanes of Geometry 2b

The evaluation of the flux planes of particle inlet and particle outlet, depicted in Figure 4.39 and 4.40, yielded similar results as that of Geometry 2a. Therefore, the mass flow density in relation to the tube bundle cross section is also 20 $\mathrm{kg/m^2/s}$. Only a longer time delay between particle inlet and particle outlet, due to the larger size, could be determined.

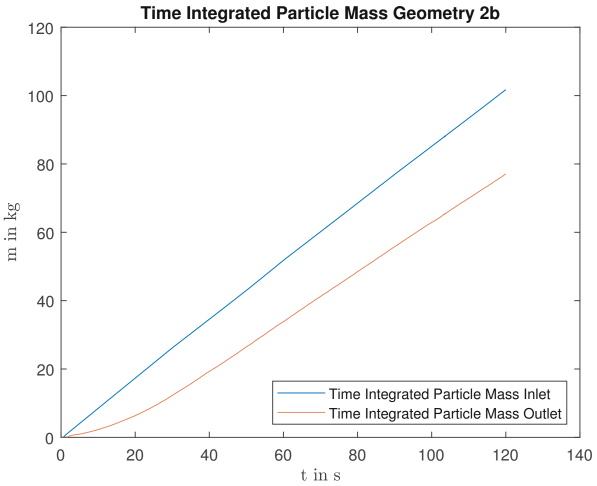

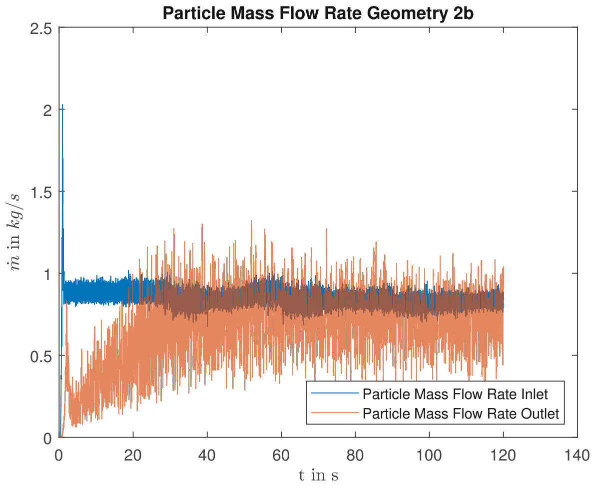

Figure 4.39: Geometry 2b particle mass

Figure 4.40: Geometry 2b particle mass flow

The evaluation of the particle mass integrated over time, depicted in Figure 4.41 showed almost identical results for all cross sections. Compared to Geometry 2a, a significantly higher proportion of backflow was observed.

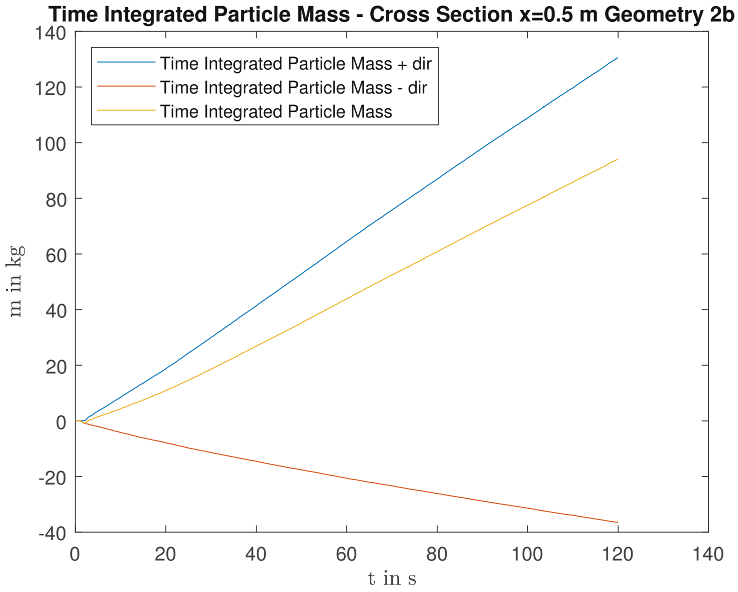

Figure 4.41: Geometry 2b particle mass, cross section 2

The separate evaluation of the particle mass integrated over time from the upper and lower flux planes are shown for two cross sections in Figure 4.42 and Figure 4.43. A similar behaviour of the time integrated particle mass of cross section 2 can be observed for cross section 3. All plots have in common that ultimately the particle flow dominates in the upper part of the chamber. As in Geometry 2a, this much higher mass flux in the upper part indicates the presence of unwanted bypass flows.

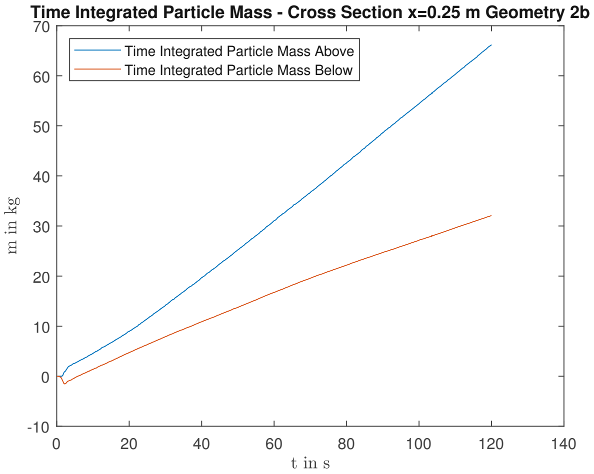

Figure 4.42: Geometry 2b particle mass, cross section 1 above/below

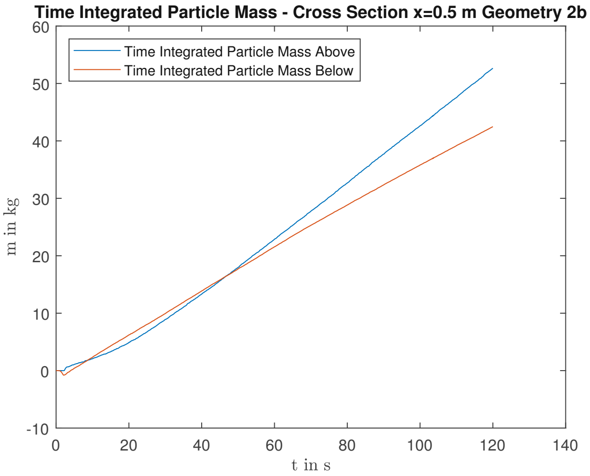

Figure 4.43: Geometry 2b particle mass, cross section 2 above/below

The particle mass flow bypasses the tube section in the small height zone above the tubes. In other words, the "real" mass flux density in the bundle is only in the order of10 kg/m^2/s. Such a performance is definitely not acceptable and in contradiction to the targeted plug flow. It has to be taken into account that the analyzed geometry with 5 vertical tube rows is not representative of a full scale heat exchanger with 20 to 50 vertical staggered tube rows. In full scale, the fluidized bed zones above and below the tube bundle will keep their height, while bundle height increases by a factor of 4 to 10. The cross section of potential bypass zones will in proportion be smaller. Hence it can be anticipated that also bypass percentage will strongly decrease.

The presence of bypass flows in the specific case was also clarified with the help of Tecplot. The Unique Particle ID was evaluated and used to create videos that animate the particle movements. These can be found under [21] for geometries 2a, 2b. Unfortunately, the particle path in the form of a streamline can not be visualised in Tecplot anymore. However, after contacting CPFD support, a feature request was made.

Figures 4.44 and 4.45 show the evaluation of the particle volume fraction of the respective geometries at the simulation time of 120 s. This shows the increasing bed height with increasing size.

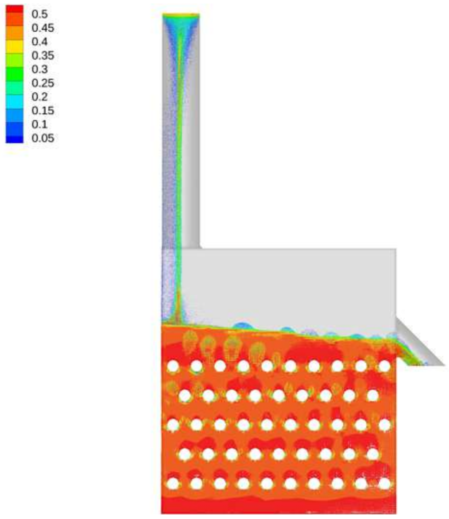

Figure 4.44: Particle volume fraction Geometry 2a

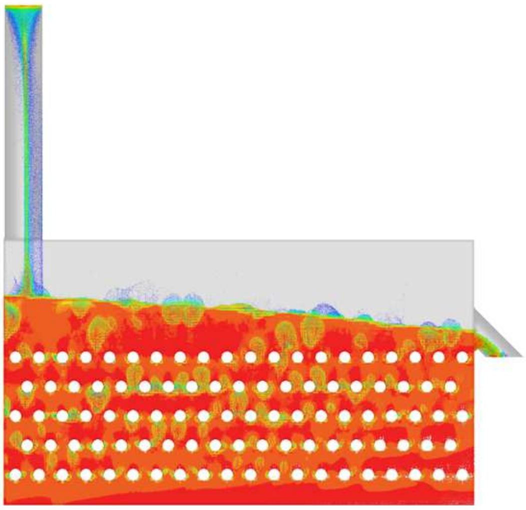

Figure 4.45: Particle volume fraction Geometry 2b

4.3.5 Flow conditions in the counter-current fluidized bed heat exchanger with auxiliary measures

In this section, the effect of an applied air-cushion technology on the flow behaviour of a counterflow fluidized bed heat exchanger is investigated. The heat exchanger is divided into four chambers by baffles. The baffles extend from the bottom to the first tube level and from the top into the fluidized bed. As Figure 4.46 shows, flux planes are used for the investigations at particle inlet and particle outlet as well as between the baffles and at three selected cross sections. The cross sections are placed at the same locations as in Geometry 2b in order to be able to make a direct comparison.

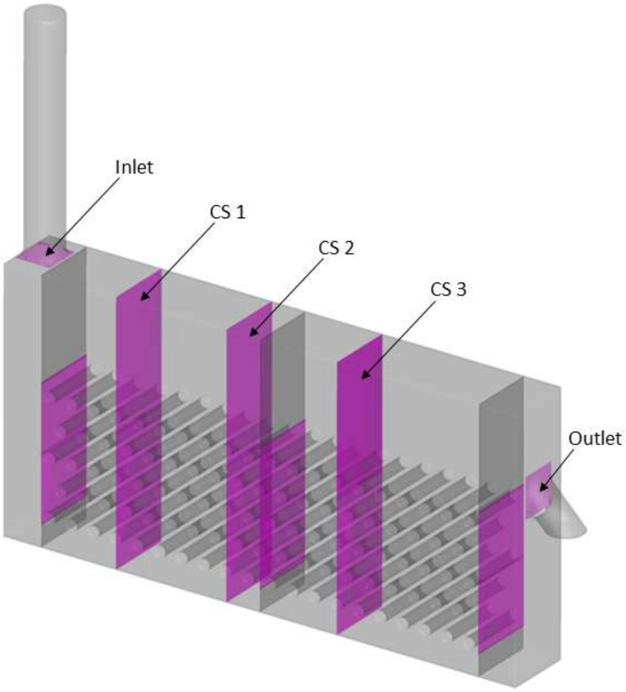

Figure 4.46: Flux planes Geometry 3

The air-cushions are used to achieve plug-flow like conditions through the tube bundle. This is to avoid unwanted bypass flows as they reduce system efficiency. In addition, bed height is to be reduced. Generally, a pressure difference between particle inlet and particle outlet is necessary for the sand to flow. In the simplest case, this is achieved by inclining the bed, as already shown in the previous Section. Air-cushions are pressure chambers that are used to avoid larger height differences and thus unused space.[31]

The choice of pressures per chamber is crucial for the performance of this technology. For the simulations carried out in this work, this is presented in Table 4.5.

Simulation	Chamber 1	Chamber 2	Chamber 3	Chamber 4
V1	100150	100125	100050	100000
V2	100000	100140	100050	100000
V3	100000	100500	100300	100000
V4	100000	100750	100400	100000

Table 4.5: Geometry 3 pressure distribution in Pascal

Apart from a slightly different bed height in chamber 1, no difference was found in the evaluation of simulation V1 and V2. Therefore, only the results of simulation V2 are presented below.

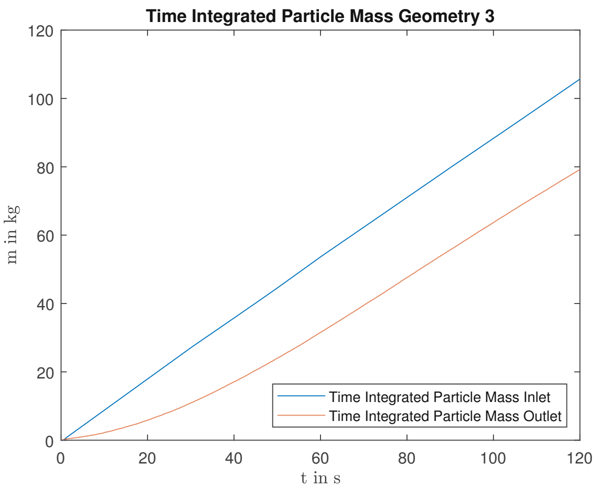

Figure 4.47: Geometry 3 particle mass

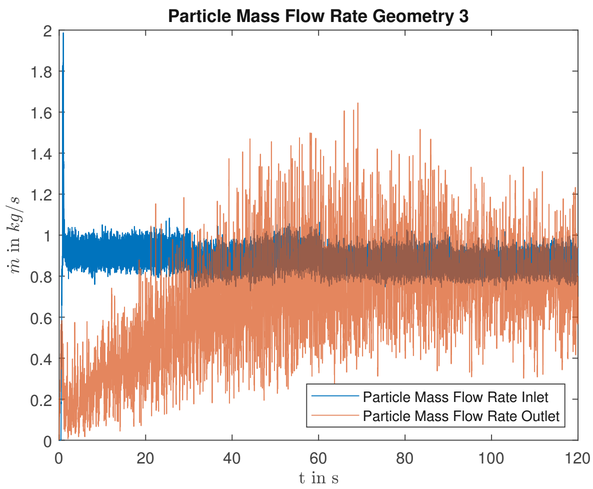

Figure 4.48: Geometry 3 particle mass flow

The evaluation of the particle inlet and particle outlet flux planes depicted in Figures 4.47 and 4.48 show similar behaviour to the analysis of Geometry 2b. Only the flow rate at the particle outlet shows a higher fluctuation range due to the baffles and the air cushion technology. Analogous to geometries 2a and 2b, the mass flow density in relation to the tube bundle cross section was set to 20 $kg/m^2/s$.

Again, only the evaluation of the central flux plane, depicted in Figure 4.49, is presented. The flux planes 1 and 3 show almost identical behaviour. Compared to Geometry 2b, no difference could be found. The relatively large backflow portion results from the characteristic flow patterns in the fluidized bed. Nevertheless, a flow directed in the particle outlet direction could be clearly identified.

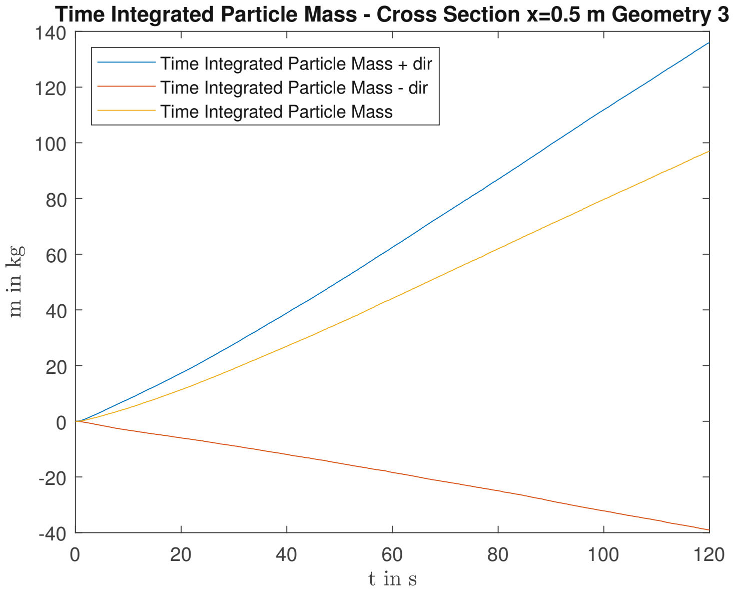

Figure 4.49: Geometry 3 particle mass, cross section 2

Figures 4.50 and 4.51 show the particle mass integrated over time that passes through the lower and upper parts of the cross sections 1 and 2. The cross section 3 shows almost identical behaviour. Compared to Geometry 2b, the majority of the particle mass does not pass through the upper part of the cross-section, but through the lower part. Thus, it can be proven that the use of baffles and air cushions significantly reduces the bypass flow. The majority of the particles flows through the tube bundle area and thereby participates in the heat exchange process.

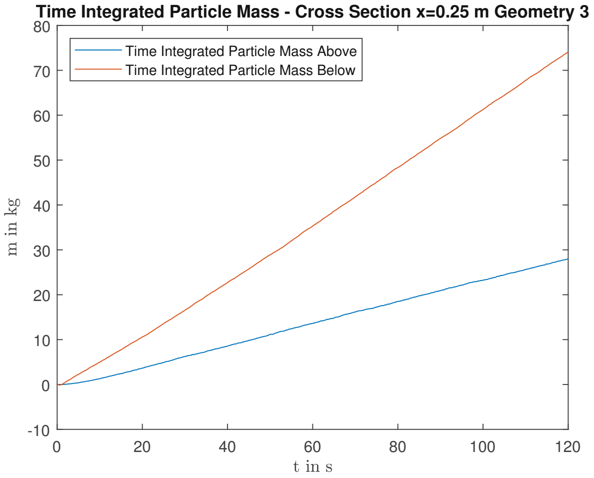

Figure 4.50: Geometry 3 particle mass, cross section 1 above/below

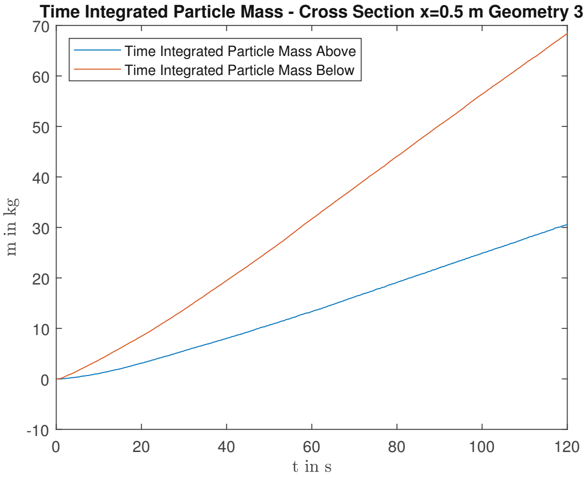

Figure 4.51: Geometry 3 particle mass, cross section 2 above/below

Figures 4.52 and 4.53 show the particle volume fraction of simulation V2 at two different times. In all simulations of Geometry 3, the bed height or bed inclination has levelled off after approximately 20 s.

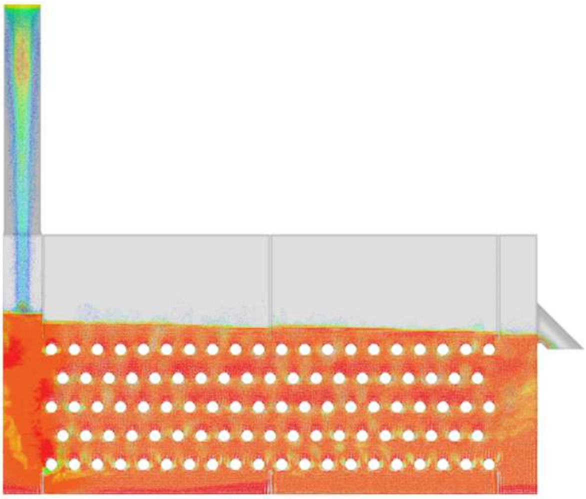

Figure 4.52: Particle volume fraction Geometry 3 V2 5 s

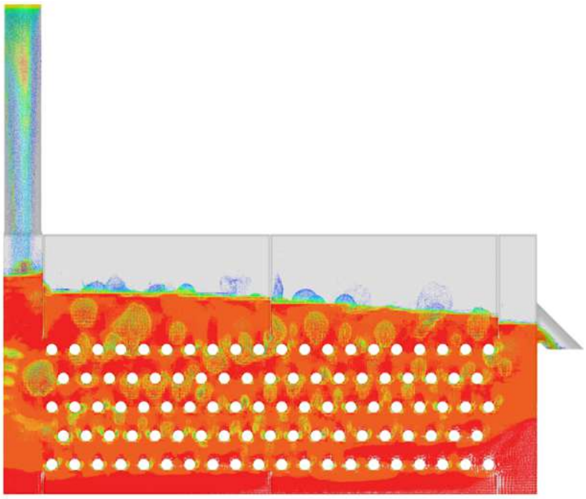

Figure 4.53: Particle volume fraction Geometry 3 V2 120 s

Since the bed heights of chamber 2 and chamber 3 can still be significantly reduced, simulation V3 was carried out with increased pressure.

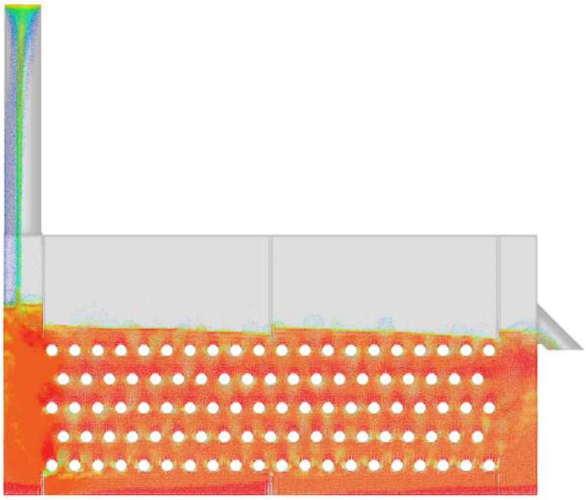

Figure 4.54: Particle volume fraction Geometry 3 V3 5 s

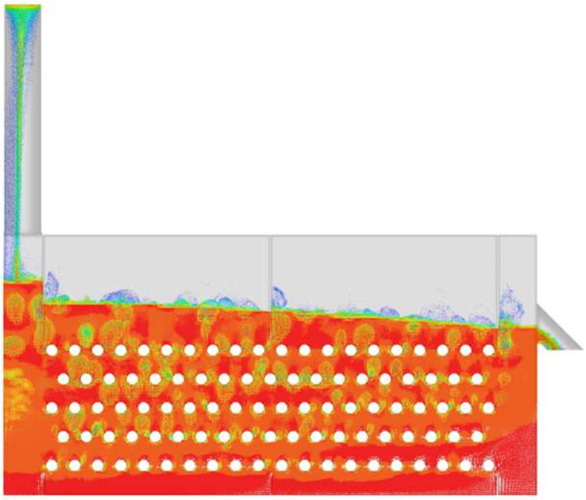

Figure 4.55: Particle volume fraction Geometry 3 V3 120 s

Figures 4.54 and 4.55 show that, with otherwise constant boundary conditions, the increased pressure results in a lower bed height. Especially the bed height of chamber 2 can still be reduced. Therefore simulation V4 was carried out with again increased pressures in the chambers. The results are shown in Figures 4.56 and 4.57. Compared to the previous simulation, the bed height could be reduced broadly and a permanent coverage of the pipe bundles could be ensured. The evaluation of the flux planes did not show significant differences compared to the already presented results of simulation V1.

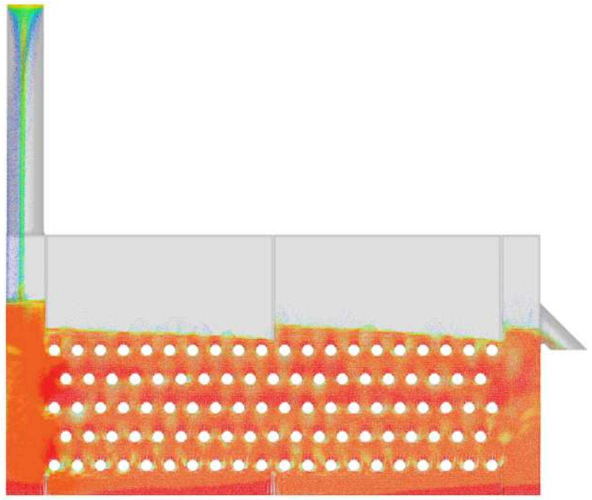

Figure 4.56: Particle volume fraction Geometry 3 V4 5 s

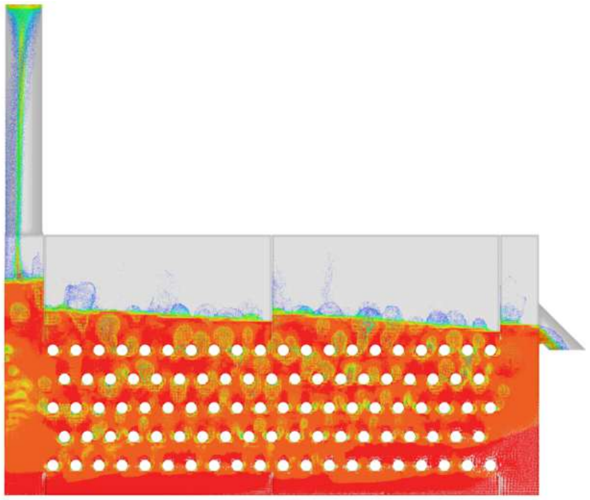

Figure 4.57: Particle volume fraction Geometry 3 V4 120 s

Figure 4.58 shows the particle dynamics visualised with the previously defined species. A static mass, which is located in the corners facing the flow, is recognisable in the figures.

Again, the Unique Particle ID was evaluated and used to create a video that animates the particle movement. This can be found under [21] for Geometry 3 and demonstrates the effectiveness of the air cushion technology.

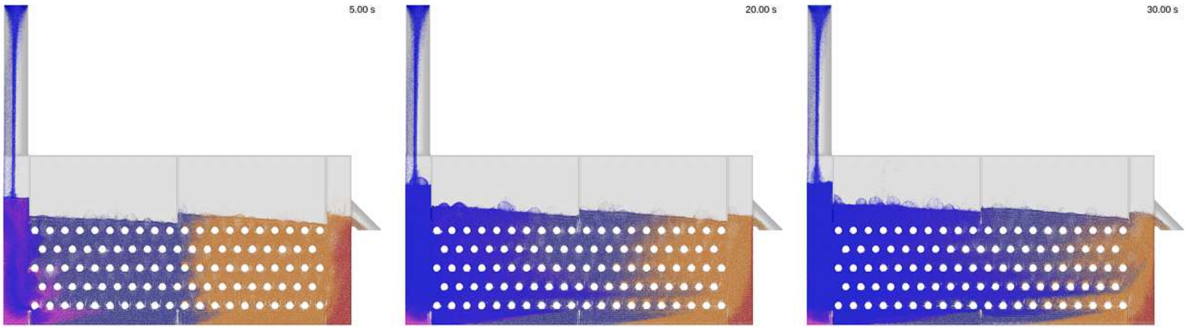

(a) 5 s (b) 20 s (c) 30 s

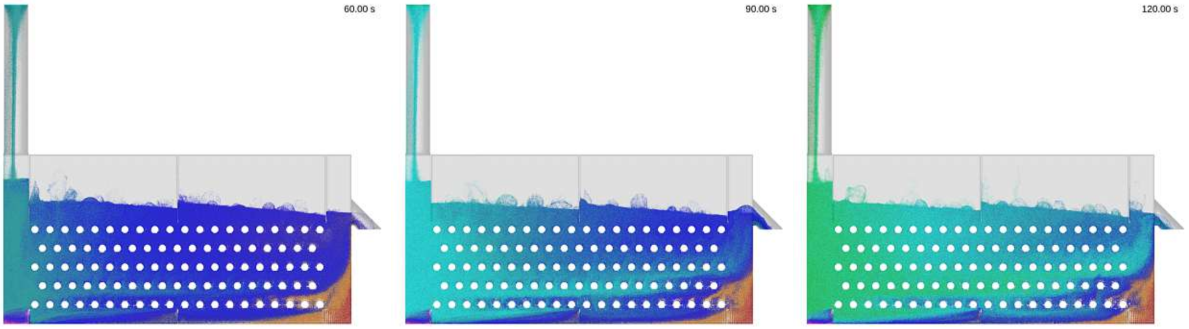

(d) 60 s (e) 90 s (f) 120 s

Figure 4.58: Geometry 3 species

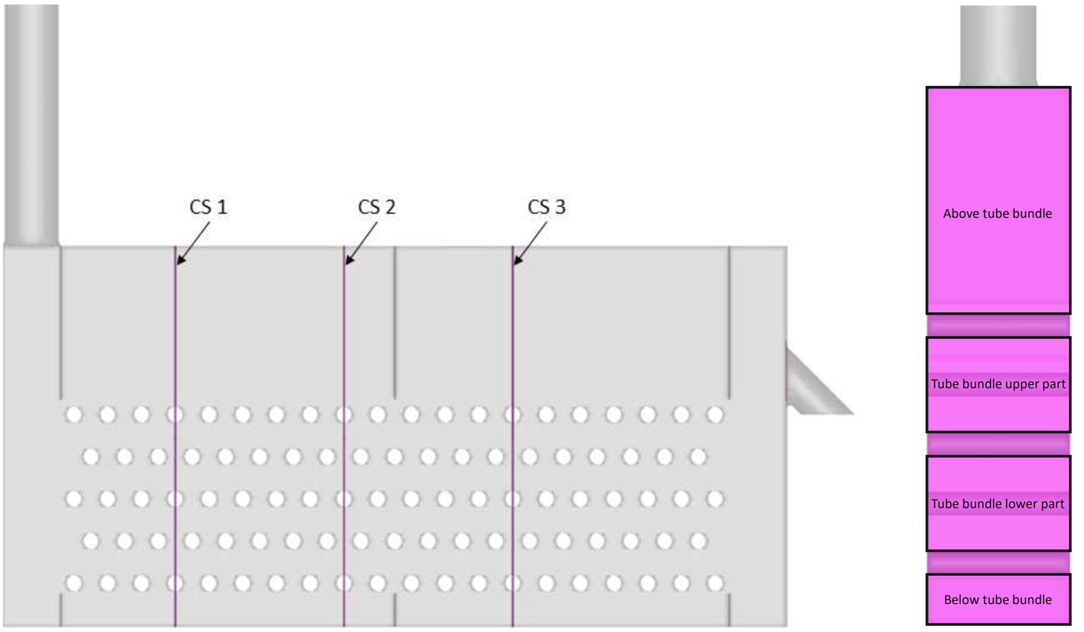

(a) Side view (b) Explanation

Figure 4.59: More detailed resolution of the flux planes, Geometry 3

Based on the results already mentioned, there was a need for a more precise resolution of the flux planes. This is to investigate the flow conditions inside and outside the tube bundle. Figure 4.59 (a) shows the three selected cross sections. Figure 4.59 (b) explains the additional subdivision of the flux planes per cross section.

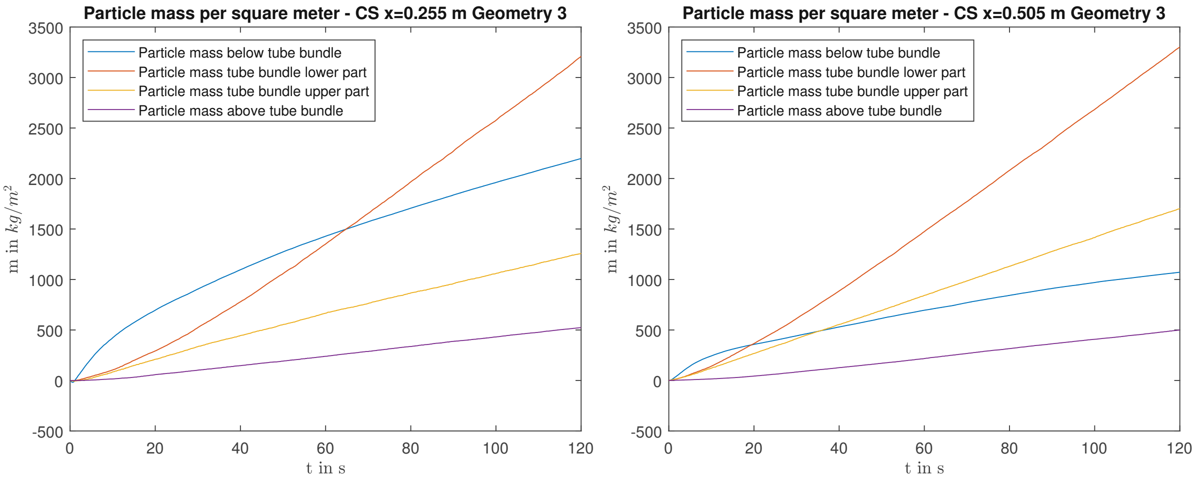

(a) Cross section 1

(b) Cross section 2

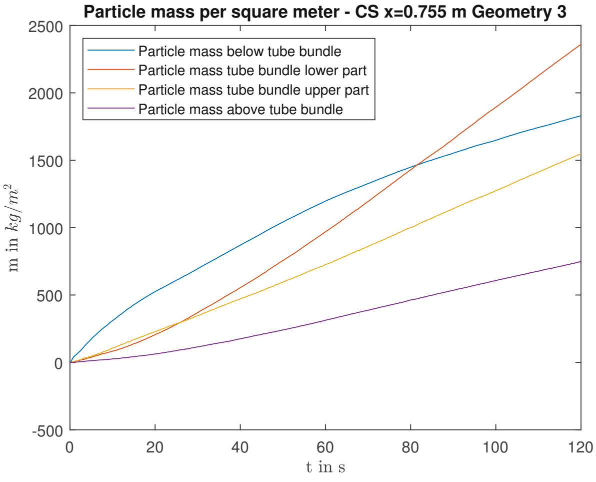

(c) Cross section 3

Figure 4.60: Particle mass per square meter, Geometry 3

The evaluation of the flux planes listed in Figure 4.59 with the pressure distribution V4 is shown in Figure 4.60 (a) - (c). Since the selected flux planes have different sizes, the curves of the particle masses integrated over time were scaled with the respective areas. The particle mass per square metre obtained in this way shows the lowest values in all cross sections above the tube bundles. The particle mass below the tube bundle varies greatly between the different cross sections. Interesting are by far the lowest values of cross section 2 near the middle baffle. This probably confirms the effectiveness of the baffles below the tube bundles. In addition, the particulate mass per square metre in the lower part of the tube bundles dominates in all cross sections.

Summing up, analysis of Geometry 3 showed that the bypass-issue which was detected in Geometry 2 could be effectively reduced and minimized. Nevertheless, the more detailed analysis grid in the bundle section revealed that strong mass flux density differences exist between the upper and the lower tube bundle tubes. It is therefore of high interest to perform further simulations with increased bundle height. The number of vertical tubes should be increased to the extent that still acceptable calculation times can be realized.

5 Conclusion

The last chapter of this diploma thesis includes a short summary of the main steps and results, a list of limitations in relation to the presented results and a proposal of future objectives.

5.1 Summary

After a brief explanation of the importance of energy storage systems and the potential of particle-based storage technologies, the basics of fluidization engineering were explained. As Barracuda® was used for the investigations, the main ideas behind this simulation program and the underlying equations were presented afterwards.

To eliminate ambiguities and to enable comparisons with other results, the minimum fluidization velocity was first determined simulatively. Significant deviations with available correlations were found. Then the heat transfer in the different variants of Geometry 1 was investigated. Initially, qualitative agreements with results already determined experimentally were calculated. The quantitative deviations were adjusted by modifying parameters of the heat transfer model in Barracuda®.

In general, an increased heat transfer with a lower vertical tube spacing could be observed. By using finned tubes, higher heat transfer coefficients could be calculated, with the helical fin showing lower values compared to the transversal fins. Of all the geometries, the lowest heat transfer coefficients were found for longitudinal fins.

A MATLAB code was created to determine the bubble frequency at the different tube types. By comparing the results of bubble frequency and heat transfer coefficient, an increasing heat transfer with increasing bubble frequency could be calculated in most cases. This illustrates the importance of the particle convective part in the heat transfer, but also shows that not all phenomena in fluidized beds can be completely explained with this.

Despite the built-in tube bundles that counteract coalescence, the bubble frequency decreases rapidly with increasing height. Although the bubble frequency decreases rapidly at first, it then develops more and more slowly towards a value different from 0.

The final investigation involved the effect of baffles and air cushion technology on the flow conditions in fluidized bed heat exchangers. For this purpose, significant bypass flows were first identified in the variant without built-in baffles. The simulation with built-in baffles and air cushion technology shows a significant reduction of these unwanted flow conditions and a realisation of plug-flow like behaviour. In addition, the sensitivity of the bed height to changes in the chamber pressures was demonstrated by several simulations with different pressure distributions.

5.2 Limitations

First of all, it should be said that information is always lost through the simulative modeling of a real plant. In the end, it is a simplified representation of reality. In the specific case of fluidized bed technology, where a universally valid set of formulas for describing the flow and heat transfer phenomena is still outstanding, certain limitations are associated with the statements made.

The description of the heat transfer and flow behaviour in Barracuda® is done with correlations that are valid for a small range of applications. This topic has already been discussed in detail for heat transfer. For the description of the flow behaviour, several drag models can be selected in Barracuda®. In this thesis, for example, the drag model of Wen and Yu [37] was used, which is more applicable for dilute systems. The effects of using Ergun's model [8], which is suitable for higher packing fractions, would be interesting. In addition, the effect of changing the default settings of the particle-to-particle interaction and particle-to-wall interaction was not investigated in this work.

In this thesis, the fin efficiencies were completely neglected in the heat transfer determination of the different tube types. By specifying a constant surface temperature, heat conduction phenomena within the pipe wall were not taken into account. A negative effect on the real system behaviour is conceivable, although the heat conduction properties of the pipe material are good and the wall thicknesses are relatively small. This is countered by the temperature effect. All simulations have been carried out at relatively low temperature levels. A positive effect on heat transfer due to increased gas thermal conductivity and increased radiant heat transfer at the targeted operating temperatures is expected.

Another limitation concerns the determination of the bubble frequency. Due to the point property of the observation point, not every bubble can be detected correctly. Since bubbles are not completely solid-free and the bubbles do not always pass the centre of the transient data point, information about bubble size and bubble velocity can be lost. Nevertheless, the raw data for determining the bubble frequency were recorded consistently at the same point as the temperature for determining the heat transfer. Thus, at least comparisons of the results within this work are valid.

5.3 Future objectives

In general, there is still substantial research potential in fluidization engineering. Since a diploma thesis would definitely not be sufficient to cover all of this, possible future objectives in the vicinity of the topics dealt with in this thesis will be listed here.

- Using Ergun's drag model [8]
- Different correlation of the dense phase heat transfer model
- Simulations with higher temperature levels and under use of radiation models to determine the temperature effect
- Visualization of the particle path with the developed feature from Tecplot
- Variation of particle mass flows in the fluidized bed heat exchanger and the effect of pressure control
- Simulation of Geometry 2b and 3 with increased bundle height and bundle length (An ideal dimension would be 20 tubes rows vertical and 40 tube rows horizontal, at a theoretical bundle mass flux density of 20 $kg/m^2/s$. It has to be determined what is the maximum feasible bed dimension, in terms of number of cells and in terms of calculation time.)

Bibliography

[1] CPFD Software Version 17.3.1. Barracuda virtual reactor user manual. Accessed: 2022-03-17.

[2] Spiros Alexopoulos and Soteris A Kalogirou. *Solar Thermal Energy*. Springer US Imprint: Springer, New York, NY, 1st ed. 2022. edition, 2022.

[3] M.J. Andrews and P.J. O'Rourke. The multiphase particle-in-cell (mp-pic) method for dense particulate flows. *International Journal of Multiphase Flow*, 22(2):379–402, 1996.

[4] S. P. Babu, B. Shah, and A. Talwalkar. Fluidization correlations for coal gasification materials — minimum fluidization velocity and fluidized bed expansion ratio. *Chem. Eng. Prog. Symp. Ser.*, 74(176):176–186, 1978.

[5] A.K. Biń. Prediction of the minimum fluidization velocity. *Powder Technology*, 81(2):197–199, 1994.

[6] P. Bourgeis and P. Grenier. Ratio of terminal velocity to minimum fluidization velocity for spherical particles. *Can. J. Chem. Eng.*, 46(1968).

[7] John C. Chen, John R. Grace, and Mohammad R. Golriz. Heat transfer in fluidized beds: design methods. *Powder Technology*, 150(2):123–132, 2005. Scale-Up in Particle Processing.

[8] Sabri Ergun. Fluid flow through packed columns. *Chemical Engineering Progress*, 48:89–94, 1949.

[9] Liang-Shih Fan and Chao Zhu. *Principles of gas-solid flows*. Cambridge series in chemical engineering. Cambridge University Press, Cambridge, 1998.

[10] D. Geldart. Types of gas fluidization. *Powder Technology*, 7(5):285–292, 1973.

[11] John R. Grace. *Hydrodynamics of Bubbling Fluidization*, chapter 7, pages 131–152. John Wiley & Sons, Ltd, 2020.

[12] S. F. Harris and D. G. Crighton. Solutions, solitary waves, and voidage disturbances in gas-fluidized beds. *Journal of fluid mechanics*, 266:243–276, 1994.

[13] Florian Heindl. Numerische Untersuchung von Strömung und Wärmeübergang in Fließbett-Wärmetauschern. Diplomarbeit, Technische Universität Wien, 2019.

[14] John E. Hesselgreaves, Richard Law, and David A. Reay. *Chapter 7 - Thermal Design*. Butterworth-Heinemann, second edition edition, 2017.

[15] Hermann Hofbauer. *Unterlagen zur Vorlesung Wirbelschichttechnik*. TU Wien, 4 edition, 2019.

[16] Dening Eric Jia. *Heat and Mass Transfer*, chapter 14, pages 291–331. John Wiley & Sons, Ltd, 2020.

[17] Sung Won Kim, Jung Yeul Ahn, Sang Done Kim, and Dong Hyun Lee. Heat transfer and bubble characteristics in a fluidized bed with immersed horizontal tube bundle. *International Journal of Heat and Mass Transfer*, 46(3):399–409, 2003.

[18] Daizo Kunii and Octave Levenspiel. *Fluidization engineering*. Butterworth-Heinemann series in chemical engineering. Butterworth-Heinemann, Boston [u.a.], 2. ed.. edition, 1991.

[19] VK Maskaev and AP Baskakov. Characteristics of external heat transfer in a fluidization bed of coarse particles. *Journal of engineering physics*, 24(4):411–414, 1973.

[20] Mohammadhadi Nakhaei, Christian Evald Hessel, Hao Wu, Damien Grévain, Sam Zakrzewski, Lars Skaarup Jensen, Peter Glarborg, and Kim Dam-Johansen. Experimental and cpfd study of gas–solid flow in a cold pilot calciner. *Powder Technology*, 340:99–115, 2018.

[21] Ladner Noah. NUMERICAL ANALYSIS OF FLOW STRUCTURE AND HEAT TRANSFER IN BUBBLING FLUIDIZED BEDS. `https://doi.org/10.5281/zenodo.6619781`, June 2022.

[22] Peter J. O'Rourke and Dale M. Snider. A new blended acceleration model for the particle contact forces induced by an interstitial fluid in dense particle/fluid flows. *Powder Technology*, 256:39–51, 2014.

[23] J.F. Richardson and M.A. da S. Jerónimo. Velocity-voidage relations for sedimentation and fluidisation. *Chemical Engineering Science*, 34(12):1419–1422, 1979.

[24] S.C. Saxena. Heat transfer between immersed surfaces and gas-fluidized beds. volume 19 of *Advances in Heat Transfer*, pages 97–190. Elsevier, 1989.

[25] Dietmar Schulze. *Pulver und Schüttgüter - Fließeigenschaften und Handhabung*. Springer-Verlag, Berlin Heidelberg New York, 2019.

[26] J. SMAGORINSKY. General circulation experiments with the primitive equations: I. the basic experiment. *Monthly Weather Review*, 91(3):99 – 164, 1963.

[27] Dale M. Snider, Samuel M. Clark, and Peter J. O'Rourke. Eulerian–lagrangian method for three-dimensional thermal reacting flow with application to coal gasifiers. *Chemical Engineering Science*, 66(6):1285–1295, 2011.

[28] D.M. Snider. An incompressible three-dimensional multiphase particle-in-cell model for dense particle flows. *Journal of Computational Physics*, 170(2):523–549, 2001.

[29] Christopher B. Solnordal, Venkatakrishna Kenche, Trevor D. Hadley, Yuqing Feng, Peter J. Witt, and K-Seng Lim. Simulation of an internally circulating fluidized bed using a multiphase particle-in-cell method. *Powder Technology*, 274:123–134, 2015.

[30] Jacqueline A Stagner and David S-K Ting. *Renewable energy for mitigating climate change*. CRC Press, Boca Raton, FL, first edition. edition, 2022.

[31] Peter Steiner, Karl Schwaiger, Heimo Walter, and Markus Haider. Active fluidized bed technology used for thermal energy storage. In *Energy Sustainability*, volume 50220. American Society of Mechanical Engineers, 2016.

[32] Peter Stephan, Stephan Kabelac, Matthias Kind, Dieter Mewes, Karlheinz Schaber, and Thomas Wetzel. *VDI-Wärmeatlas - Fachlicher Träger VDI-Gesellschaft Verfahrenstechnik und Chemieingenieurwesen*. Springer-Verlag, Berlin Heidelberg New York, 12 edition, 2019.

[33] Stefan Thanheiser, Markus Haider, and Paul Schwarzmayr. Experimental investigation of the heat transfer between finned tubes and a bubbling fluidized bed with horizontal sand mass flow. *Energies*, 15(4), 2022.

[34] H.A. Vreedenberg. Heat transfer between a fluidized bed and a horizontal tube. *Chemical Engineering Science*, 9(1):52–60, 1958.

[35] Hakon Wadell. Volume, shape, and roundness of rock particles. *The Journal of Geology*, 40(5):443–451, 1932.

[36] C.Y. Wen and Y.H. Yu. A generalized method for predicting the minimum fluidization velocity. *A.I.Ch.E. Journal*, 12(3):610–612, 1966.

[37] C.Y. Wen and Y.H. Yu. Mechanics of fluidization. In *Chem. Eng. Prog. Symp. Ser.*, volume 62, pages 100–111, 1966.

[38] Kevin J. Whitty and Michael Siddoway. A system for measuring bubble voidage and frequency around tubes immersed in a fluidized bed of particles. *Review of Scientific Instruments*, 81(7):073305, 2010.

[39] Shiliang Yang, Xiaohuan Liu, and Shuai Wang. Cfd simulation of air-blown coal gasification in a fluidized bed reactor with continuous feedstock. *Energy Conversion and Management*, 213:112774, 2020.

[40] Wen-Ching Yang. *Handbook of fluidization and fluid-particle systems*. Chemical industries. Dekker, CRC Press, New York, NY [u.a.], 2003.

[41] Sergei Zabrodski. *Hydrodynamics and heat transfer in fluidized beds*. MIT Press (MA), 1966.

[42] Yongmin Zhang and Qing Wei. Cpfd simulation of bed-to-wall heat transfer in a gas-solids bubbling fluidized bed with an immersed vertical tube. *Chemical Engineering and Processing: Process Intensification*, 116:17–28, 2017.

List of Figures

List of Tables

A | Data Sheets

This appendix contains all relevant data sheets.

BCS215

BAUCHEMIESANDE | CONSTRUCTION CHEMICALS SANDS

Chemische Analyse | Chemical analysis

Fe_2O_3	< 0,2 %
Al_2O_3	< 0,2 %
TiO_2	< 0,2 %
SiO_2	> 99,1 %

Physikalische Kenndaten | Physical characteristics

Mittlere Körnung | Medium grain size	0,146 mm
AFS Kennzahl | AFS number	91
Theoretische spezifische Oberfläche | Theoretic specific surface area	165 cm^2/g
Gleichmäßigkeitsgrad | Uniformity ratio	75 %
Glühverlust | Loss on ignition	< 0,2 %
Sinterbeginn | Sintering point	> 1550 °C
Schüttdichte feuergetrocknet | Bulk density fire dried	1,34 to/m^3

Korngrößenverteilung | Grain size distribution

Maschenweite | Mesh Size (mm)	Rückstand | Residue (%)	Summe | Sum (%)	Toleranzbereich | Tolerance range (%)
> 0,710	0,0		
0,500–0,710	0,0		
0,355–0,500	0,0		
0,250–0,355	0,5	100,0	0–1
0,180–0,250	18,0	99,5	12–24
0,125–0,180	50,0	81,5	45–55
0,090–0,125	27,0	31,5	22–32
0,063–0,090	4,0	4,5	3–6
0,000–0,063	0,5	0,5	0–1

Die angegebenen Daten stellen Jahresdurchschnittswerte dar, eine Verbindlichkeit kann daraus nicht abgeleitet werden.

The shown data represent annual averages, a liability can not be deduced.

STROBEL QUARZSAND GmbH | Freihungsand | 92271 Freihung | Germany | www.strobel-quarzsand.de | info@strobel-quarzsand.de | T: 09646 92010 | F: 09646 1257
STAND 10/2016 | REVISION 10

B | MATLAB Code

This appendix contains the programmed MATLAB code for the data analysis of Geometry 1a as an example. All relevant functions for the evaluation of the remaining geometries can also be found in it.

Code Listing B.1: Code of Evaluation Geometry 1a

```
%%  Auswertung Geometrie 1a                            %%
%   Author: Noah Ladner                                %%
%%%%%%%%%%%%%%%%%%%%%%%%%%%%%%%%%%%%%%%%%%%%%%%%%%%%%%%%%

clearvars
clc
close all


%Laden der Daten
data = read_data('trans.data00');  % Volume Fraction, Particle Temperature
data1 = read_data('trans.data01'); % Heat Transfer


figure % Particle Temperatur
plot(data(:,1),data(:,14))
hold on
plot(data(:,1),data(:,15))
plot(data(:,1),data(:,16))
plot(data(:,1),data(:,17))
T_Sand = (data_process(data(:,14))+data_process(data(:,15))+data_process(data(:,16))+data_process(data(:,17)))/4; % bereinigte mittlere Sandtemperatur in K
plot(data(:,1),T_Sand)
title('Particle Temperature Geometry 1a');
xlabel('Time in s', 'interpreter','latex')
ylabel('Particle Tmperature in K', 'interpreter','latex')
legend('top', 'right', 'bottom', 'left', 'processed Mean ', 'Location','southeast')

% Total wall heat transfer rate in W
figure
plot(data1(:,1),data1(:,2));
Q_mitt = data_mitt(data1, 2);
Mitt1_str = sprintf('Mean  = %.2f', Q_mitt);
p2 = yline(Q_mitt);
legend(p2,{Mitt1_str})
title('Heat Transfer Rate Geometry 1a');
xlabel('Time in s', 'interpreter','latex')
ylabel('$\dot{Q}$ in $W$', 'interpreter','latex')

% Waermeuebergangskoeffizient
figure
A_Rohr = ones(size(data(:,14)))*0.01179888; % Rohroberflaeche
T_Rohr = ones(size(data(:,14)))*498; % Rohrtemperatur in K
Q = data1(:,2); % Total wall heat transfer rate in W
alpha = Q./(A_Rohr.*(T_Rohr-T_Sand));
p1 = plot(data(:,1),alpha);
hold on
t_alpha = [data(:,1) alpha]; %Matrix fuer Mittelwertbildung mit Zeitvektor
alpha_mitt = data_mitt(t_alpha, 2);
Mitt1_str = sprintf('Mean  = %.2f', alpha_mitt);
p2 = yline(alpha_mitt);
```

```
legend(p2,{Mitt1_str})
title('Heat Transfer Coefficient Geometry 1a');
xlabel('Time in s', 'interpreter','latex')
ylabel('$\alpha$ in $\frac{W}{m^2 K}$', 'interpreter','latex')

alpha_a=[data(:,1),alpha, ones(size(data(:,1)))*alpha_mitt];
save('alpha_a.mat','alpha_a');

figure % Blasenfrequenz mit Particle Volume Fraction Rohr 1 30s
[t_Minima_r,Minima_r,n_r]=find_minima(data(1:end,1), data(1:end,3)); % Particle Volume Fraction Minima rechts
[t_Minima_l,Minima_l,n_l]=find_minima(data(1:end,1), data(1:end,5)); % Particle Volume Fraction Minima links
f_b_1=(n_r+n_l)/(2*data(end,1)) %Halbe Blasenfrequenz Rohr 1
plot(data(1:end,1), data(1:end,3),t_Minima_r,Minima_r,'r*')
hold on
plot(data(1:end,1),data(1:end,5),t_Minima_l,Minima_l,'g*')
title('Particle Volume Fraction Geometry 1a Tube 1');
xlabel('Time in s', 'interpreter','latex')
ylabel('Particle Volume Fraction in 1', 'interpreter','latex')
n_r_str = sprintf('n_r = %d', n_r);
n_l_str = sprintf('n_l = %d', n_l);
legend('Part.Vol.Frac right', n_r_str , 'Part.Vol.Frac left',n_l_str)

% Blasenfrequenz mit Particle Volume Fraction Rohr 2 30s
[t_Minima_r,Minima_r,n_r]=find_minima(data(1:end,1), data(1:end,7)); % Particle Volume Fraction Minima rechts
[t_Minima_l,Minima_l,n_l]=find_minima(data(1:end,1), data(1:end,9)); % Particle Volume Fraction Minima links
f_b_2=(n_r+n_l)/(2*data(end,1)) %Halbe Blasenfrequenz Rohr 2

% Blasenfrequenz mit Particle Volume Fraction Rohr 2 30s
[t_Minima_r,Minima_r,n_r]=find_minima(data(1:end,1), data(1:end,11)); % Particle Volume Fraction Minima rechts
[t_Minima_l,Minima_l,n_l]=find_minima(data(1:end,1), data(1:end,13)); % Particle Volume Fraction Minima links
f_b_3=(n_r+n_l)/(2*data(end,1)) %Halbe Blasenfrequenz Rohr 3

function data = read_data(filename)
%Funktion  ffnet  trans.data00 (29 Spalten) und konvertiert in Matrix
fileID = fopen(filename); %open file
C = textscan(fileID, '%f %f %f %f %f %f %f %f %f %f %f %f %f %f %f %f %f %f %f %f %f %f %f %f %f %f %f %f %f', 'CommentStyle', '#'); %Read formatted data from text file or string
fclose(fileID); %close file

data = cell2mat(C);
end

function mitt = data_mitt(data, s) %uebergabe von Matrix, Spaltennummer
%Mittelwert fuer variable Zeitschritte
zs=size(data);
sum = data(1,s);

    for i = 2:zs(1)
        sum = sum + data(i,s)*(data(i,1)-data(i-1,1));
    end
mitt = (1/(data(end,1)-data(1,1)))*sum;

end

function [t_Minima,Minima,Anzahl] = find_minima(t, A)
% Funktion findet Minimalwerte fuer Blasenfrequenz: aus Zeitvektor und
% Datenvektor wird Zeitvektor der Minimalwerte, Datenwerte der Minima und
% Anzahl der Minima
TF = islocalmin(A,'MinSeparation',0.07,'SamplePoints',t);
Minima = A(TF);
t_Minima = t(TF);
n=length(Minima);
for i=1:length(Minima)
    if Minima(i)>0.2 % lokale Minima die gr   er als 0.2 sind werden nicht gewertet
        n=n-1;
        Minima(i)=[NaN];
        t_Minima(i)=[NaN];
    else
        continue
    end
end

Anzahl = n;
end

```

```
function vec_pr = data_process(vec)
%Funktion ersetzt 0-Werte des Vektors mit dem vorherigen Wert
vec_pr=vec;
for i=1:length(vec)
    if vec(i)==0
        vec_pr(i)=vec_pr(i-1);
    else
        continue
    end
end
end
```

C Technical Drawings

This appendix contains the technically drawings of the examined geometries.

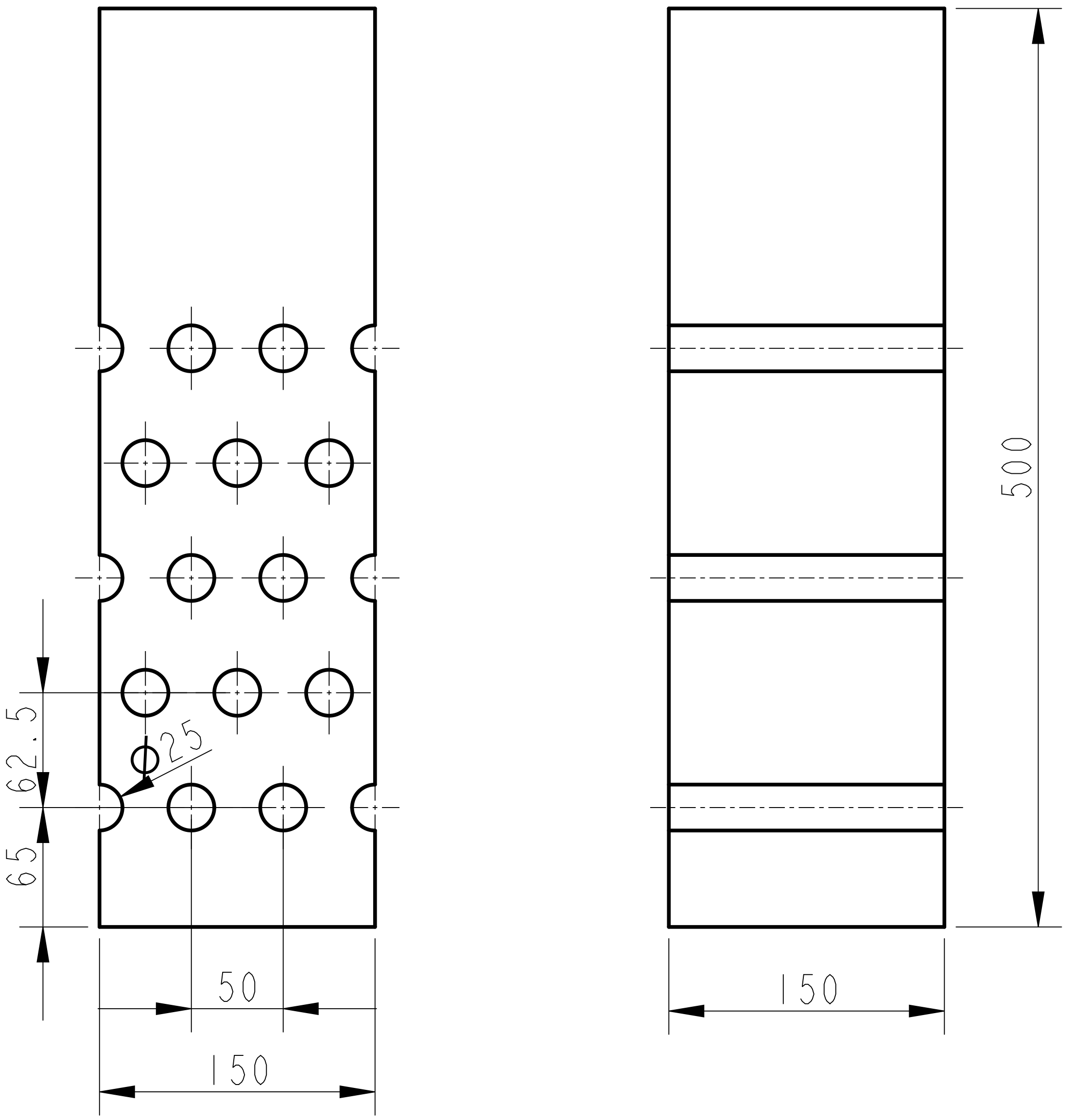

horizontal pitch: 50 mm
vertical pitch: 62.5 mm
tube: ⌀ 25 mm

Allgemeintoleranz:	Institut für Energietechnik und Thermodynamik	TU Wien
-	Benennung: Geometrie 1a	Name: Noah Ladner
Maßstab: 1 : 4		Studienjahr: 2022
	Zeichnungsnummer: 1	Datum: Apr-16-22

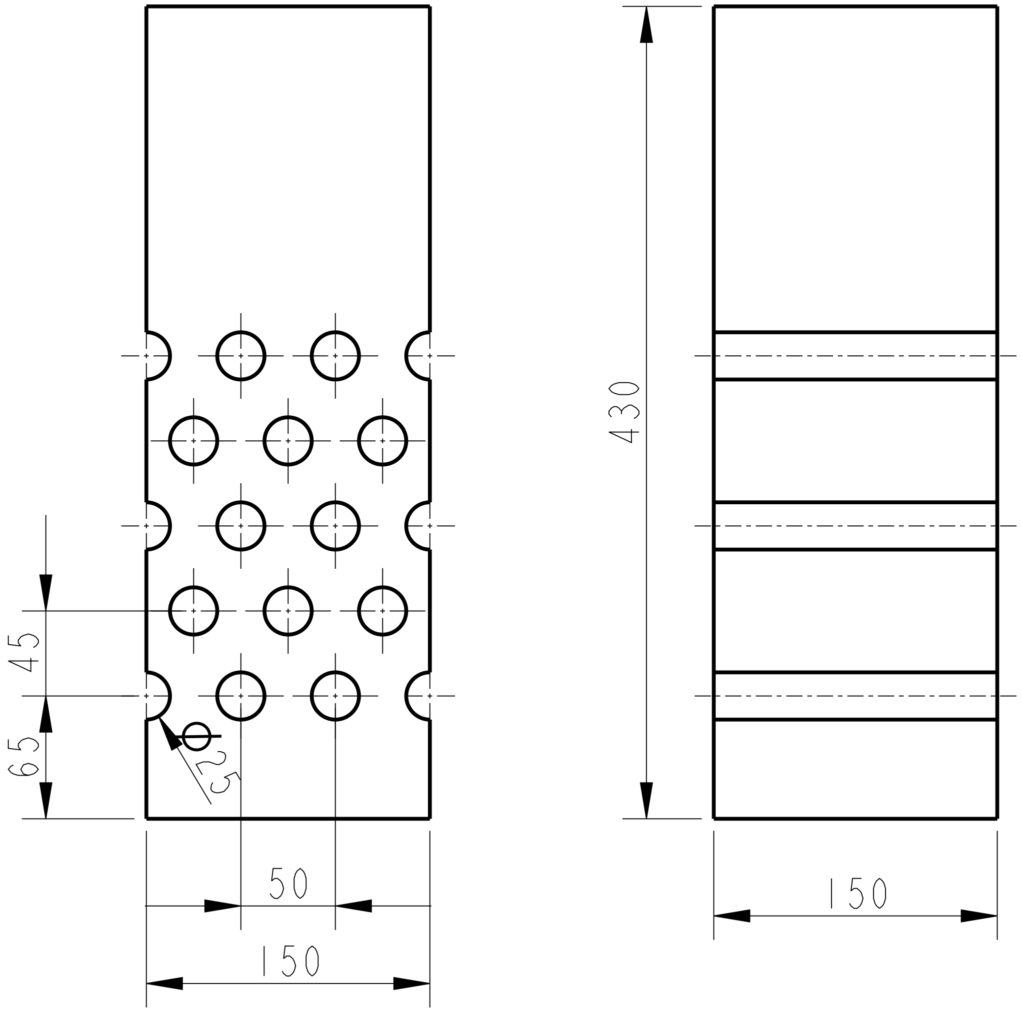

horizontal pitch: 50 mm
vertical pitch: 45 mm
tube: Ø 25 mm

Allgemein toleranz: -	Institut für Energietechnik und Thermodynamik	TU Wien
	Benennung: Geometrie 1b	Name: Noah Ladner
Maßstab: 1 : 4		Studienjahr: 2022
	Zeichnungsnummer: 1	Datum: Apr-15-22

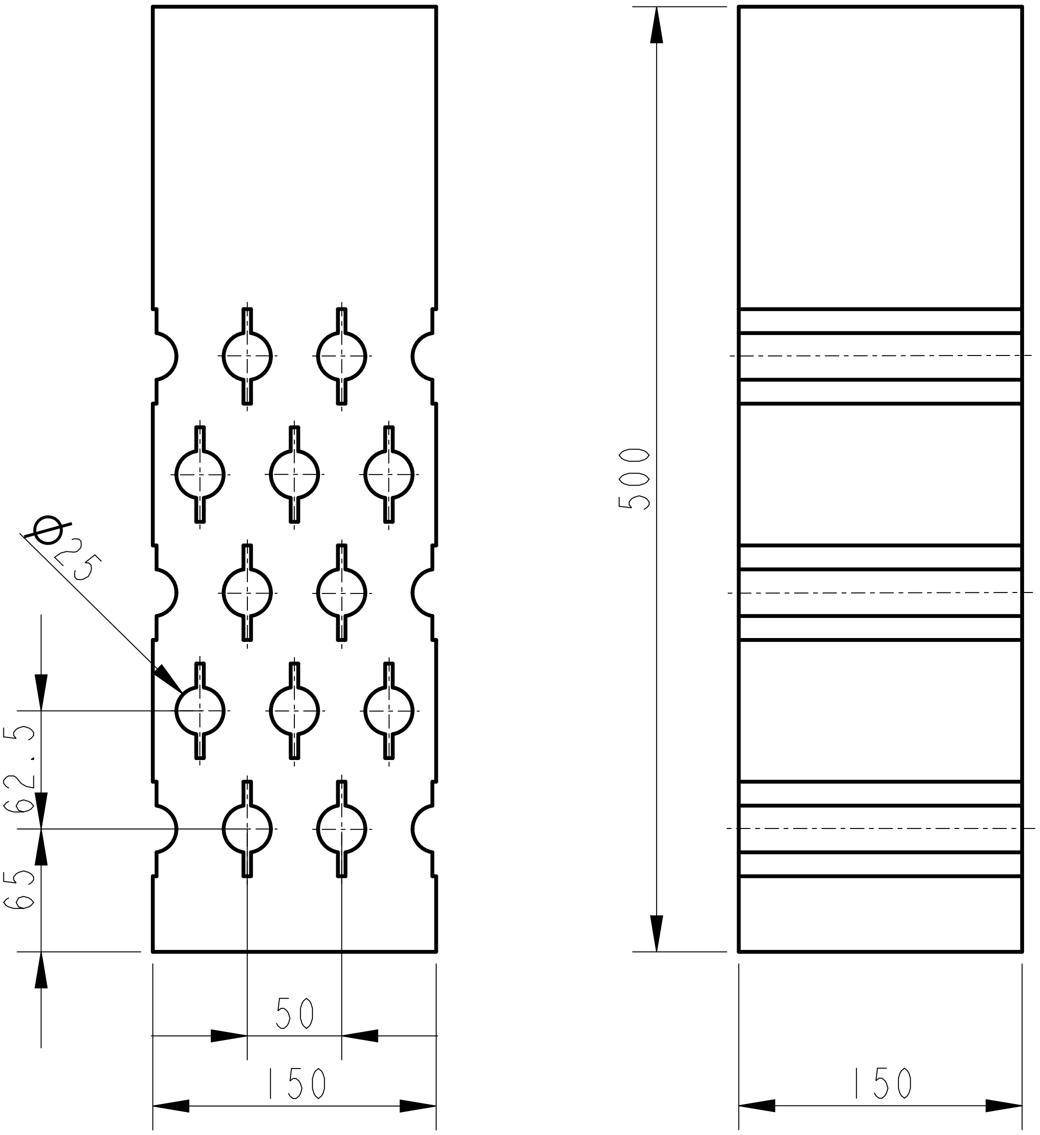

horizontal pitch: 50 mm
vertical pitch: 62.5 mm
tube: Ø25 mm, longitudinal fin h=12.5 mm d=4 mm

Allgemein toleranz: -	Institut für Energietechnik und Thermodynamik	TU Wien
	Benennung: Geometrie 1c	Name: Noah Ladner
Maßstab: 1 : 4		Studienjahr: 2022
	Zeichnungsnummer: 1	Datum: Apr-15-22

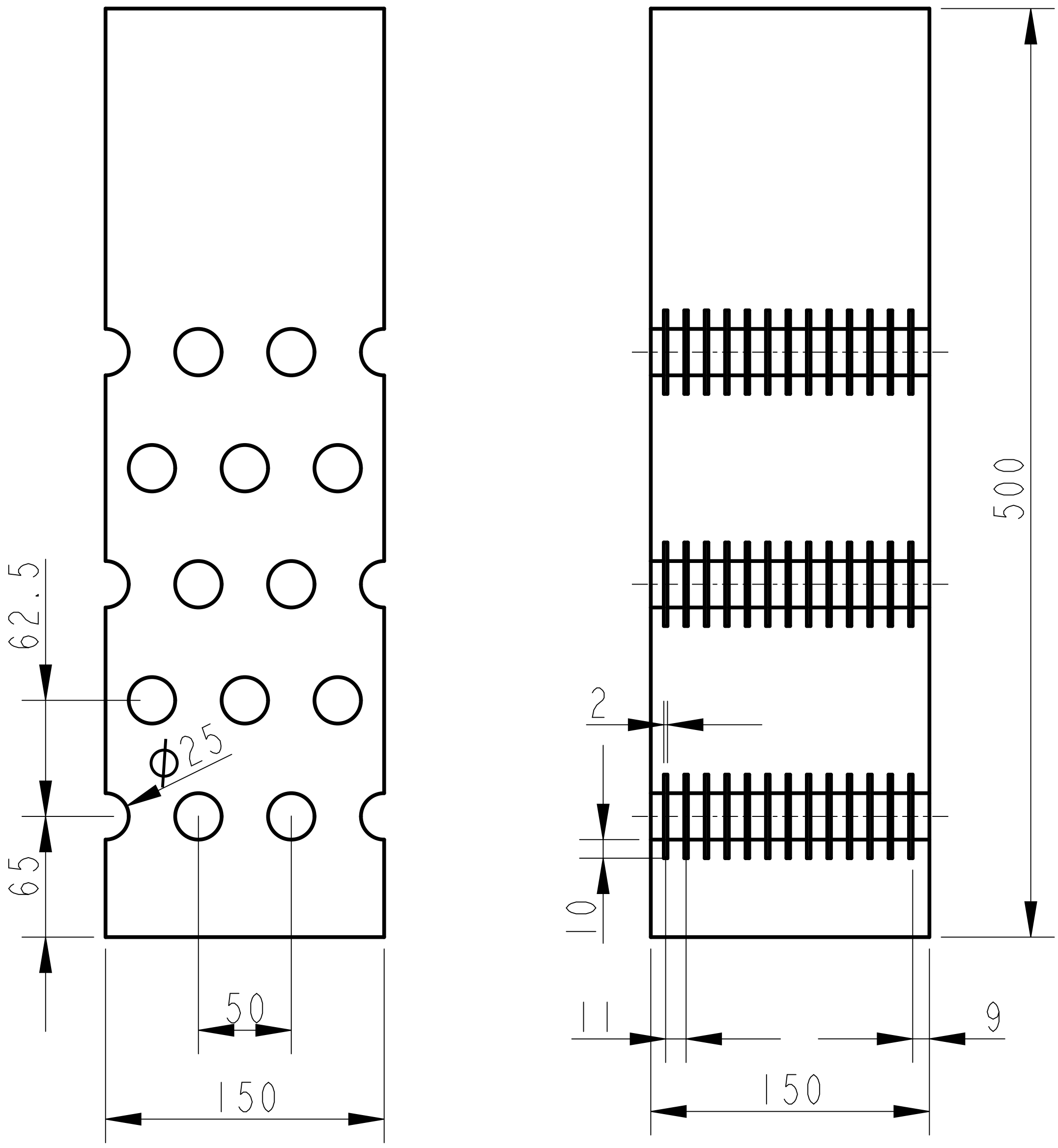

horizontal pitch: 50 mm
vertical pitch: 62.5 mm
tube: Ø25 mm, transversal fins h=10 mm s=2 mm t=11 mm

Allgemein toleranz: –	Institut für Energietchnik und Thermodynamik	TU Wien
	Benennung: Geometrie 1d	Name: Noah Ladner
Maßstab: 1 : 4		Studienjahr: 2022
	Zeichnungsnummer: 1	Datum: Apr-15-22

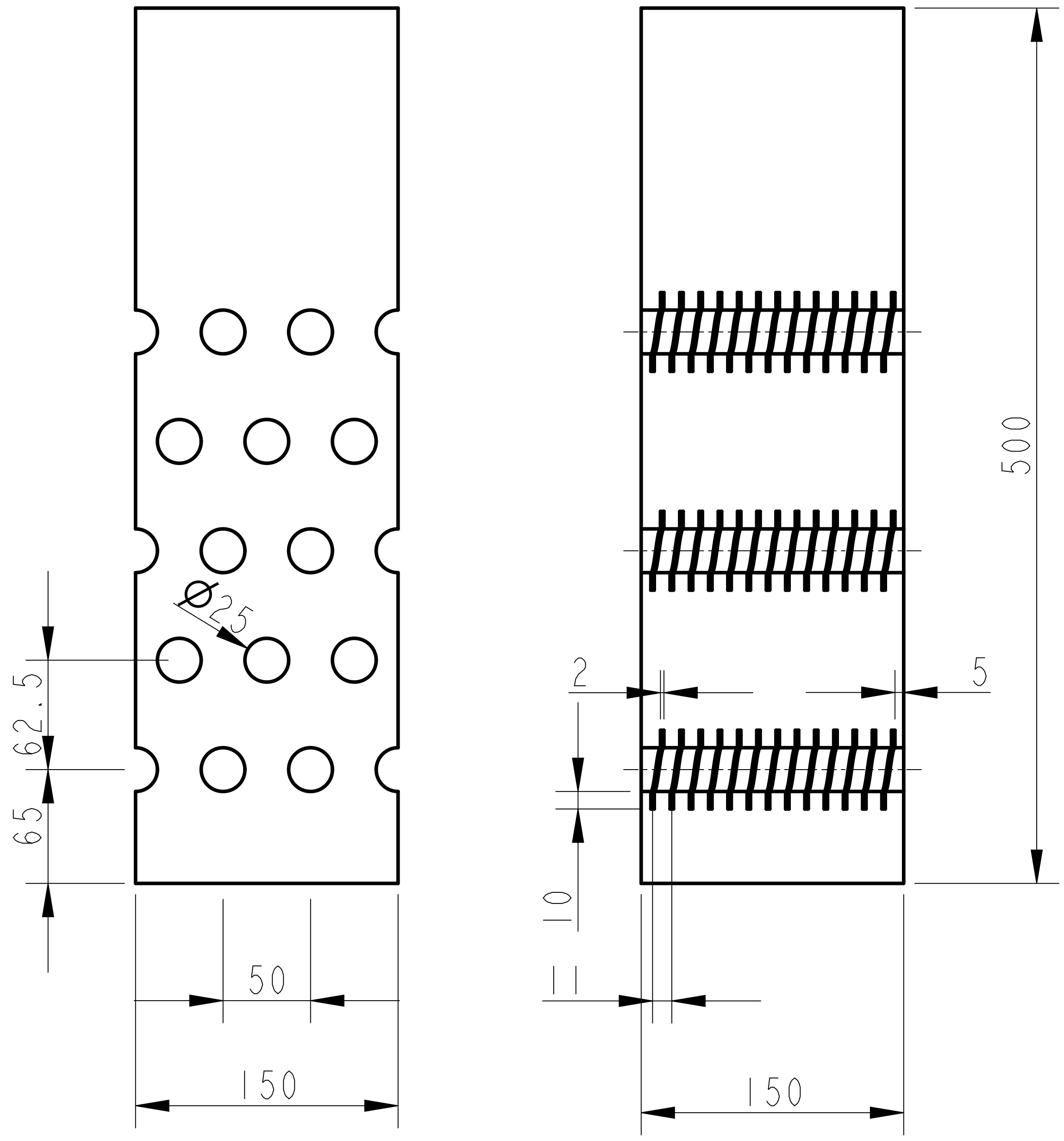

horizontal pitch: 50 mm
vertical pitch: 62.5 mm
tube: Ø25 mm, helical fins h=10 mm s=2 mm p=11 mm

Allgemein toleranz: -	Institut für Energietechnik und Thermodynamik	TU Wien
	Benennung: Geometrie 1e	Name: Noah Ladner
Maßstab: 1 : 4		Studienjahr: 2022
	Zeichnungsnummer: 1	Datum: Apr-16-22

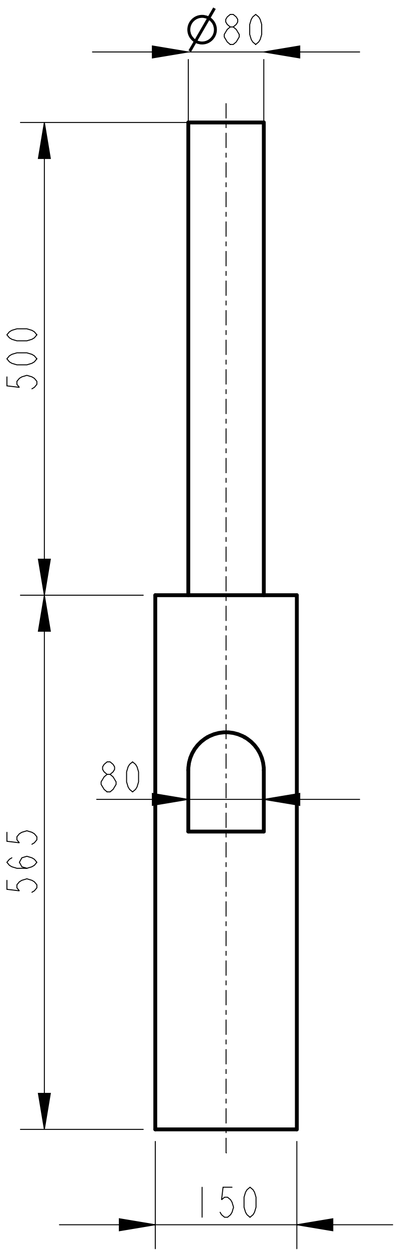

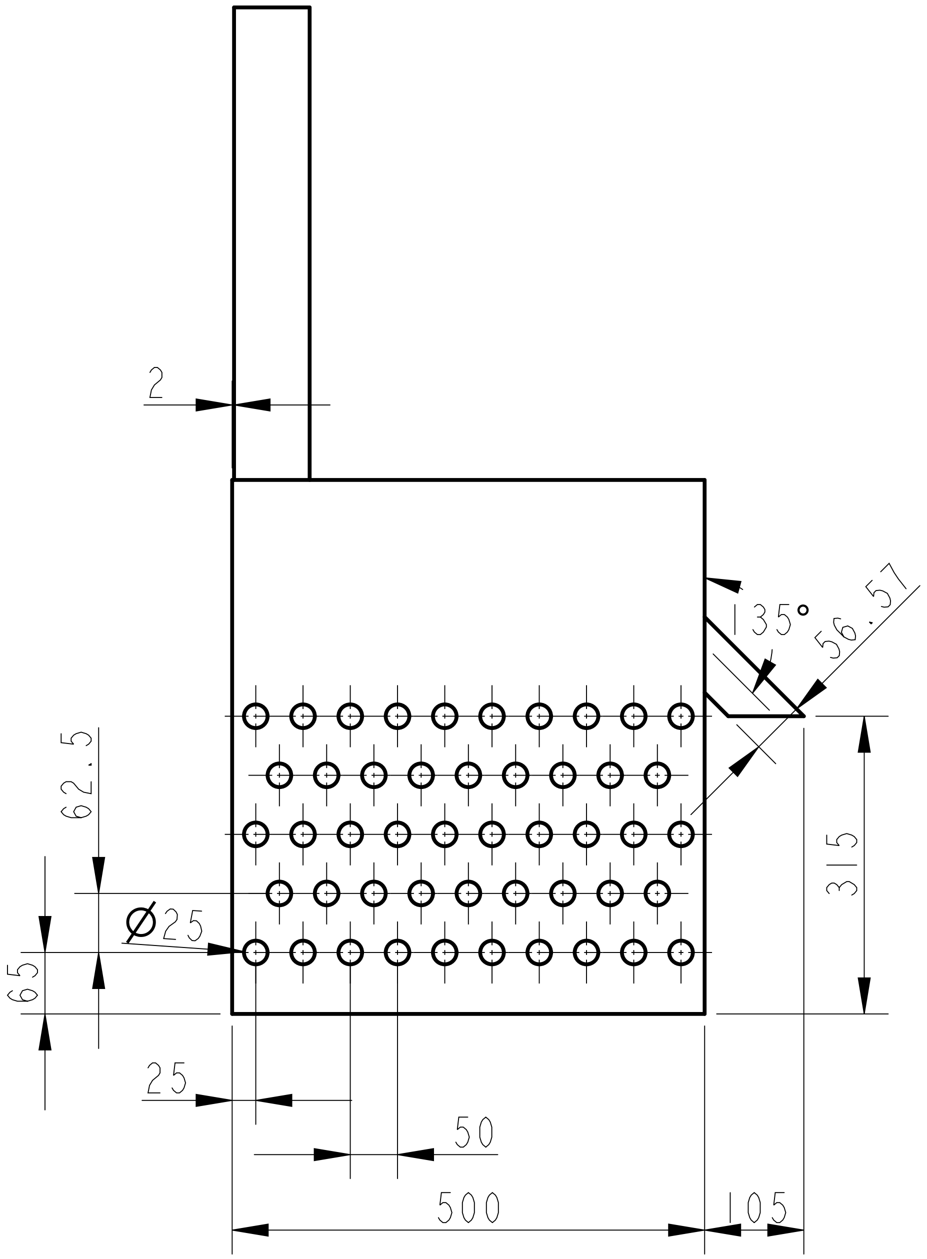

Allgemein toleranz:
-

Institut für Energietechnik und Thermodynamik

TU Wien

Benennung:

Geometrie 2a

Name:
Noah Ladner

Maßstab:

1 : 8

Studienjahr:
2022

Zeichnungsnummer: 1

Datum:
May-03-22

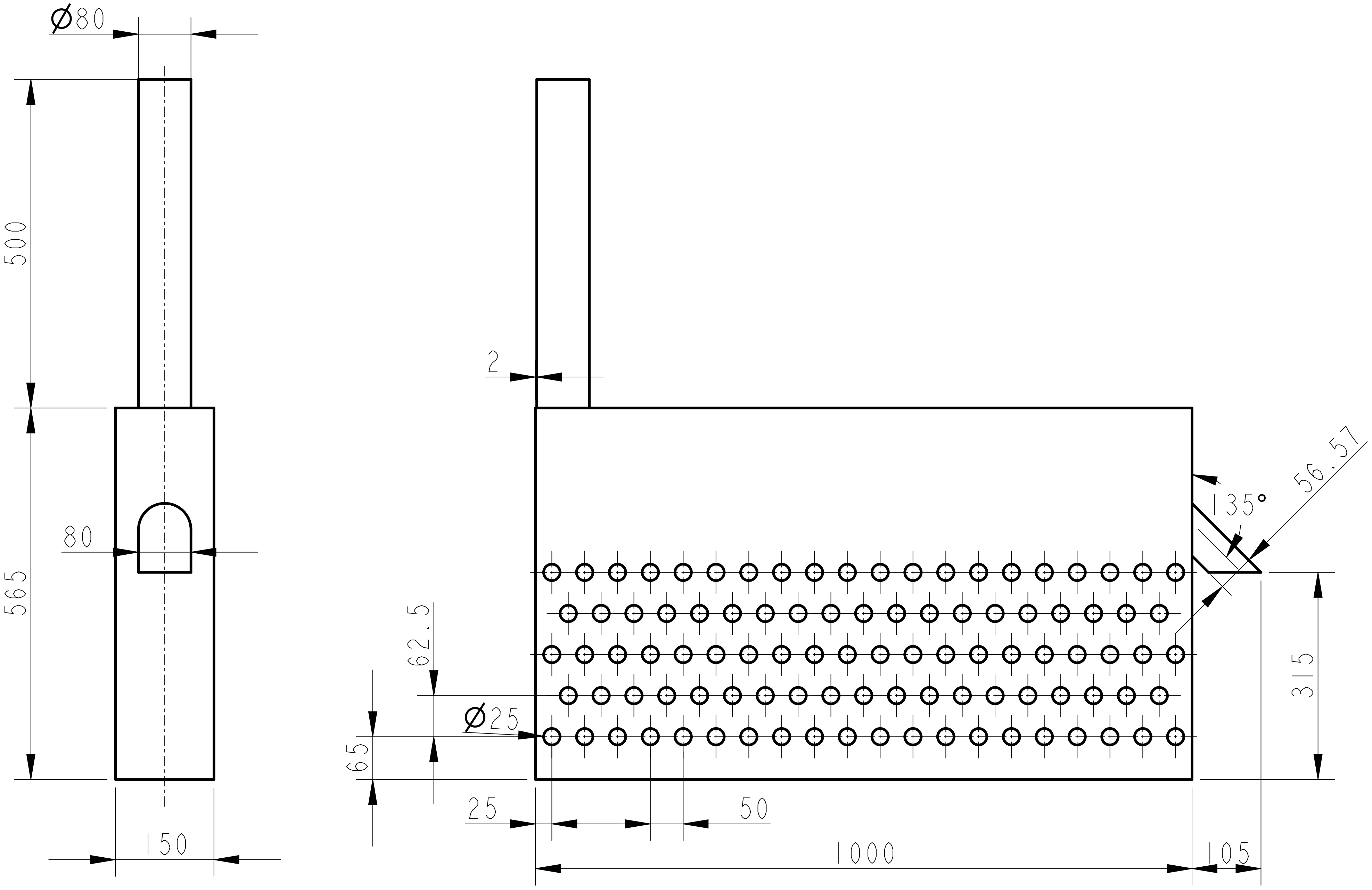

Allgemein toleranz: -	Institut für Energietechnik und Thermodynamik	TU Wien
	Benennung: Geometrie 2b	Name: Noah Ladner
Maßstab: 1 : 8		Studienjahr: 2022
	Zeichnungsnummer: 1	Datum: May-05-22

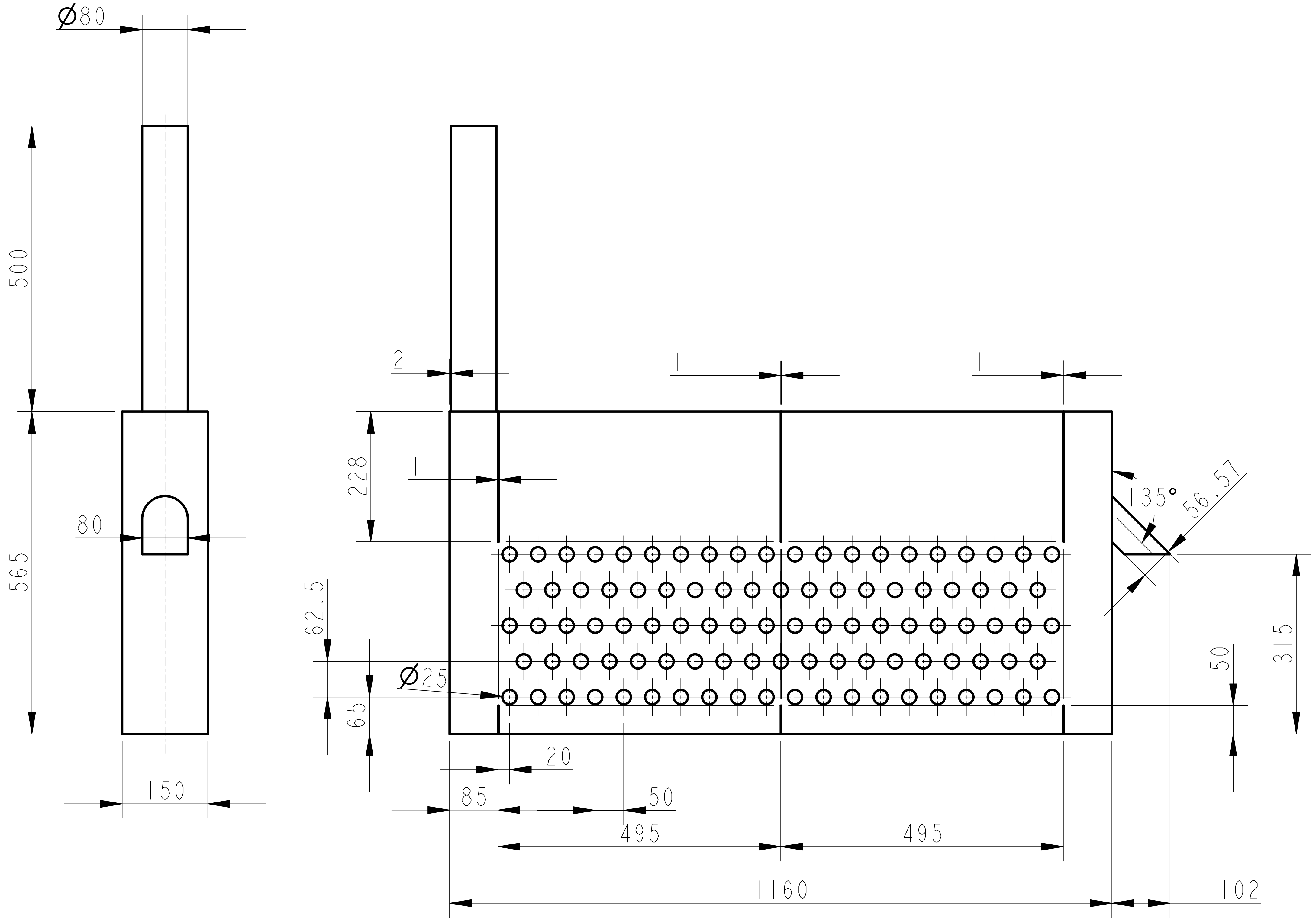

Allgemein toleranz:
-

Institut für Energietechnik und Thermodynamik

TU Wien

Benennung:

Geometrie 3

Name:
Noah Ladner

Maßstab:

1 : 8

Studienjahr:
2022

Zeichnungsnummer: 1

Datum:
May-05-22